Spin and Heat Currents in Magnetic Nanostructures

THÈSE N^{O} 5640 (2013)

PRÉSENTÉE LE 8 FÉVRIER 2013

À LA FACULTÉ DES SCIENCES DE BASE
LABORATOIRE DE PHYSIQUE DES MATÉRIAUX NANOSTRUCTURÉS
PROGRAMME DOCTORAL EN PHYSIQUE

ÉCOLE POLYTECHNIQUE FÉDÉRALE DE LAUSANNE

POUR L'OBTENTION DU GRADE DE DOCTEUR ÈS SCIENCES

PAR

Arndt Christian VON BIEREN

acceptée sur proposition du jury:

Prof. N. Grandjean, président du jury
Prof. J.-Ph. Ansermet, directeur de thèse
Dr U. Ebels, rapporteur
Prof. D. Grundler, rapporteur
Prof. H. Rønnow, rapporteur

ÉCOLE POLYTECHNIQUE
FÉDÉRALE DE LAUSANNE
Suisse
2013

To Julia.

Acknowledgments

I am indebted to many people for their generous support and for making my time as a PhD student – be it in Konstanz or Lausanne – an unforgettable experience. In particular, I would like to express my gratitude to:

. . . **Jean-Philippe Ansermet**, first of all for accepting me as a PhD student in your lab. I am very grateful for your guidance, for providing me with lots of brilliant (and some crazy) ideas, for your indestructible optimism and enthusiasm, and also for giving me the freedom I needed to develop and pursue my own research interests in this last part of my PhD. Thank you for everything!

. . . **Dirk Grundler**, for being an extremely helpful and reliable collaboration partner. Your experience and attention to detail turned our discussions into some of the most efficient and enjoyable ones I have had during my time as a PhD student! Many thanks also for providing me with the samples for my second project, and to **Florian Brandl** for the fabrication.

. . . **Aïcha Hessler-Wyser**, my PhD mentor, for patiently listening to my worries and supporting me with your advice and words of encouragement throughout some of the rougher moments during my PhD. You really made me feel that EPFL's doctoral school is taking care of its PhD students – no matter what. The same applies to **Wolf-Dieter Schneider**, **Susan Killias**, **Thomas Rizzo** and **Jacques Giovanola**. Thank you for your support.

. . . **Mathias Kläui**, for hiring me as a PhD student and giving me the opportunity to move to lovely Lausanne! I would also like to thank **Regina Hoffmann-Vogel** for the collaboration on the nanocontacts project.

. . . **Stephen Krzyk** and **Ajit Patra**, for letting 'Mr. von Bieren' join your team and for teaching me how to tame those nanocontacts! Thanks for all the fun times in the lab and for cheering me up after every single setback. A very special thanks-for-risking-your-life-for-me goes to Ajit for taking care of the HF etching and to both of you for artistic exercises under/in/above the vacuum chamber to fix something . . . ;) It was a pleasure working with you guys!

. . . all my former colleagues at the University of Konstanz: **Jan Heinen, Philipp Möhrke, Gregory Malinowski, Christoforos Moutafis, Jan Rhensius, Jakoba Heidler, Andreas Lörincz, Emil Tafra, Andre Bisig, Lutz Heyne, June Kim-Seo** including the newcomers **Felix Büttner, Christian Dette, Helmut Körner, Mathias Eltschka, Martin Stärk, Philip Wohlhüter and Sebastian Schweitzer** (plus the ones I forgot to mention at this point) for all the good times and their support. Special thanks go to **Greg** and **Andreas** for being the funniest officemates I've had during my PhD, **Jan** for making lots of first-class samples! and **Chris**, the coolest

post-doc ever, for keeping up the good (Greek-y) mood in the lab. Thanks for suggestions on the manuscript **Ciaran Fowley**!

...**Friederike Stuckenbrock**, definitely the coolest secretary ever, for her (administrative *and* moral) support and **Matthias Hagner** for keeping the nanolab up and running.

...**Alina Deac, Andreas Mann, Daniel Rüffer and Antonio Vetrò**, the EPFL-based part of LNSD, first and foremost for sticking together and pulling this through – I think we were a great team! It was really a pleasure and an honor to have you as colleagues and friends. Special thanks go to Andreas for the good teamwork on the TRMOKE setup, to Daniel for sharing his knowledge on electrical measurements and his experience in LabVIEW (and his programs!) with me and to Alina for her scientific (and non-scientific) advice ... and putting up with our German humor ;)

...**Elisa Papa, Francesco Commandè, Pedro Saraiva** (and one more time **Antonio Vetrò**) for being just great colleagues that quickly became friends, and for all your help (and your equipment ;)) for my last project. Also many thanks for all the tips on good Italian food :). I would like to thank **Sylvain Bréchet** for his scientific advice and proofreading my thesis manuscript.

...**Chantal Roulin** and **Florence Grandjean** for welcoming me at EPFL after my relocation from Konstanz to Lausanne, for all the great help with countless things even beyond administration, such as apartment-hunting, translations and teaching me a bit of French every time we spoke! And of course, for their support and trust throughout some of the tougher times ...

...**Stefan Minniberger** and **Alexandre Rydlo**, my first office neighbors and lunchmates at EPFL, for making the transition from Konstanz to Lausanne a lot easier.

...the mechanical engineering / electronics workshop and the IT-service at ICMP for doing an amazing job! Without all those parts, custom electronic devices, advice on measurement setups and really quick support in case of computer/network issues my PhD could have easily taken a year longer. Thank you **Gilles Grandjean, Claude Amendola, Michel Longchamp, Philippe Guex, Olivier Haldimann, Philippe Zürcher, Martial Doy, Primo Locatelli, Claire-Lise Bandelier, José Grandjean, Philippe Cordey and Philippe Cuanillion**.

...lots of other people at ICMP, in particular **Wolfgang Harbich, Harald Brune, Stefano Rusponi** for always being friendly, open and helpful as well as **Alberto Cavallin, Fabian Natterer, Chongqi Yu, Simon Bonanni, Simon Moser, Sergio Vlaic, Fabio Donati, Quentin Dubout and more** for creating such a good atmosphere at the institute (especially on Thursdays at the after-work beer ;))

...**Vladislav Korenivski, Adrian Iovan, Sebastian Andersson and Anders Liljeborg** – my research supervisors and colleagues during my undergraduate studies at KTH Stockholm. The experimental techniques and the way of working in the lab/cleanroom that I have learned in your lab have been invaluable for every project I have worked on during my PhD!

Zum Schluss möchte ich den wichtigsten Personen in meinen Leben danken:

. . . **meiner Familie – Mama, Papa und Carsten** – für eure bedingungslose Unterstüzung und euren Rückhalt über all die Jahre, eure Liebe und eure Geduld. Jetzt bin ich endlich mit dem Studium fertig! ;) Danke auch an **Uta, Harald und Christiane** für eure Unterstützung!

. . . **Julia** – ich will gar nicht erst versuchen in Worte zu fassen wie groß dein Anteil an dieser Arbeit ist und wie dankbar ich dir dafür bin... Du hättest wirklich einen zweiten Doktortitel verdient! :) ♡

Lausanne, 18 December 2012 A. v. B.

Abstract

It was the purpose of this thesis to contribute to a better understanding of magnetoresistance phenomena as well as thermoelectric and spin caloritronic effects in magnetic micro and nanostructures. This work is divided into two parts: (I) Magnetoresistance phenomena in tailored magnetic nanocontacts, and (II) Thermoelectric effects and ferromagnetic resonance in laser-heated microstructures.

First, we investigate magnetoresistance (MR) effects in stable and clean Permalloy ($Ni_{80}Fe_{20}$, Py) nanocontacts of variable cross-section, ranging from the diffusive to the ballistic conduction regime. We fabricate nanocontacts by combination of ultra-high vacuum deposition and *in-situ* electromigration in a tailored ring geometry that allows us to precisely control the positioning of a magnetic domain wall. In the diffusive regime up to a resistance of $R \approx 540\,\Omega$, we observe three different resistance levels, corresponding to distinct domain wall positions. The evolution of these levels as a function of contact size can be reproduced by geometry-dependent simulations of the anisotropic MR (AMR) based on micromagnetic and current distribution simulations. This confirms that the bulk AMR dominates the MR signal in the diffusive regime and excludes a significant intrinsic domain wall MR. At higher contact resistances the situation changes drastically and we detect large domain wall induced MR effects by measuring the resistance values of the nanocontact with and without a domain wall at zero applied field. In the ballistic transport regime, the MR ratio reaches up to 50% and exhibits a previously unobserved sign change. Our results can be reproduced by recent atomistic calculations of the DW-induced MR for different configurations of the nanocontact, highlighting the importance of the contact's detailed atomic arrangement.

Second, we address the issue of spurious thermoelectric phenomena that can occur in the transverse spin Seebeck effect geometry. We employ scanning focused laser heating to generate temperature gradients on a µm-scale and we characterize the laser-induced thermovoltages in microscopic crossed Au / Py wires on MgO and GaAs substrates. Supported by numerical simulations of the laser-induced temperature distribution and spatially resolved as well as time-resolved electrical measurements, we unambiguously identify and separate two major contributions: (i) the Seebeck effect due to local heating of the Au/Py thermocouples and (ii) the anomalous Nernst effect (ANE) in Py due to the large out-of-plane temperature gradient generated at the position of the laser spot. Furthermore, we demonstrate thermoelectrical magnetic imaging based on spatially resolved ANE measurements and resolve the micromagnetic behavior of a Py wire on the µm-scale. We observe the formation and pinning of magnetic domains during magnetization reversal and detect the impact of laser heating on the reversal process. Finally, we search for evidence for the existence of a thermally induced bulk spin current in thin Py films. For this purpose, we combine the generation of very large heat gradients with the local excitation and detection of ferromagnetic resonance (FMR). Our analysis shows that the observed laser-induced changes of the FMR lineshape can be entirely attributed to the temperature-dependence of the saturation magnetization.

Keywords: magnetoresistance, nanocontact, domain wall, electromigration, laser heating, thermoelectric voltage, magnetic imaging, spin caloritronics, ferromagnetic resonance.

Zusammenfassung

Ziel dieser Dissertation ist das bessere Verständnis von Magnetwiderstandseffekten sowie thermoelektrischen und spin-kalorischen Effekten in magnetischen Mikro- und Nanostrukturen. Die folgende Arbeit gliedert sich in zwei Teile: (I) Magnetwiderstandseffekte in ringförmigen magnetischen Nanokontakten, (II) thermoelektrische Effekte und ferromagnetische Resonanz in lasergeheizten Mikrostrukturen.

Im ersten Abschnitt untersuchen wir Magnetwiderstandseffekte in stabilen, verunreinigungsfreien Permalloy ($Ni_{80}Fe_{20}$, Py) Nanokontakten variabler Größe im diffusiven und ballistischen Transportregime. Die Herstellung erfolgt durch Aufdampfen im Vakuum sowie anschließende Elektromigration. Dabei ermöglicht uns eine spezielle halbringförmige Geometrie der Kontakte, magnetische Domänenwände (DW) präzise zu positionieren. Im diffusiven Bereich bis $R \approx 540\,\Omega$ beobachten wir drei verschiedene Widerstandsniveaus und ordnen diese unterschiedlichen DW-Positionen zu. Geometrieabhängige Berechnungen des anisotropen Magnetwiderstandes (AMR) auf Basis von stromdichte- und mikromagnetischen Simulationen zeigen große Übereinstimmung mit der beobachteten Entwicklung dieser Niveaus als Funktion des Kontaktwiderstandes. Daraus schließen wir, dass in diesem Widerstandsbereich der AMR den dominierende Beitrag zum Magnetwiderstand liefert und intrinsische Widerstandsbeiträge der DW vernachlässigt werden können. Bei höheren Widerstanden, insbesondere im ballistischen Regime, beobachten wir bis zu 50 % DW-induzierten Magnetwiderstand und einen bisher unbekannten Vorzeichenwechsel. Dieses Verhalten lässt sich auf Grundlage von kürzlich vorgestellten atomistischen Berechnungen des Magnetwiderstandes für verschiedene atomare Konfigurationen des Kontaktes verstehen, was die Bedeutung der genauen atomaren Anordnung für Größe und Vorzeichen des Effektes unterstreicht.

Der zweite Abschnitt befasst sich mit thermoelektrischen Effekten, die in Messungen des (transversen) spin Seebeck Effektes als Artefakte auftreten können. Dazu erzeugen wir µm-genau positionierte Temperaturgradienten mittels fokussiertem Laserheizen und bestimmen die in mikroskopischen, gekreuzten Au/Py-Drähten auftretendenden laserinduzierten Thermospannungen. Durch numerische Simulationen des erzeugten Temperaturprofils sowie räumlich als auch zeitlich aufgelöste elektrische Messungen lassen sich zwei dominierende Effekte eindeutig identifizieren: (i) Der Seebeck Effekt durch Erwärmung von Au/Py-Thermoelementen sowie (ii) der anomale Nernst Effekt (ANE) in Py durch lokale Temperaturgradienten innerhalb des Laserspots. Desweiteren demonstrieren wir die thermoelektrische Abbildung der Magnetisierung mithilfe örtlich aufgelöster Messungen des ANE. Darauf aufbauend bilden wir die Ummagnetisierung eines Py-Drahtes ab und analysieren die Entstehung und Verankerung von DW sowie den Einfluss des Laserheizens auf den Umkehrprozess. In einem zweiten Abschnitt untersuchen wir lokal erwärmte Py Dünnschichten hinsichtlich der Existenz thermisch generierter Spinströme. Zu diesem Zweck kombinieren wir lokales Laserheizen mit lokaler Anregung und Detektion von ferromagnetischer Resonanz (FMR). Wie unsere Analyse zeigt, kann die Änderung der FMR im Temperaturgradient vollständig auf die Temperaturabhängkeit der Sättigungsmagnetisierung zurückgeführt werden.

Stichwörter: Magnetwiderstand, Nanokontakt, Domänenwand, Elektromigration, Laserheizen, Thermospannung, Spin Kaloritronik, Ferromagnetische Resonanz.

Résumé

Ce travail de thèse est dédié à l'étude et à la compréhension des phénomènes de magnétorésistance ainsi que des effets thermoélectriques et de spin caloritronique dans des microstructures et nanostructures magnétiques. Il s'articule autour de deux parties : (I) étude de l'effet de la magnétorésistance des nanocontacts magnétiques de tailles différentes et, (II) l'étude des phénomènes thermoélectriques et des courants de spin générés par un courant de chaleur.
Premièrement, nous avons étudié l'effet de la magnétorésistance (MR) dans des nanocontacts à base de Permalloy ($Ni_{80}Fe_{20}$, Py) de différentes tailles. Cette approche nous permet d'étudier la MR sur une gamme de conductivité électrique allant du régime diffusif au régime balistique. La fabrication de ces nanocontacts a été faite de la façon suivante : déposition de la couche mince dans un vide poussé suivi d'une électromigration in-situ de la nanostructure à géométrie circulaire. L'utilisation de cette géométrie circulaire permet de contrôler la position de la paroi de domaine magnétique. En régime diffusif, trois paliers distincts de résistance ont été observés et correspondent à une certaine position de la paroi de domaine. De plus, nous observons une dépendance de ces paliers de résistance en fonction de la taille du nanocontact. La compréhension de l'évolution de la résistance en fonction de la taille des nanocontacts a été réalisée théoriquement en utilisant deux approches : micro-magnétisme et distribution de courant. Ces approches ont permis de démontrer que la magnétorésistance anisotropique (AMR) est la contribution dominante dans le signal de MR observé, excluant par la même l'effet intrinsèque d'une paroi de domaine dans ce régime. Toutefois, pour des résistances de contact plus élevées, la situation change drastiquement. En effet, nous observons une large paroi de domaine induisant un effet sur la MR. Dans le régime de transport balistique, la variation de la MR est de 50% et montre une inversion de signe. L'utilisation d'une approche atomistique et la prise en compte de différents arrangements atomiste au niveau des contacts ont permis d'expliquer les résultats obtenus dans ce régime. L'importance de l'arrangement des atomes au niveau des contacts a été démontrée.
Deuxièmement, nous abordons la question des phénomènes thermoélectriques parasites qui peuvent se produire en mesurant l'effet spin Seebeck transverse. Dans ce but, nous avons utilisé un laser focalisé à balayage pour générer un gradient de température à une échelle micrométrique afin de mesurer la différence de potentiels électrique sur des microfilaments d'or/permalloy (Au/Py) déposés sur des substrats de MgO et GaAs. L'utilisation de simulateur numérique pour déterminer la distribution de températures sur ces microstructures et les mesures électriques en temps résolu, nous ont permis d'identifier clairement deux contributions majeurs : (i) L'effet Seebeck dû au chauffage local lié au thermocouple Au/Py et (ii) l'effet Nernst anormal (ANE) dans le permalloy dû au large gradient de température hors plan. En outre, l'imagerie magnétique thermoélectrique nous a permis d'étudier le comportement micromagnétique du microfilament de Py. Finalement, nous avons cherché à démontrer l'existence d'un courant de spin généré par un courant de chaleur dans des couches minces de Py. Pour ce faire, nous avons combiné la production d'un large gradient de température avec l'excitation locale et la détection par résonance ferromagnétique (FMR). Notre analyse montre une modification des pics de résonance sous un fort gradient de température et ceci a été attribué à une dépendance en température de l'aimantation à saturation.

Mots-clés : magnétorésistance, paroi de domaine, électromigration, chauffage laser, thermoélectricité, imagerie magnétique, spin caloritronique, résonance ferromagnétique.

List of publications

Project-related publications

I. A. K. Patra, A. von Bieren, S. Krzyk, J. Rhensius, L. J. Heyderman, R. Hoffmann, and M. Kläui. *Magnetoresistance measurement of tailored Permalloy nanocontacts*.
Physical Review B 82,134447 (2010).

Author contribution: Sample fabrication, performed most of the measurements and part of the simulations, took part in preparing the manuscript.

II. A. von Bieren, A. K. Patra, S. Krzyk, J. Rhensius, L. J. Heyderman, R. Hoffmann-Vogel, and M. Kläui. *Domain-wall induced large magnetoresistance effects at zero applied field in ballistic nanocontacts*.
Physical Review Letters 110, 067203 (2013).

Author contribution: Conceived fabrication process and prepared samples, performed measurements and data analysis, wrote the manuscript.

III. A. von Bieren, F. Brandl, D. Grundler, J.-Ph. Ansermet. *Space- and time-resolved Seebeck and Nernst voltages in laser-heated permalloy/gold microstructures*.
Applied Physics Letters 102, 052408 (2013).

Author contribution: Developed experiment, performed measurements and data analysis, wrote the manuscript.

Minor contributions

I. D. Ilgaz, J. Nievendick, L. Heyne, D. Backes, J. Rhensius, T. A. Moore, M. Á. Niño, A. Locatelli, T. O. Menteş, A. v. Schmidsfeld, A. v. Bieren, S. Krzyk, L. J. Heyderman, and M. Kläui. *Domain-Wall depinning assisted by pure spin currents*.
Physical Review Letters 105, 076601 (2010).

II. A. Bisig, J. Rhensius, M. Kammerer, M. Curcic, H. Stoll, G. Schütz, B. van Waeyenberge, K. Wei Chou, T. Tyliszczak, L. J. Heyderman, S. Krzyk, A. von Bieren and M. Kläui. *Direct imaging of current induced magnetic vortex gyration in an asymmetric potential well*.
Applied Physics Letters 96, 152506 (2010).

Contents

List of Figures

List of Abbreviations

AMF	Atomic Force Microscopy
AMR	Anisotropic Magnetoresistance
ANE	Anomalous Nernst Effect
BMR	Ballistic Magnetoresistance
DW	Domain Wall
DWMR	Domain Wall Magnetoresistance
EDFMR	Electrically Detected Ferromagnetic Resonance
EM	Electromigration
FEM	Finite Element Method
FM	Ferromagnet / Ferromagnetic
FMR	Ferromagnetic Resonance
FIB	Focussed Ion Beam
FWHM	Full Width at Half Maximum
GMR	Giant Magnetoresistance
HF	Hydroflouric Acid
(I)SHE	(Inverse) Spin-Hall Effect
MR	Magnetoresistance
MTJ	Magnetic Tunnel Junction
MW	Microwave
NM	Normal Metal
Py	Permalloy ($Ni_{80}Fe_{20}$)
RF	Radio Frequency
RIE	Reactive Ion Etching
SE	Seebeck Effect
SEM	Scanning Electron Microscope
SPV	Surface Photo Voltage
SSE	Spin Seebeck Effect
STT	Spin Transfer Torque
TC	Thermocouple
TMR	Tunneling Magnetoresistance
TTL	Transistor-Transistor Logic
UHV	Ultra High Vacuum
YIG	Yttrium Iron Garnet

Introduction

The miniaturization of integrated circuits (ICs) and the rise of semiconductor technology has not only revolutionized our economies, but also the way we live and communicate. Huge efforts are made to sustain the remarkable growth in IC performance attained during the past decades (described by *Moore's law*). However, the pace of miniaturization is expected to start slowing down soon as transistors and memory elements approach ultimate limits in terms of size, stability and power dissipation.

Traditional electronic devices are based on manipulating electron charges. The field of *Spintronics* – spin-based electronics – opens up new approaches to tackling these miniaturization issues and adding new functionality by exploiting the electron's intrinsic angular momentum (or *spin*) in addition to its charge [1, 2]. For instance, extremely thin magnetic wires, so-called magnetic nanocontacts (see Part I), might one day be employed as memory elements [3], enabling ultra-high storage densities close to the ultimate atomic limit. Novel spin-dependent thermoelectric effects (see Part II) could help 'recycling' waste heat to reduce power consumption [4]. Additionally, such effects contribute to our understanding of pure spin currents, potentially enabling a dissipation-free alternative to charge-based electronics [5].

Research in the area of spintronics has developed at a remarkable pace during the last 20 to 30 years. In particular the discovery of giant magnetoresistance (GMR) in 1988 and its subsequent commercialization in magnetic hard disk drives by IBM [6] less than a decade later was a breakthrough for the field and led to a surge in activities. The Nobel Prize in Physics in 2007, awarded for the discovery of GMR [7, 8], highlights this milestone. However, despite the field's maturity in terms of a few technological applications, many aspects of spin-dependent electron transport are still not fully understood and new effects continue to emerge [9].

Of particular interest are phenomena that lead to a change of the electrical resistance of a conductor in response to a changing local magnetization or external magnetic field. With the emergence of thin-film deposition techniques, the giant magnetoresistance (GMR) effect was discovered and tunneling magnetoresistance (TMR [10]) could be investigated systematically. In both cases, the resistance depends on the mutual orientation of two closely spaced ferromagnetic thin films. Modern nanofabrication tools open the possibility to study such effects in fully customized geometries. This allows us to directly investigate the effect of inhomogeneous magnetization structures [11], such as domain walls, on the MR. In fact, experimental evidence

suggests that a domain wall, if small enough, can have an intrinsic contribution to the MR, the so-called domain wall magnetoresistance (DWMR) [12]. Theoretical models attribute the effect to modulated spin-dependent scattering probabilities within the wall [13]. However, the precise origin of the various observations made in different materials and geometries is still subject to discussion [14]. In particular, the nature of DWMR in (technologically most relevant) soft magnetic materials, such as Permalloy (Py ≡ $Ni_{80}Fe_{20}$), is unclear as the effect is hard to distinguish from the anisotropic magnetoresistance (AMR) in most geometries.

When the size of a conductor approaches critical length scales (spin diffusion length & electron mean free path), the properties of electron transport change drastically [15]. Nanocontacts offer the possibility to study such length scales. Especially in the ballistic conduction regime, where electrons are presumed to travel scatter-free, novel MR phenomena have been observed [14]. Depending on the experimental details, these effects are called ballistic magnetoresistance (BMR), enhanced/atomic AMR or DWMR [16]. However, reliable MR measurements on nanocontacts entail particular requirements in terms of stability, cleanliness and control of the magnetization. A major challenge is the identification of and discrimination between the various MR effects. Unambiguous and artifact-free measurements of any of the considered effects are therefore hard to accomplish. Clear-cut experimental demonstrations are rare and often contradict previous results [16]. Hence, in Part I of this thesis we aim at providing more reliable MR measurements of such nanocontacts (see below).

The same way domain walls can influence the electron transport (MR effects), reciprocally, spin-polarized currents can be used to manipulate magnetic configurations [17]. The corresponding mechanism, the spin transfer torque (STT), is well-understood [18] and plays an essential role in various applications, such as magnetoresistive random access memory (MRAM). A key issue of devices based on this effect (and of microelectronics in general) is that charge currents entail heating, which is a growing obstacle as device dimensions continue to shrink. Therefore, alternative approaches that avoid the generation of heat are urgently needed. One of them is based on pure diffusive spin currents, as those currents do not convey a net charge current, but only involve a transport of spin angular momentum.

It was shown experimentally how pure spin currents can be generated, controlled and employed in nanodevices [19]. When generating spin currents using spin-polarized charge currents, the required current density is usually unfavorably large. To avoid this problem, more efficient ways to generate spin currents are being explored. An interesting approach is based on the recently found spin Seebeck effect (SSE) [20], referring to the generation of a spin current induced by a constant orthogonal temperature gradient in a ferromagnetic material. Apart from the intriguing perspective of using this effect in spin current based devices and heat machines, the effect is also challenging from a fundamental physics point of view as its precise origin and its phenomenology in various magnetic structures are still not fully understood [4]. Part II of this thesis aims at enhancing our understanding of different spurious thermoelectric effects in SSE measurements and probing for the presence of thermally induced spin currents in thin ferromagnetic films (see below).

This thesis

The following thesis is presented in two independent parts which were conducted at separate times. Part I is based on a one-year project on magnetoresistance in magnetic nanocontacts at the University of Konstanz under Prof. Matthias Kläui. After relocating to EPFL in June 2010 and the departure of Prof. Kläui in June 2011, the planned topic of time-resolved MOKE measurements (not part of this thesis) was abandoned and I continued under the guidance of Prof. Jean-Phillipe Ansermet. The work presented in Part II was conducted in his group and in close collaboration with Prof. Dirk Grundler (Technical University of Munich).

Part I: Investigation of MR properties of ferromagnetic nanocontacts

The main objectives of this project are the identification, discrimination and analysis of the various MR effects at play in ferromagnetic nanocontacts in the diffusive and ballistic conduction regime. Of particular interest are the anisotropic MR (AMR) and the domain wall MR (DWMR) as they are often hard to distinguish. Many previous studies have suffered from various drawbacks preventing a distinct analysis, such as artifacts due to magnetostriction, high impurity concentrations as well as a lack of precise control of the magnetization structure. The approach developed in this thesis aims at eliminating most of these issues by employing specially tailored sample designs based on a half-ring structure and performing fabrication and measurements in a UHV environment. This allows us to study MR effects in exceptionally stable and clean contacts of variable size, ranging from the diffusive to the ballistic regime.

Part II: Thermoelectric effects and ferromagnetic resonance in laser-heated structures

It has been shown recently that many SSE experiments are prone to artifacts due to spurious temperature gradients, in particular in the transverse geometry where the generation of a pure in-plane temperature gradient is essential. Using focused laser-induced heating, we aim at improving the understanding of possible thermoelectric artifacts in this configuration. For this purpose we characterize the temperature gradients and the resulting thermovoltages in microscopic crossed Au / Py wires. By combining spatially resolved and time-resolved thermoelectric measurements with numerical simulations of the temperature distribution, we are able to separate and unambiguously identify two distinct contributions to the generated signal. Additionally, we demonstrate thermoelectrical magnetic imaging of Py wires using spatially resolved measurements of the anomalous Nernst effect and study the formation and pinning of magnetic domains during magnetization reversal. Furthermore, to date very few experimental studies have confirmed the existence of the SSE itself. Hence, further characterization of the effect using a new approach would be highly desirable. In this prospect, we develop a novel measurement technique based on laser-induced heating and ferromagnetic resonance (FMR). We employ the technique to assess the presence of thermally generated spin currents in thin Py layers.

Part I

Magnetoresistance phenomena in tailored magnetic nanocontacts

1 Theoretical and experimental background

Part I of this thesis deals with the evolution of magnetoresistance (MR) effects in magnetic nanocontacts in both the diffusive and the ballistic conduction regime. This initial chapter provides a brief introduction to the most relevant concepts, theoretical models and previously published studies. Chapter 2 addresses the experimental techniques employed, i.e. fabrication methods and measurement schemes. Part I is concluded by the presentation and discussion of the measurement results in Chapter 3 and a summary with concluding remarks in Chapter 4.

1.1 Spin-dependent transport

Ferromagnetism & Spin polarization

In ferromagnetic transition metals (Iron (Fe), Nickel (Ni) and Cobalt (Co)), ferromagnetism and hence the spin polarization of the electron system arises from the balance between two effects. The exchange interaction tends to align the spins in the partially occupied 3d-orbitals [21], giving rise to a nonzero magnetic moment of the atom. The energy gain of this alignment is due to the Pauli exclusion principle. It maximizes the distance between electrons of the same spin and thus lowers the energy associated with their Coulomb repulsion. However, this is only true for isolated atoms. In solids the hybridization between atomic orbitals and the formation of electronic bands can inhibit the occurrence of a net magnetic moment. Aligning the spins in the 3d band requires occupying states with higher kinetic energy compared to a balanced band with $N^{\uparrow} = N^{\downarrow}$. A net magnetic moment (i.e. a spin-imbalance) only occurs if the cost of the redistribution of electrons is counterbalanced by a sufficient gain in exchange energy. This is the so-called Stoner criterion, which predicts the occurrence of band ferromagnetism in Fe, Ni and Co. In these materials the majority spin sub-band $d^{\uparrow}$ is shifted to lower energies with respect to the minority band $d^{\downarrow}$, leading to $N^{\uparrow} \neq N^{\downarrow}$ and hence a finite magnetization in equilibrium.

As a result of this exchange splitting, the density of states (DOS) at the Fermi level $D_{\mathrm{F}}^{\uparrow,\downarrow}$ becomes different for the two electron sub-bands. This yields different conductivities for majority and

minority electrons (here denoted by ↑ and ↓, respectively), given by

$$\sigma^{\uparrow,\downarrow} = 1/\rho^{\uparrow,\downarrow} = e^2 \tau^{\uparrow,\downarrow} D_F^{\uparrow,\downarrow} / m^\star \,, \tag{1.1}$$

where $\tau^{\uparrow,\downarrow}$ is the spin-dependent relaxation time, e the electron charge and $m^\star$ the effective electron mass. If spin-flip scattering is weak, the conduction in a ferromagnet can therefore be described by a resistor model with two parallel channels with different resistivities. This is the two-channel model developed by Mott [22], according to which the total resistivity is given by

$$\rho = \frac{\rho^\uparrow \rho^\downarrow}{\rho^\uparrow + \rho^\downarrow} \,. \tag{1.2}$$

The current in a ferromagnetic metal is mainly carried by the s-electrons as they exhibit a much lower mass $m^\star$ than d-electrons. However, spin-conserving s-to-d transitions are the main source of scattering for s-electrons and determine $\tau^{\uparrow,\downarrow}$ in Equation (1.1). Hence, a high (low) DOS in the d sub-band (i.e. a large (small) number of available states to scatter to) will give rise to a high (low) resistivity of the corresponding spin channel.

A corresponding transport spin polarization can be defined as

$$P_j \equiv \frac{j^\uparrow - j^\downarrow}{j^\uparrow + j^\downarrow} = \frac{\sigma^\uparrow - \sigma^\downarrow}{\sigma^\uparrow + \sigma^\downarrow} \tag{1.3}$$

where $j^{\uparrow,\downarrow}$ is the bulk current density in the respective spin channel. This is generally not the same as the spin polarization of the d-band DOS, $P = \left(D_F^\uparrow - D_F^\downarrow\right) \Big/ \left(D_F^\uparrow + D_F^\downarrow\right)$, as most of the current is not carried by the d-electrons. Measuring the spin polarization is a challenging task as $j^{\uparrow,\downarrow}$ is not directly accessible by experimental methods and the available measurement techniques deliver different results depending on the probed transport regime [23]. Commonly used techniques are Andreev reflection [24], spin-resolved photoemission and spin polarized tunneling [25]. For the ferromagnetic transition metals and their alloys, such as Permalloy, the degree of spin polarization lies in the range of about 20% to 60%.

When a spin-polarized current leaves a ferromagnet (FM) across an interface with a normal metal (NM) the current becomes unpolarized. Spin-flip scattering relaxes the spin-imbalance while the electrons travel into the NM. The depolarization requires that spin-up (majority) electrons accumulate close to the interface as more of these electrons need to flip their spin. This leads to a phenomenon called spin accumulation [26]. As the spin-flip scattering depends on the electronic properties of the NM, the accumulation decays over a material-specific length, the so-called spin-diffusion length l_s. Typical values of l_s for normal metals range from tens of nm (Au) to about 1 µm (Al) [27].

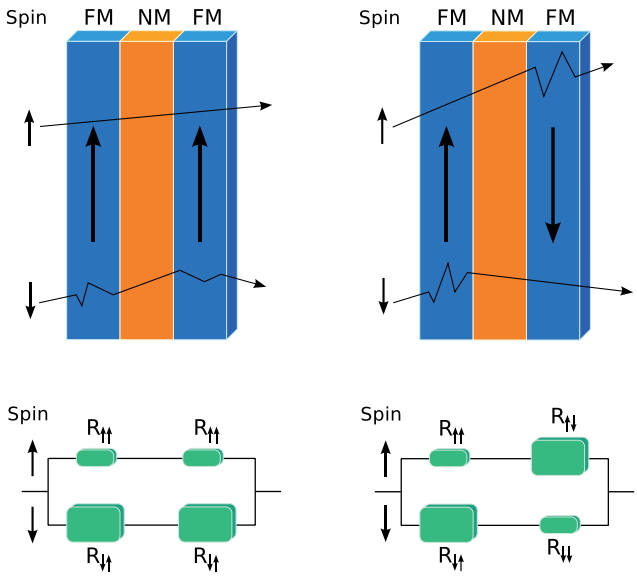

Figure 1.1 | Schematic illustration of the GMR effect. Solid lines represent simplified electron paths through the F/NM/F multilayer, illustrating the magnetization-dependent scattering. Left panels: low resistance state for parallel magnetization alignment due to shortcut via spin-down electrons. Right panels: High-resistance state for anti-parallel magnetization alignment due to strong scattering in both spin channels. The bottom panels show the equivalent circuit diagrams. Figure taken from [28].

Giant magnetoresistance

The giant magnetoresistance (GMR) effect [7, 8] is observed in magnetic multilayers of the structure F1/NM/F2, where F1 and F2 are ferromagnetic layers that can be switched independently and NM is a thin normal metal spacer (see Figure 1.1). The two-channel model discussed above directly provides a simplified explanation for this effect: For a parallel magnetization alignment (P state) of the two magnetic layers, spin-up electrons can travel through both layers as majority electrons, i.e. through the low resistance channel, whereas spin-down electrons suffer from significantly stronger scattering in both layers. The spin-up channel thus provides a conductivity shortcut, leading to a low overall resistance of the multilayer. In the antiparallel (AP state) configuration however, both spin channels are strongly scattered in one of the layers, leading to a significantly higher resistance. Such a spin-valve (i.e. a structure where F1 is fixed and F2 can be switched) is characterized by the magnetoresistance ratio

$$\mathrm{MR} = \frac{R_{\mathrm{AP}} - R_{\mathrm{P}}}{R_{\mathrm{P}}} \,, \tag{1.4}$$

which can reach more than 100 % in special multilayer structures [29]. The angle-dependence of the effect is given by

$$R = R_{\mathrm{P}} + \Delta R(1 - \cos\theta)/2 \,, \tag{1.5}$$

where θ is the angle between the magnetization of the two ferromagnetic layers.

Tunneling magnetoresistance

If the NM spacer layer (see Figure 1.1) is replaced by an insulator (I) such as Al_2O_3 or MgO, a GMR spin valve becomes a magnetic tunnel junction (MTJ). Similar to a GMR device, in a TMR device the total (tunneling) conductance through the barrier depends on the relative magnetization of the FM layers: the conductance is high in the P state and low in the AP state. Based on a simple model, the Jullière formula [30] provides a rough estimate of the TMR as a function of the spin polarization of the two electrodes P_1 and P_2:

$$\mathrm{TMR} = \frac{2P_1P_2}{1-P_1P_2}\,. \tag{1.6}$$

A more accurate model was developed by Slonczewski by taking into account the thickness and the height of the tunnel barrier [31]. It predicts a tunneling conductance through the F/I/F structure of

$$G = G_0\left(1+P_{\mathrm{eff}}^2\cos\theta\right), \tag{1.7}$$

where G_0 denotes the tunneling conductance without spin-split bands and P_{eff}^2 is an effective tunneling spin polarization of the barrier and the electrodes. Despite the limited applicability of these models to modern (single-crystalline) barrier materials such as MgO [32, 33], the result demonstrates the importance of the concept of spin polarization also in the tunneling regime.

1.2 Magnetic domain walls in nanostructures

The local spins in a ferromagnet are aligned by the exchange interaction. It is well known, however, that most macroscopic ferromagnets in equilibrium have a net magnetic moment much lower than that at saturation. This phenomenon has been identified by Weiss as arising from the formation of magnetic domains of different uniform magnetization orientation that are separated by transition regions, the domain walls (DWs). The way a ferromagnet forms magnetic domains depends on the various energy terms that describe a magnetic object [14, 34]. The deciding factor for the formation of domains is the magnetostatic energy due to the demagnetization field. It reaches a minimum for zero net sample magnetization, making a uniform magnetization of the sample energetically highly unfavorable.

The size of a DW is governed by the competition between the exchange interaction E_{ex} and the anisotropy energy E_{an}. While E_{ex} tends to align neighboring spins in parallel (wide wall), E_{an} is minimized for a maximum number of spins aligned with the anisotropy axis (narrow

wall). Minimizing the total DW energy yields a wall width of

$$w = \pi\sqrt{\frac{A}{K}} \tag{1.8}$$

and a wall energy per unit area of

$$\sigma_{\mathrm{w}} = 2\pi\sqrt{AK}, \tag{1.9}$$

where A is the exchange stiffness and K is the anisotropy energy density. For a soft ferromagnet (e.g. Permalloy) with $K \approx 10^3\,\mathrm{J\,m^{-3}}$ and $A \approx 10^{-11}\,\mathrm{J\,m^{-1}}$, typical DW widths are on the order of $\sim 100\,\mathrm{nm}$. It is interesting to note that the wall energy is proportional to the area of the wall. This causes DWs to form flat sheets and makes pinning of DWs at geometrical features such as notches possible. For the same reason, a magnetic nanocontact (i.e. a narrow constriction) will always act as a deep potential minimum for DWs in its vicinity.

Technological applications involving DWs (e.g. data storage [35] or logic circuits [36]) as well as more fundamental studies (e.g. on domain wall MR or current-induced DW motion [37]), require very well-defined shapes and precise positioning of DWs. Due to the growing influence of the geometry on the magnetization when shrinking device dimensions, nanostructures offer a very versatile way to tailor DWs [11, 34, 38]. In particular structures made of magnetically soft materials such as Py can be engineered to accommodate only certain types of DWs pinned at very specific positions along a nanowire with a well-defined pinning potential.

Patterned magnetic thin films (except films with perpendicular anisotropy) mostly form Néel-type walls where the magnetization rotates parallel to the film plane. The magnetization tends to stay aligned with the film plane due to the otherwise strong demagnetizing field. Two major types of DWs exist in magnetic nanowires: transverse and vortex walls [11, 39]. It mainly depends on the ratio between width and thickness of the wire whether one or the other is energetically favored. Figure 1.2 shows the simulated magnetization structure of a transverse (a) and a vortex (b) wall pinned in a half-ring wire. The bottom panels illustrate how both types of walls are attracted to a notch in the structure.

It is known from experiments that the width of a pinned transverse wall can be drastically reduced by shrinking the size of the constriction [40]. As pointed out in Reference [41], Equation (1.8) is no longer valid in nanoconstrictions. Despite the drastic increase in exchange energy density within a pinned DW, the overall cost in exchange energy can be lower for a squeezed DW as it occupies a much smaller volume. As a result, the DW width is of the order of the constriction size ($w \sim d$).

Therefore, magnetic nanocontacts are particularly useful for studying phenomena in very narrow DWs. Magnetic ring structures (or parts of rings) like the one shown in Figure 1.2 have proven to be a suitable geometry for the efficient and controlled positioning of DWs [11, 42].

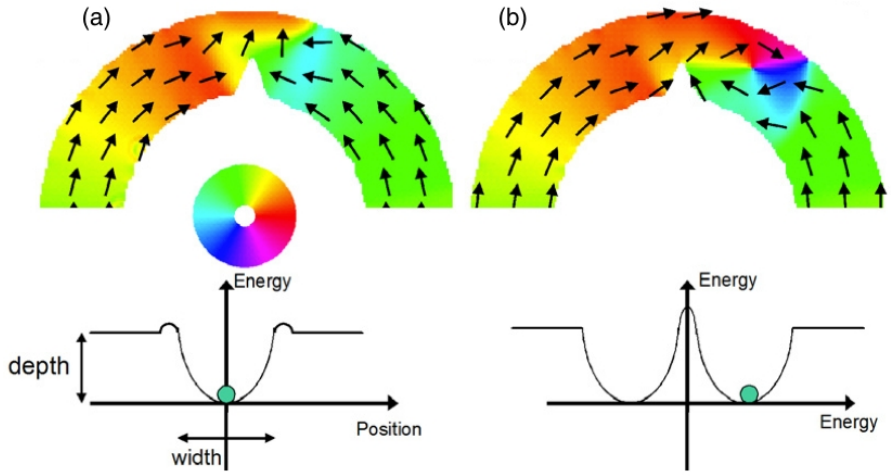

Figure 1.2 | Pinning of domain walls in notched nanowires. Simulation of the DW types predominantly occurring in magnetic nanowires (annular as well as straight wires): Magnetization profile and pinning potential of (a) transverse and (b) vortex DW. While transverse walls are attracted to the center of the notch, the potential minimum for vortex walls is to either side of the notch. Figure taken from [11].

The experiments presented in this part of the thesis rely on a combination of such annular wires with extremely small constrictions, as will be explained in more detail in Chapter 2.

1.3 Transport properties of metallic nanocontacts

In macroscopic metallic conductors the electrical resistance is given by Ohm's law. In the simplest case of a conductor of cross-sectional area A, length l and resistivity ρ (which is generally temperature-dependent) the resistance is $R = \rho \frac{l}{A}$. Maxwell was the first who used Ohm's law to calculate the resistance of a metallic constriction of variable geometry [43]. In the limiting case where the contact is a simple orifice of diameter d in a non-conducting plate separating metallic leads, the resistance yields the so-called *Maxwell resistance*

$$R = \frac{\rho}{d} . \tag{1.10}$$

These expressions are valid in the classical limit, where the characteristic length scale d of the sample is much greater than the elastic mean free path of the electrons l_e. In this conduction regime electrons scatter many times on their way through the contact. For the metals considered in this study, the dominant scattering mechanism at room temperature is phonon-electron scattering. Only at very low temperatures (when phonons are frozen out) also scattering off impurities and magnons (spin waves) plays a more significant role. This regime, where $d \gg l_e$, is called *diffusive*.

However, when the size of the contact is smaller than the mean free path, i.e. $d < l_e$, electrons may pass through the contact without being scattered and hence without changing their

momentum. This conduction regime is called *ballistic*. For ferromagnetic metals l_e is typically very small, requiring extremely small contacts to observe ballistic conduction (l_e is of the order of a few nm, e.g. for Py $l_e \approx 1\,\text{nm}$ [44]). Sharvin developed a semi-classical model to describe conduction in this regime [45]. The so-called *Sharvin conductance* is given by

$$G_S = \frac{2e^2}{h}\left(\frac{k_F r}{2}\right)^2 , \tag{1.11}$$

where h is Planck's constant, k_F is the Fermi wave vector and r is the contact radius. Hence, the conductance of a ballistic contact is independent of the mean free path and the resistivity, but depends only on the Fermi surface (i.e. the electron density) and the contact size.

An expression for the contact resistance that covers both the diffusive and the ballistic regime (by combining Equations (1.10) and (1.11)) was derived by Wexler [46]:

$$R_W = \frac{4}{3\pi}\frac{\rho l_e}{r^2} + \gamma\frac{\rho}{2r} \qquad \text{with} \quad \gamma = \frac{1+0.83(l_e/r)}{1+1.33(l_e/r)} , \tag{1.12}$$

where ρ is the bulk resistivity and r is the contact radius. As one can readily see, the two terms of Equation (1.12) represent the contributions from the diffusive (first term vanishes for $r \gg l_e$) and the ballistic (second term becomes negligible for $r \ll l_e$) conduction regimes. We will employ this expression later when we analyze the evolution of the MR as a function of contact size and resistance.

The smallest possible metallic contacts consist of only one or a few atoms at their narrowest point, resulting in an effective contact size on the order of 1 nm or less. As this is comparable with the Fermi wavelength in metals (e.g. in gold: $\lambda_F = 0.52\,\text{nm}$) the transverse momentum of the electron waves propagating through the contact becomes quantized (similar to an electromagnetic wave traveling through a wave-guide). This situation cannot be satisfyingly described by the (semi-)classical models introduced above, but requires a full quantum mechanical treatment. One of the first and most widely used theories of this kind is the scattering approach developed by Landauer [47]. It predicts that a perfect single mode conductor has a finite resistance of $h/2e^2 \approx 12.9\,\text{k}\Omega$. In general, the phase-coherent conductance through a nanocontact at zero temperature is given by

$$G = G_0 \sum_n \tau_n = \frac{2e^2}{h}\sum_n \tau_n \tag{1.13}$$

where τ_n is the transmission probability of the n^{th} occupied (i.e. conducting) mode and G_0 is the conductance quantum (for a spin-degenerate conductance channel). This result is in stark contrast to classical models that would predict zero resistance in the absence of scattering.

Although conductance quantization effects are not addressed in our experiments, it should be noted that such effects have indeed been observed in a wide range of metals using different

experimental approaches (see Section 1.4), both at cryogenic temperatures and even at room temperature (for a review of this topic see Ref. [15]). The situation is more complicated in the case of ferromagnetic metals. Intuitively, one would expect that the strong exchange interaction (see Section 1.1) lifts the spin-degeneracy, leading to fractional quantization of the conductance in steps of $\Delta G = e^2/h$ instead of $2e^2/h$. While some claim that several magnetic metals (Fe, Co and Ni) and even non-magnetic metals (Pt) exhibit such fractional quantization [48, 49], others raised concerns over potential artifacts due to impurities and adsorbates in the contact region [50] that could induce similar effects.

1.4 Fabrication of metallic nanocontacts

Metallic nanocontacts can be fabricated using a number of different techniques. In this section we briefly review the most widely used approaches and discuss them in terms of achievable quality, stability and reliability of the resulting contacts.

Spear-anvil technique

The first and most simple technique was pioneered in 1980 by Jansen [51]. In a spear-anvil contact (also called pressure-type contact) the nanocontact is established between a clean metal surface, the anvil, and a sharply etched metal wire, the spear, by pressing the wire onto the surface. The distance between the surface and the wire is usually controlled by a differential-screw mechanism and the wire can be spring-loaded for better control of the contact pressure. The entire sample holder is often immersed in liquid Helium in order to improve the contact stability and reduce thermal noise. Typical contact sizes range from 10 to 100 nm.

The main advantage of the spear-anvil technique is its simplicity and versatility as it requires almost no sample preparation. However, control of the contact diameter is strongly limited and finding the desired contact resistance is mostly a random process. The technique is therefore not suitable for systematic studies of transport phenomena as a function of contact size.

Scanning tunneling microscope

While the scanning tunneling microscope (STM) is a very well established tool for characterizing the topography and the electronic properties of conducting surfaces (for a review see Ref. [52]), it can also be used to study nanocontacts. The piezoelectric control of the tip-surface separation allows for a very precise approach of the tip, such that sub-nm contacts can be easily established [53] and studied [54]. The main disadvantage of STMs compared to the methods described in the following is that it takes sophisticated (and expensive) vibration compensation to keep the contacts mechanically stable enough. This is because the mechan-

ical support connecting the two contact sides is usually far away from the nanocontact (~ cm). In addition to that, special cleaning procedures are required to avoid the presence of adsorbates or contamination on the contacting surfaces and custom shapes (on the μm scale) of the contacts are hard to implement.

Electrodeposition

Electrochemical junctions (ECJs) are fabricated using electrodeposition or electrodissolution by either filling a small gap (< 100 nm) between two predefined leads or dissolving material from a notched wire to shrink its diameter [55]. ECJs usually provide no long-term stability of atomic-sized contacts due to the continuous exposure to the electroplating solution. Also, due to the chemical reactions involved, ECJs cannot attain the same degree of purity and cleanliness as nanocontacts fabricated under cryogenic vacuum conditions. These drawbacks limit the use of this technique for clean and artifact-free studies of nanocontacts.

Mechanically controllable break junction technique

A mechanically controllable break junction (MCBJ) consists of a thin, notched metallic wire glued to or deposited on a flexible substrate (see Figure 1.3(a) for an illustration). The substrate is bent using a piezoelectric element, which causes the top surface of the substrate and thus the wire to expand until the contact breaks at the notch. This procedure is usually performed in a low-temperature vacuum environment so that the freshly exposed contact surfaces remain clean. The contact separation as well as the contact size can then be precisely controlled by the piezoelectric actuator.

The MCBJ technique has proven to be extremely successful for studying nanocontacts [15]. One of the main advantages is the low displacement ratio between the movement of the piezo-element and the displacement of the contact faces. This ratio can be as low as $r_d \sim 10^{-4}$ in micropatterned MCBJs, implying that the displacement can be controlled with better than pm-precision. Once a clean fracture is established, the contact can be closed and opened many times, opening the possibility for statistical studies. It is particularly useful for magnetic studies that the notched wire can be patterned into almost any desired shape using micro and nanofabrication techniques. The MCBJ technique is also very robust against vibrations, mainly because the free-standing part of the leads is of the order of only 1 μm. However, this remaining free-standing length is at the same time one of the major drawbacks for studies involving magnetic materials. Magnetostriction in these parts of the contact can lead to highly undesirable artifacts, as we will discuss in more detail in Section 1.5.

Electromigration

Electromigration (EM) is a phenomenon that describes the transport of material in a conductor subject to very high current densities (typically ~ $10^{12}\,\mathrm{A\,m^{-2}}$). The effect is due to two distinct

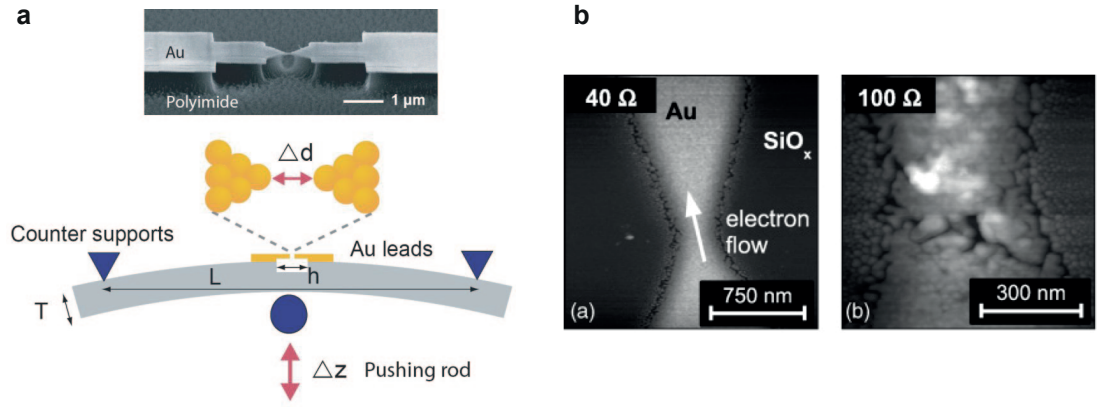

Figure 1.3 | Fabrication techniques for nanocontacts. (a) Schematic illustration of the mechanically controllable break junction (MCBJ) technique: The piezoelectrially controlled pushing rod bends the flexible substrate, which then pulls the two ends of the notched Au wire apart, gradually reducing the contact diameter and eventually leading to a broken contact. Illustration taken from http://www.nanoelectronics.ch/research/molecular.php. (b) AFM images taken prior and after electromigration of a constricted Au wire. Figure taken from [57].

forces acting on the atoms of the conductor [56]: First, the *direct force* $\mathbf{F}_d = Z_d e\mathbf{E}$ due to the electrostatic interaction of the atom with the electric field $\mathbf{E}$. Second, the momentum transfer to the lattice by scattering charge carriers, resulting in the so-called *wind force* $\mathbf{F}_w = Z_w e\mathbf{E}$. Z_w and Z_d denote the material-dependent effective charges (of the lattice ions). In most cases, the wind force dominates over the direct force as $Z_w \propto 1/\rho$ and thus $Z_w \gg Z_d$ in good conductors with low resistivity ρ. Under these conditions, EM will lead to a transfer of atoms in the direction of the electron flow.

For a long time since its discovery in the 19th century by Gerardin, research in the field of EM focused solely on the role of EM as a failure mode of metal interconnects in integrated circuits [58]. As feature sizes continued to shrink and current densities increased, EM posed a serious problem to the reliability of integrated circuits (ICs). However, if properly controlled, the effect can also be exploited for the fabrication of nanocontacts and nanogaps. By passing a large current through a wire with a constriction, the wire heats up at its narrowest point. As soon as the critical current density is reached (typically $j_{\text{crit}} > 1 \times 10^{11}\,\text{A}\,\text{m}^{-2}$), EM sets in at this position and leads to thinning of the constriction [59]. The resulting increase in resistance of the constriction further increases the current density and hence the power dissipation at the constriction. Unless precautions are taken, the contact can easily break in this moment due to the so-called 'thermal runaway', an uncontrolled and rapid increase in temperature leading to melting, island formation and consequently an uncontrollable fracture in the wire [60].

Several techniques have been developed to avoid the thermal runaway and to obtain a nanocontact of specific size or a small nanogap (~ 1 nm) suitable for molecular electronics [61]. Analog [62] or computer-controlled [63, 64, 65] feedback control has proven to be very reliable in controlling the temperature of the contact. Limiting the resistance of the

leads can also drastically improve the reliability of the EM process [60]. Several studies have demonstrated the reliability of the technique down to the quantum conduction regime (e.g. [60, 65, 63]), highlighting its suitability even for atomic nanocontacts.

It is of fundamental interest to correlate the precise (atomic) shape of a nanocontact with its physical behavior. As there are no moving parts involved, EM can easily be combined with (real-time) imaging of the contact formation using tunneling electron microscopy (TEM) [66, 67] or scanning probe microscopy (SPM) [57]. Such imaging studies provide a better understanding of the evolution of the contact during EM and ultimately allow for the precise measurement of the size of the contact or gap formed by EM (see Figure 1.3(b)). Importantly, such imaging studies confirm that the length of the suspended part of the contact is considerably shorter than in MCBJ contacts ($l_{\text{free}} \sim d_{\text{contact}}$). Keeping the suspended parts of the contact as short as possible is key to increasing the stability and reducing artifacts due to magnetostriction (see Section 1.5). Therefore, this is one of the main advantages of the EM-fabricated nanocontacts over MCBJs. In addition to that, EM can be performed automatically and in parallel on a large number of junctions, making it an interesting candidate for technological applications in data storage. The only clear disadvantage compared to the more widely-used MCBJs is that EM is not suitable for repetitive opening and closing of atomic contacts, preventing its use as a statistical tool in the quantum regime.

1.5 Magnetoresistance in magnetic nanocontacts

A variety of different MR effects can be observed in magnetic nanocontacts. In this section, we will review the most relevant effects and provide a summary of available theoretical models and experimental studies.

1.5.1 Theoretical models

Anisotropic magnetoresistance

The anisotropic magnetoresistance (AMR), discovered by W. Thomson in 1856 [68], was the very first discovered MR effect. It describes the dependence of the electrical resistivity of a ferromagnetic sample on the angle θ between the magnetization $\boldsymbol{M}$ and the electrical current density $\boldsymbol{j}$. In a homogeneously magnetized sample, the resistivity reaches a maximum $\rho_{\parallel}$ for $\boldsymbol{M} \parallel \boldsymbol{j}$ and its minimum $\rho_{\perp}$ for $\boldsymbol{M} \perp \boldsymbol{j}$. In general, the angle-dependent resistivity is given by

$$\rho(\theta) = \rho_{\perp} + \Delta\rho_{\text{max}} \cos^2\theta \qquad \text{with} \quad \Delta\rho_{\text{max}} \equiv \rho_{\parallel} - \rho_{\perp} \,. \tag{1.14}$$

The AMR ratio $\Delta\rho/\rho$ is on the order of a few percent for most ferromagnetic metals and it is particularly strong in alloys such as Py. As the AMR depends directly on the magnetization in an otherwise homogeneous material, it can be used as a very sensitive probe for the detection of domain walls in magnetic nanostructures [42].

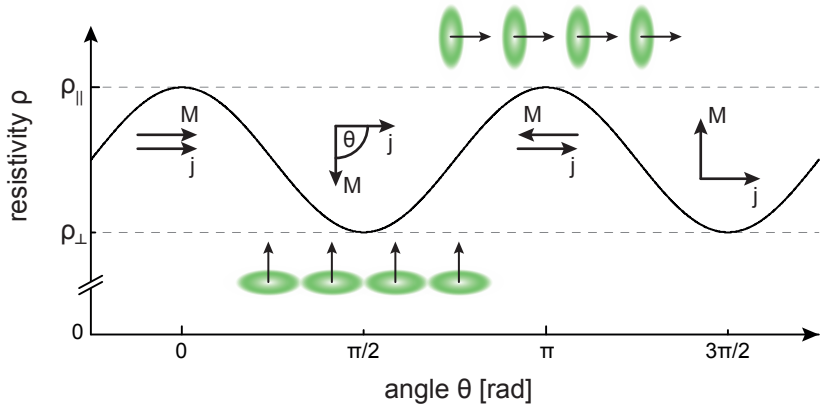

Figure 1.4 | Angle-dependence of the AMR effect. The solid line shows the $\cos^2\theta$ angle dependence of the AMR, where θ is the angle between the current density $\boldsymbol{j}$ and the magnetization $\boldsymbol{M}$. Sketches illustrate the coupling between the direction of the local spins (black arrows) and the anisotropic charge distribution due to the spin-orbit interaction (see text).

At the origin of the AMR is the spin-orbit interaction that, despite the hybridization-induced quenching of the orbital moment in itinerant 3d-ferromagnets (see Section 1.1), results in an orbital character of the total magnetic moment. As 3d orbitals are highly anisotropic, this orbital part leads to an anisotropic charge distribution coupled to the direction of the magnetic moment (see simplified illustrations in Figure 1.4). As the magnetization is rotated, the orientation of available d-states (distribution of k-wave vectors) required for s-d scattering events and thus the scattering rate itself change. This in turn gives rise to the discussed angle-dependence of the resistivity – the AMR. A more rigorous and detailed derivation of the effect can be found in Reference [69].

Domain wall magnetoresistance

The domain wall magnetoresistance (DWMR) (also called domain wall resistance (DWR)) describes a change of the electrical resistance of a ferromagnet induced by the presence of a DW. While there is a clear conceptual distinction between DWMR and the AMR, the two effects are often hard to distinguish experimentally: On the one hand, the DWMR arises from additional electron scattering in rapidly changing magnetization structures. There is experimental evidence that it explicitly depends on the size of the DW, or in other words, it depends on how quickly the magnetization changes when an electron travels through a DW. On the other hand, the AMR does also occur in DWs, but only due to the changing angle θ between magnetization and current density ($\Delta\rho \propto \cos^2\theta$). In contrast to DWMR, the AMR does not depend on the gradient of the magnetization.

Cabrera and Falicov were the first to theoretically predict such an additional resistance term [70] based on a so-called 'paramagnetic effect' spin scattering model. A DW, i.e. a rotation of **M** by 180°, can be considered as an exchange of the spin-up and spin-down bands on either

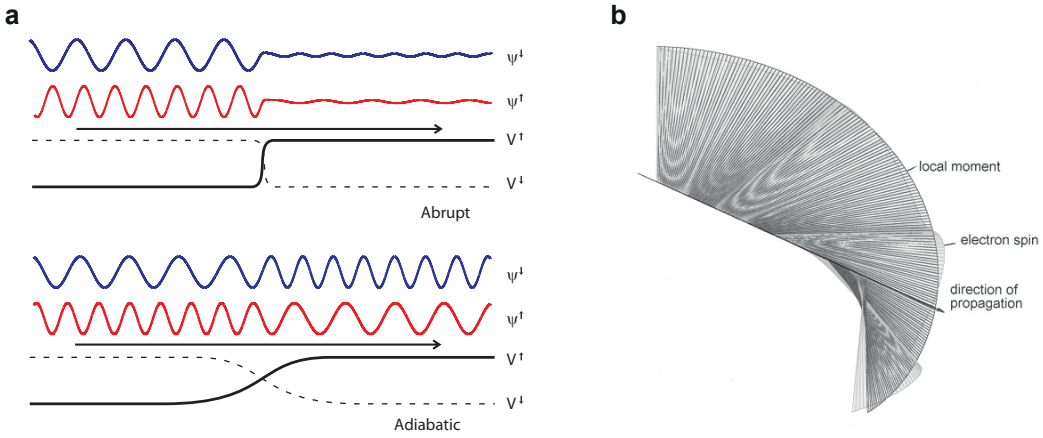

Figure 1.5 | DWMR models proposed by Cabrera/Falicov and Viret. (a) Cabrera/Falicov-model: Spin-resolved potential profiles $V^{\uparrow,\downarrow}$ and resulting wavefunctions $\Psi^{\uparrow,\downarrow}$ at abrupt and wide domain walls. The drastically reduced transmitted amplitude of the electron wave function in the case of an abrupt DW (upper panel) gives rise to DWMR. (b) Viret-model: Numerical simulation of the spin precession and the resulting misalignment between the electron spin and the local moment during traversal of the DW. Figures taken from [14] and [72].

side of the DW. An electron traveling from one side to the other will thus see a potential step with height E_{ex}, based on which electron transmission probabilities can be calculated (see Figure 1.5). While there is negligible reflection of the electron wave functions for a wide DW (adiabatic case), it was predicted that an abrupt DW can drastically reduce the transmission through the DW and give rise to a DWMR of $\Delta\rho/\rho \propto e^{-\pi k_F w}$. However, both Cabrera and Falicov, as well as Berger [71], found that the wall thickness w has to be on the order of the Fermi wavelenth ($\lambda_F \sim$ Å) for the effect to be measurable. As this corresponds to atomically abrupt DWs, the model was discarded as an explanation for early experimental observations of the DWMR in rather large DWs.

More recently, Viret et al. proposed a semi-classical model for DWMR based on the pseudo-Larmor precession of the conduction electron spin about the changing exchange field direction within the DW [72, 73]. The precession causes the orientation of the spin and the local magnetization to be slightly misaligned for small enough DWs (see Figure 1.5). In analogy to GMR and the two-channel model (cp. Section 1.1), this leads to additional scattering, which can be expressed by an effective mean free path as a function of the mis-tracking angle θ_s between the orientation of the spin and the local magnetization, according to

$$l(\theta_s) = \frac{\bar{l}}{1 + P^2 + 2P\cos\theta_s}\,, \tag{1.15}$$

where $\bar{l}$ is the average electron mean free path and P the spin polarization. By estimating the

average of θ_s for the passage of an electron through a DW of width w, the MR was shown to be

$$\frac{\Delta R}{R} = \frac{2P}{(1-P)^2}\left(\frac{2\pi\hbar v_\mathrm{F}}{E_\mathrm{ex}}\right)^2 \frac{1}{w^2}\,, \tag{1.16}$$

where v_F is the Fermi velocity and E_ex is the exchange energy. This result predicts rather small MR values for realistic wall widths in the diffusive regime (e.g. $\Delta R/R \approx 3\times10^{-4}$ for $w = 15\,\mathrm{nm}$ in Co, and 4×10^{-5} for $w = 100\,\mathrm{nm}$ in Ni).

A fully quantum mechanical approach to treat the problem of DWMR and to clarify its origin was published shortly later by Levy and Zhang [13]. According to their model, the DWMR arises from increased impurity scattering due to the mixing of spin-↑ and spin-↓ states within a narrow DW (i.e. in the case of non-adiabatic transport with nonzero θ_s). This largely confirms the results of Viret et al. discussed above, and in particular the predicted proportionality of DWMR $\propto 1/w^2$. Further theoretical confirmation of this behavior was provided by Brataas et al., who calculated the DWMR based on a two-band Stoner model [74] in the diffusive and the ballistic transport regime. Sizable positive DWMR signals on the order of ~ 1 % for realistic DW widths were predicted to appear only in the diffusive limit for strongly asymmetric spin lifetimes.

Other theoretical models have also predicted a negative DWMR, i.e. a decrease in resistance due to the presence of a narrow DW. Tatara et al. [75] attributed negative DWMR to a weak localization effect, where the quantum contribution to the resistivity is reduced by the decoherence of the electrons due to the presence of a DW. However, such effects are only expected to be significant in the quantum regime and at very low temperatures. Furthermore, DWMR of either sign (depending on the asymmetry of spin-dependent scattering lifetimes) has been predicted by van Gorkom et al. [76] by taking into account DW-induced changes in the electronic structure. *Ab initio* studies such as the ones in References [77, 78] generally support the results of most analytical models in that narrower DWs are assumed to give rise to higher DWMR. For instance, up to 60 % positive DWMR has been predicted in [78] for extremely narrow DWs that measure only a few atomic planes in width.

However, a consistent prediction of the magnitude, the sign and the width-dependence of DWMR in the diffusive regime across the various models (see References [14, 79] for an overview) does not exist. This highlights the importance of reliable experimental demonstrations of these effects (see below).

Very large MR in nanocontacts

Experimental reports about extremely large MR in nanocontacts (e.g. more than 200 % [80] or even larger [81, 82], see below) reignited the search for applicable theoretical models, this time more focused on the ballistic transport regime in atomic nanocontacts, where extremely narrow DWs can be generated (see Section 1.2). Inspired by its occurrence in the

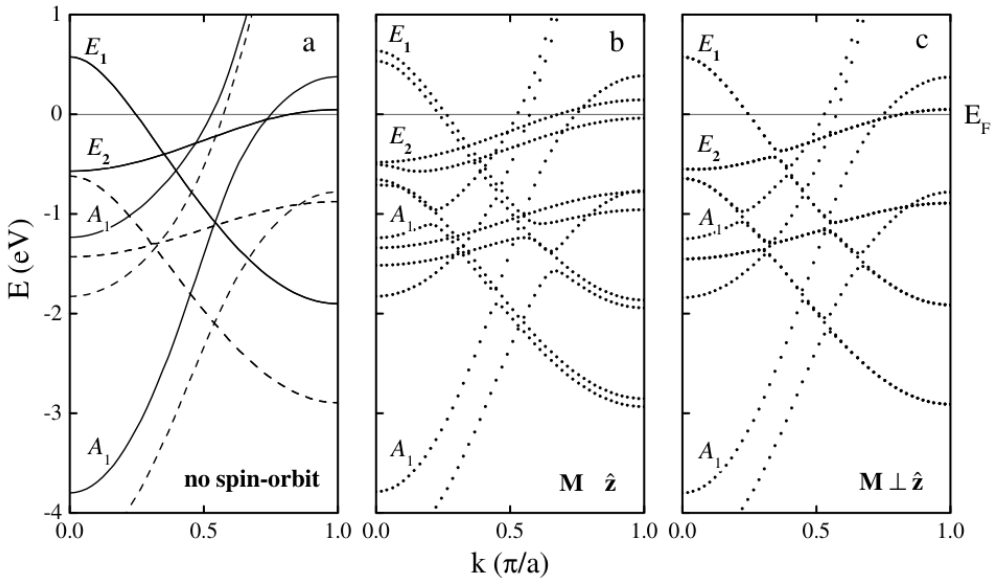

Figure 1.6 | Electronic structure of a monoatomic Ni wire, (a) without spin-orbit interaction, (b) with spin-orbit interaction and $\boldsymbol{M}$ aligned with the wire axis and (c) with $\boldsymbol{M}$ perpendicular to the wire axis. Dashed lines and solid lines in (a) denote the majority-spin and minoritiy-spin bands, respectively. Figure taken from [88].

ballistic regime, the effect is sometimes called **ballistic magnetorestistance (BMR)**. While some theoretical models could reproduce such spectacularly large DWMR effects [83, 84], others claimed that such MR values cannot be attained for realistic atomic structures and magnetization configurations of atomic nanocontacts [85, 86, 87].

Many of the developed theoretical approaches are based on the Landauer theory (see Section 1.3) as it permits the calculation of the total conductance in the quantum conduction regime by summation over the available propagating channels. Calculations of this kind require the (numerical) derivation of the full electronic band structure of the contact as it is the number of bands crossing the Fermi level that determines the number of conducting channels. The precise band structure of low-dimensional structures, however, depends sensitively on the details of the atomic structure, which is hard to determine experimentally. A basic example is given in the following:

For a simple (but rather unrealistic) one-dimensional monoatomic Ni wire one obtains the electronic structure shown in Figure 1.6 [88]. Similar results were obtained for chains of Fe atoms [89]. Spin and orbital moments in such chains are expected to be strongly enhanced, giving rise to stronger spin-orbit interaction. It was shown that the bands arising from the coupling of 3d-orbitals (E_1 and E_2 in Figure 1.6) become spin-split by the spin-orbit interaction when the magnetization points along the wire axis, while they are almost degenerate for a perpendicular alignment. Based on the assumption that each band crossing, i.e. each non-degenerate channel, contributes $G = e^2/h$, the total conductance is expected to change from $6e^2/h$ to $7e^2/h$ for a rotation of $\boldsymbol{M}$ by 90°. As this effect, just like the AMR, does not depend on

the presence of a DW, it is sometimes called **atomic** or **enhanced AMR** instead of BMR.

This simplified model demonstrates the general principle of studies of this kind. Later it was shown that more complicated atomic structures and magnetization configurations have to be considered to obtain more accurate and realistic results (e.g. [90, 91, 92, 93]). The general consensus of the most recent publications on the topic is that DWMR as well as BMR (or enhanced AMR) is expected to be on the order of a few to a few tens of percent in realistic geometries in the ballistic conduction regime, and that much higher MR values, as reported in some experiments (e.g. [80, 81]), must be ascribed to artifacts. The issue of artifacts in DWMR measurements will be discussed in more detail in the following section where we review some of the most relevant experimental studies.

1.5.2 Experimental studies

Diffusive conduction regime

All experimental demonstrations of DWMR face a common challenge: the intrinsic and often very small DW-induced effect occurs simultaneously with other MR effects, such as the AMR. Depending on the experiment, this can either obscure the DWMR or, in the worst case, lead to wrong conclusions about sign and magnitude of the DWMR effect. A wide range of different experimental approaches have been developed that aim at separating the different contributions to the overall MR. A selection of the most successful and reliable ones is presented in the following.

A study on DWMR in Co and Ni films by Viret et al. [72], one of the first of its kind, illustrates very well how difficult it is to detect DWMR in unpatterned thin films of soft magnetic materials. Figure 1.7(a) shows the MR measurements on one of the films investigated. In both, the longitudinal (R measured along the applied field) and the transverse (R measured perpendicular to the applied field) geometry, the measurement is clearly dominated by AMR. The peaks and dips indicate the magnetization reversal of the film at the coercive field $\pm H_c$. In the absence of any MR effect other than AMR the two curves should add up to a constant. The observed positive deviation from this constant value (shown in Figure 1.7(b)) was attributed to additional scattering due to DWs and an explanation based on the spin mistracking model (see above) was put forward. However, without detailed knowledge of the micromagnetic behavior of the sample, AMR could not entirely be ruled out as the origin of the effect.

Among the various attempts to make DWMR measurements more reliable (for a review see Ref. [14]) two main strategies can be identified. First, the use of micro and nanostructures for improved control of the size and shape of the DWs: usually, these experiments are based on wires or other well-defined shapes made of soft magnetic materials with in-plane magnetization. Often, there is a small negative DWMR (e.g. based on simple Co or Ni wires [94, 95], zigzag-shaped Co wires [96], epitaxial Fe films with the magnetic easy axis across the wire [97] or Ni wires [98]). Others claimed that the drop in resistance can be entirely attributed to AMR

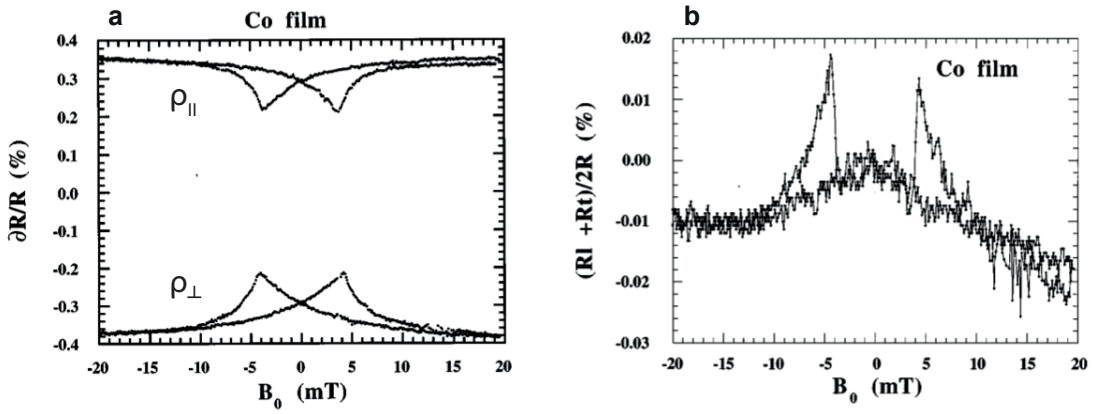

Figure 1.7 | AMR and DWMR in Co thin films. (a) MR measurements in transverse ($\rho_\perp$) and longitudinal ($\rho_\parallel$) geometries for a 28 nm thick Co film. (b) Domain-wall-scattering induced resistivity obtained by adding the transverse and longitudinal magnetoresistance curves. Figure taken from [72].

[99, 100, 101] or found evidence for a small positive contribution [102].

Second, employing highly anisotropic materials such as CoPt, FePt and Co opened the possibility of studying a large number of DWs in wires or films with stripe domain patterns. As these materials usually exhibit Bloch walls (see Section 1.2), experiments can be designed such that the magnetization always points perpendicular to the current direction, which avoids any influence by the AMR. A number of carefully designed studies revealed a small positive DWMR [103, 104, 105], qualitatively supporting the theoretical prediction by Levy and Zhang discussed above (DWMR $\propto 1/w^2$). However, in contradiction to this model, single DWs pinned in highly anisotropic Co nanowires were shown to induce relatively large positive DWMR [106].

More recently, Hassel et al. [107] and Aziz et al. [108] found strong evidence for quantitative agreement with the Levy and Zhang model in highly anisotropic Co/Pt multilayers. Controlled 'writing' of the domains using magnetic force microscopy (MFM) or focused ion beam (FIB) irradiation allowed them to determine the resistance change caused by the generation or annihilation of single DWs. Depending on the used material system and geometry the relative resistance changes observed were 1.8 % [107] and 0.1 % [108], in agreement with the theoretical model. The highest degree of control to date was achieved very recently by Franken et al. using a combination of Ga-FIB and magneto-optical imaging [12]: in addition to writing a controlled DW pattern in the Pt/Co/Pt strip (see Figure 1.8), the Ga irradiation dose was shown to locally tune the out-of-plane anisotropy and thus the DW width. The DWMR as a function of DW width showed excellent agreement with the predicted $1/w^2$ dependency, strongly supporting the validity of the Levy and Zhang model for Bloch walls in the diffusive regime.

In summary, it can be stated that a general consensus on the sign and magnitude of the intrinsic DWMR in the diffusive regime exists only for highly anisotropic materials where a

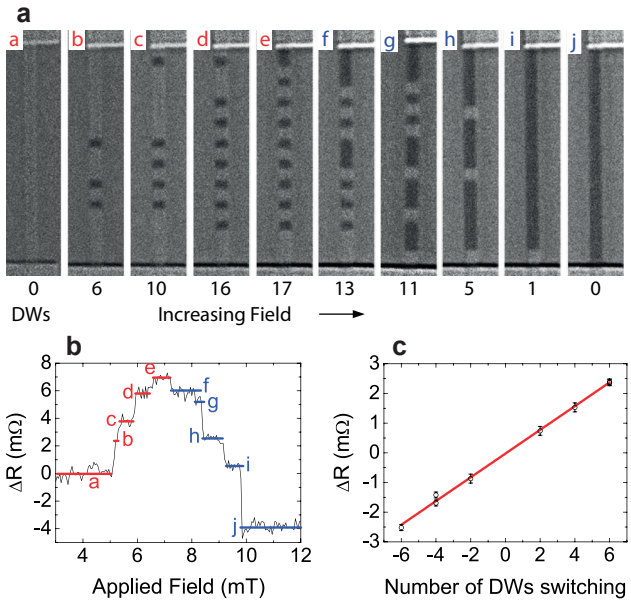

Figure 1.8 | DWMR measurements by controlled nucleation and annihilation of DWs in Pt/Co/Pt wires. (a) Kerr microscopy images recorded as a function of external magnetic field, showing nucleation and annihilation of magnetic domains at the previously irradiated positions (dark areas have inverted magnetization and correspond to irradiated areas) (b) Resistance as a function of field, showing discrete steps for each nucleation or annihilation of a DW. (c) Magnitude of resistance jumps as a function of number of DWs nucleating or annihilating. The slope represents the resistance increase due to a single DW. Figure taken from [12].

large number of very narrow DWs can be easily prepared. In this case the DWs were consistently shown to give rise to additional scattering, leading to a rise in the resistivity ($\propto 1/w^2$). The situation is less clear in the case of magnetically soft materials, where mixed results have been obtained – often due to issues related to separating the DWMR from other MR effects such as AMR. Thus, there is a clear need for more controlled and reliable studies on application-relevant materials like Py. We address this issue by our measurements of MR effects in nanocontacts of variable size (see Section 3.1).

Ballistic/quantum regime

Studying nanocontacts in the ballistic and quantum regime is an enormous experimental challenge in many respects. Structural and magnetic properties can be characterized sufficiently accurate only down to a contact size of a few nm using techniques such as AFM, SEM, MFM. While this is sufficient for diffusive contacts, obtaining reliable data about the magnetic and geometrical configuration on the atomic scale is much more difficult – in many cases completely impossible. Atomic contacts are also hard to fabricate in a reproducible fashion (see Section 1.4) and tend to be unstable at room temperature. Additionally, experiments of this kind often suffer from artifacts that are hard to detect. Unambiguous experimental observations of MR in the ballistic regime are therefore difficult to obtain and verify.

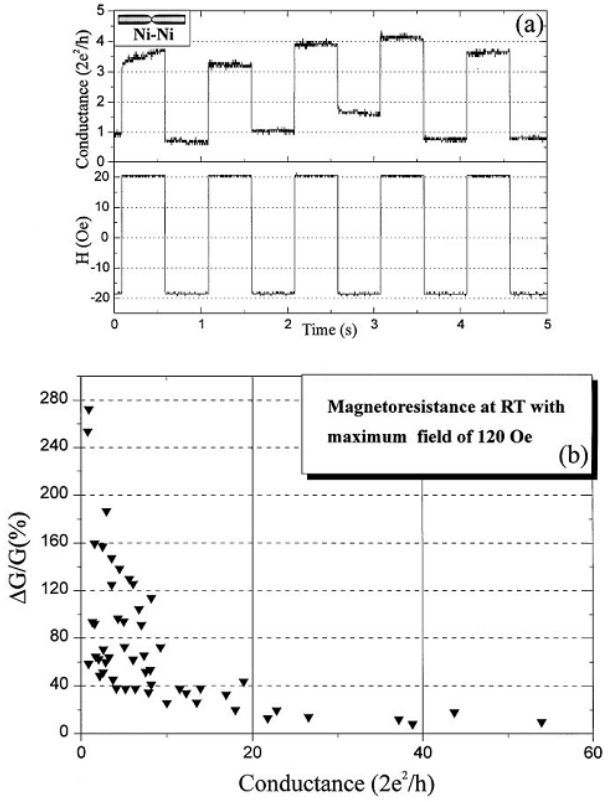

Figure 1.9 | Observation of large BMR in mechanically prepared Ni contacts. (a) Two nickel wires of millimeter radius are used to form a nanoconstriction. (b) Dependence of magnetoresistance on the conductance level: the applied magnetic field ranges from 20 to 120 Oe. Figure taken from [80].

Spectacularly high MR in ballistic nanocontacts was first reported by García et al. The authors claimed to observe more than 200 % BMR at room temperature in mechanically prepared [80] (see Figure 1.9) or electrodeposited [109] Ni contacts. Others supported these findings and reported even larger MR [81, 82]. These large effects were attributed to a DW-induced modulation of the transmission coefficients of the spin-polarized channels that contribute to the conduction in the quantum transport regime.

The observation of such large MR effects generated a lot of interest in DWMR in nanocontacts, in part owing to the huge potential this effect would have for technological applications. However, the results were heavily disputed as many had issues reproducing the effect. After years of debate, a publication by Egelhoff et al. brought most of the discussions to an end [110]: in a series of very carefully designed series of experiments it was shown that all of the reported extremely large BMR effects (> 200 %) could be attributed to artifacts due to magnetostrictive, magnetostatic and magnetomechanical effects.

Nevertheless research efforts in the field did not cease. However, being aware of the threats artifacts pose to reliable studies on MR in nanocontacts, greater care was taken in designing artifact-free and stable experiments. In addition to reducing magnetostriction and magne-

tostatic effects, a growing number of experiments was performed in vacuum and/or at low temperatures to reduce adsorbates in the contact region and avoid thermally excited atomic motion.

Several well-controlled experiments based on the MCBJ technique [111], electrochemical junctions [112] as well as electromigration [113] consistently reported MR effects of at most a few tens of percent for resistances on the order of one or a few conductance quanta e^2/h. In these experiments, relatively high magnetic fields prevented the controlled formation of DWs, which led some to the conclusion that BMR is the same phenomenon as enhanced AMR. In this picture, the observed change of resistance while sweeping the applied magnetic field is explained as arising from the rotation of the magnetic moments in the contact region (see section on theoretical models, [88, 89]).

Triggered by these results, Viret et al. systematically investigated the angle-dependence of the MR in Fe nanocontacts [89]. Stable contacts up to the ballistic conduction regime were established using the MCBJ technique. Figure 1.10 shows the main result, the evolution of the AMR with increasing contact resistance from the diffusive to the ballistic regime. In the diffusive regime (bottom panel, contact size about 10 atoms) the angle-dependence clearly shows the $\cos^2\theta$ behavior known from AMR in the bulk. Atomic contacts with resistances close to h/e^2 (top panels, presumably single atomic contacts of different local arrangement) exhibit strongly enhanced AMR of up to 75 % with a step-like angle-dependence. Recently, similar data from a series of MCBJ-based experiments was published by Egle et al. [114]. This lends strong support to the hypothesis of angle-dependent opening and closing of conduction channels [90], as discussed in Section 1.5.1.

Similar results were obtained by Sokolov et al. from electrochemical Co junctions that revealed reproducible abrupt switching between stable conductance values [115]. However, in a comment Shi and Ralph pointed out that the observed effect could be an artifact due to field-induced atomic motion giving rise to two-level fluctuations [116] (authors' response: [117]). In fact, the occurrence of such fluctuations in atomic-sized contacts is a well-known phenomenon [15] and should be explicitly ruled out in experiments on such contacts. Significantly lower MR values (only up to 14 %) with a strong bias-dependence were observed in a similar study on electromigrated Permalloy contacts [118]. Despite remaining differences between these experiments in terms of magnitude and angle-dependence of the MR, an enhancement of the AMR in atomic/ballistic nanocontacts seems to be confirmed.

Due to the additional degree of complexity and the increased risk of artifacts, to date very few have focused on the impact of a pinned DW on the resistance of a ballistic (atomic) nanocontact. Bolotin et al. [119] conducted a study of this kind with gradually electromigrated nanocontacts. They claimed to observe DWMR in line with the Levy and Zhang model in the diffusive regime, and enhanced DWMR of 10 % – 40 % in the ballistic regime. However, from the data presented in the paper it remains unclear if the magnetic switching consistently occurs in a controlled way. In the tunneling regime the observed TMR fluctuates between

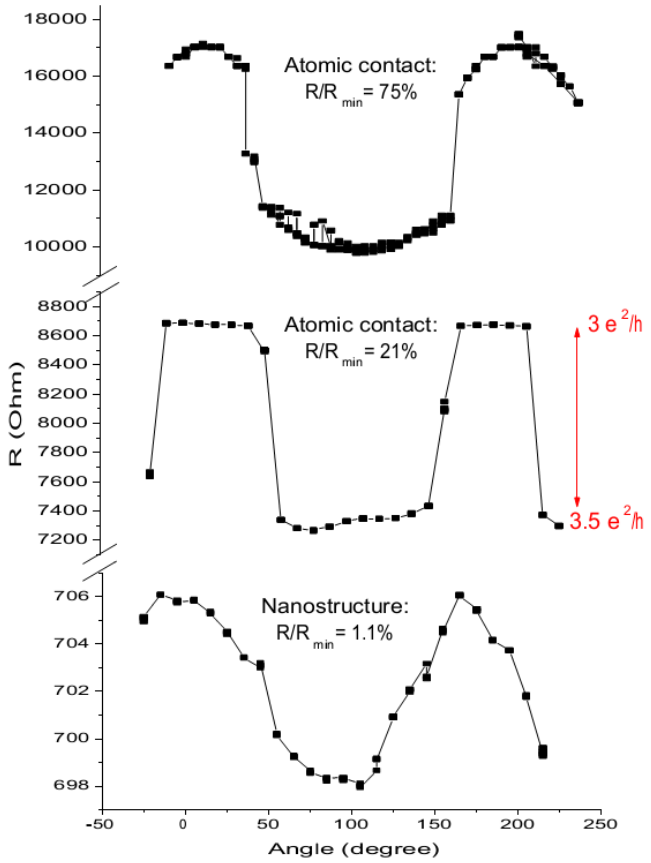

Figure 1.10 | Evolution of AMR in Fe MCBJs from the diffusive to the ballistic regime. Dependence of the resistance on the angle between magnetization and current for three Fe contacts of different size. A magnetic field of 2.5 T completely saturates the nanocontact for any given field angle. Figure taken from [89].

−10 % and 85 %.

More recently, Ben Hamida et al. performed MR measurements on constricted Fe wires to assess the intrinsic DWMR in atomic constrictions [120]. After modeling and subtracting the DW-induced MR, they report positive DWMR of up to 4 % in atomic contacts (up to 10 kΩ). The major shortcoming of this study is the possible contamination of the nanocontact region with impurities or adsorbates as experiments and fabrication were not performed under vacuum conditions.

Similar to the case of DWMR in the diffusive regime and the case of enhanced AMR in the ballistic regime, additional experimental as well as theoretical work is required to fully elucidate the nature of DWMR in the ballistic conduction regime. In view of the numerous reports on artifacts and the discussed difficulties in separating DWMR and AMR, carefully designed experiments that combine the highest degree of purity with the best control of the magnetization structure possible are needed.

2 Experimental techniques

Magnetoresistance measurements of magnetic nanocontacts have proven to be extremely sensitive to artifacts due to magnetostriction, contamination and instability (see Section 1.5). Moreover, controlling magnetization on the nanoscale can be a challenge by itself (see Section 1.2). It is therefore essential to develop both, a reliable fabrication process as well as a controlled and clean measurement environment. In the following we will discuss how we tackled these requirements.

2.1 Measurement and deposition chamber

The deposition and any measurements are performed in a custom-built ultra-high vacuum (UHV) chamber with a base pressure below 3×10^{-10} mbar. The combination of two high-throughput turbopumps with a Ti-sublimation pump and an ion getter pump ensures short pump-down times and a high-quality vacuum. Photos and a description of the main parts of the chamber are depicted in Figure 2.1. Each sample undergoes a bake-out procedure in the load-lock for 6 h at about 100 °C to reach the base pressure before it is transferred to the main chamber. The surface of the sample can then be cleaned (ion milled) using an ion gun installed in the main chamber.

The main chamber is equipped with four to six custom-built thermal evaporators for *in-situ* deposition of magnetic (Ni, Py) and non-magnetic (Cu, Au, Ho, etc.) materials (see Figure 2.2). Electrons emitted from the heating filament (99 % tungsten / 1 % thorium oxide) are accelerated to the evaporation rod by a potential difference of 0.5 to 1 kV. Typical values for the heating power required for evaporation at rates between 5 nm h^{-1} and 25 nm h^{-1} range from 10 to 25 W, depending on the material's vapor pressure characteristics. The evaporators are mounted on the bottom flange of the main chamber, facing up towards the sample. Prior to any deposition, each evaporator is outgassed and material is evaporated for at least one hour with closed deposition shutter to improve the purity of the deposited film.

For the best possible control of the magnetization configuration of the nanocontact we use a

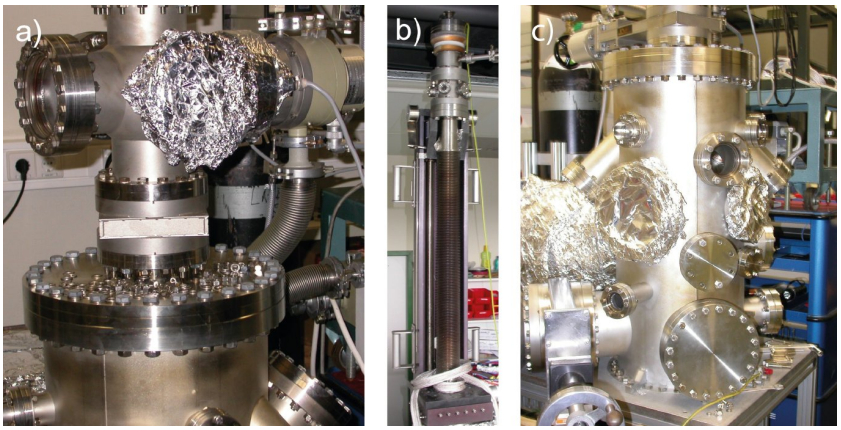

Figure 2.1 | Photos of parts of the UHV setup used for measurements and thin film deposition. Upper part of (a) shows the sample load-lock. Its bottom port leads to the main chamber (c) for measurements and evaporation, the top port is connected to the linear/rotational motion feedthrough (b) used for transferring the sample between load-lock and main chamber. The long vacuum bellow in (b) accommodates the cryostat. The topmost flanges in (b) provide electrical feedthroughs and connections to the cryostat.

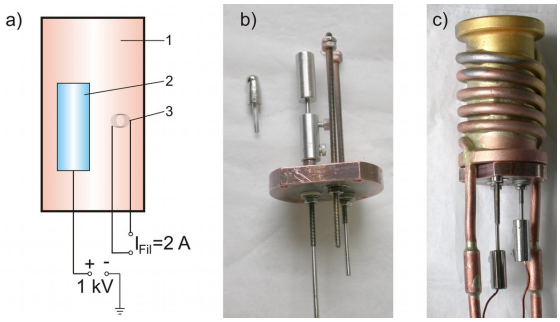

Figure 2.2 | Thermal evaporator. (a) Schematic illustration of evaporator with cooling shroud (1), evaporation rod (2) and heating filament (3). (b) Evaporation source with new evaporation rod mounted, used rod to the left. (c) Mounted and connected evaporator.

rotatable magnetic field generated by an *in-situ* vector magnet. Figure 2.3 shows the carrier plate that holds the magnet and the sample fixture in place. Due to geometrical restrictions of the vacuum chamber and the coil size, the generated field is limited to $H_{\max} \approx 100\,\mathrm{mT}$ ($H \approx 50\,\mathrm{mT}$ for continuous operation). The sample holder (Figure 2.3(c)) consists of a thin Cu plate with clamps and eight spring-loaded contacts. After nanopatterning (see Section 2.2), the sample is fixed and wire-bonded to the holder, which is then inserted upside down into the center of the vector magnet. This allows us to perform the characterization of the MR of the sample before, throughout and after the deposition process.

In order to reduce thermally induced instabilities in the nanocontact, the sample holder can be cooled down. For this purpose, the magnet carrier plate is mounted on the bottom end of a liquid nitrogen cryostat that keeps the sample at a temperature of about 80 K. The copper cylinder shown in Figure 2.3(a) establishes the thermal contact to the sample.

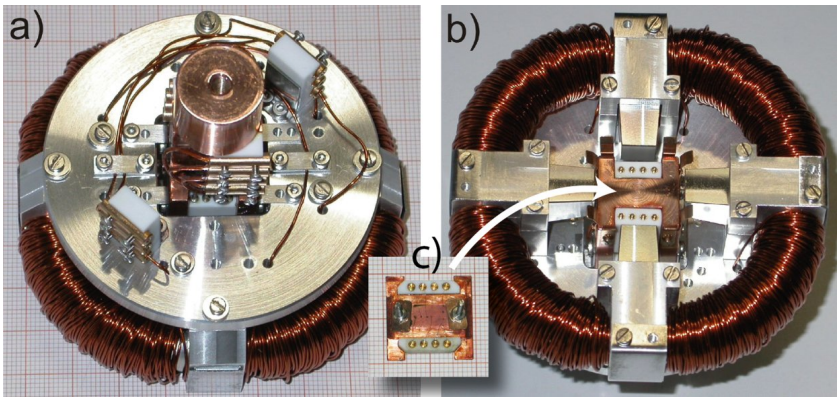

Figure 2.3 | Vector magnet and sample carrier for deposition and electrical measurements. (a) Top side with interface (Cu) to cryostat and electrical connections for magnet coils and sample contacts. (b) Side facing down (towards evaporators) with vector magnet and contacts for clip-in sample holder (c).

2.2 Sample fabrication

We developed two processes for the stable and artifact-free characterization of magnetic nanocontacts. Both are based on the same principle: First, the sample is pre-patterned using micro and nanofabrication techniques. Without prior deposition of magnetic material, the patterned sample is loaded into the UHV chamber and connected to the measurement equipment. Only then we deposit a clean layer of Permalloy to form a nanocontact on the substrate. As the contact is not exposed to the atmosphere between deposition and measurements (as often the case in previous experimental studies) we obtain exceptionally clean contacts.

The shape of the contact and its leads is determined in the pre-patterning step. For both processes we have chosen a magnetic half-ring geometry. In this geometry, DWs can be positioned precisely and reproducibly using a rotatable in-plane magnetic field H. Permalloy is frequently used for studies in magnetic nanostructures owing to its favorable magnetic properties. In particular its low crystalline anisotropy makes it often the best choice for generating geometry-controlled magnetization structures, such as DWs. We chose Permalloy not only for these reasons, but also because it exhibits very low magnetostriction: the relative length change at magnetization reversal, $\lambda = \Delta d/d$, amounts to less than $\sim 10^{-5}$ in Permalloy.

The detailed magnetization configurations of Permalloy ring nanostructures are well established by transport measurements and imaging techniques [42, 121, 122, 123] (see also Section 1.2). We have performed micromagnetic simulations to verify the controlled DW positioning in the half-ring structures used here. The magnetization configurations shown in Figure 2.4 illustrate the positioning by applying a saturating magnetic field along φ and relaxing it back to zero. We distinguish between three different magnetization states that can be generated: with a DW pinned at the notch, with a DW in one of the arms and without any DW within the half-ring. These results facilitate the interpretation of the MR data presented in Chapter 3.

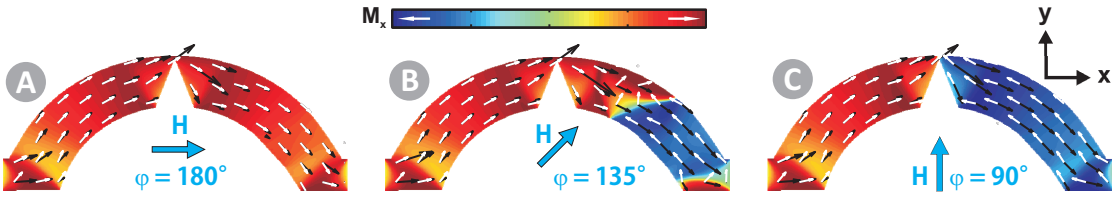

Figure 2.4 | Magnetization configurations of magnetic half-ring structures. Simulation of stable magnetization configurations (after saturating the magnetization at angle φ and relaxing the field to zero), (A) without DW, (B) with DW within the ring, (C) with a DW pinned at the notch. White arrows: magnetization orientation, Black arrows: local current direction and density.

Focused ion beam (FIB) lithography of suspended Si_3N_4 bridges

For the first fabrication process we use suspended Si_3N_4 bridges to obtain tailored nanocontacts. The most important fabrication steps are illustrated in Figure 2.5. First, Cr (5 nm)/Au (30 nm)/Cr (5 nm) pads are fabricated on Si_3N_4 (200 nm)/SiO_2 (500 nm)/Si substrates by a lift-off process based on electron beam lithography and electron beam evaporation. Using the top Cr layer as a mask, the samples are processed by reactive ion etching to remove the Si_3N_4 layer. After that, the samples are placed in a hydroflouric acid (HF) bath to remove the exposed SiO_2 layer. The resulting undercut of about $1-2\,\mu$m (see Figure 2.5(2)) completely underetches the Si_3N_4/Au bridges that connect the bonding pads.

After the HF etching step, a 60° ring segment with a constriction at its center is written by FIB. In a final processing step, the metallic layers (Cr/Au/Cr) are removed from the ring segment using FIB. This results in a free-standing Si_3N_4 bridge (see Figure 2.5(3)), on which Py can be deposited. In this state the sample is placed on and connected to the sample carrier. The carrier is then loaded into the UHV chamber with all contacts connected to ground and a layer of 12 nm Py is deposited at room temperature. The generation of the undercut is essential in avoiding any undesirable short circuit between the Py nanoring segment and the Py-covered resist layer. Without the undercut, the deposition of the Py layer would cover the sidewall of the Au/Si_3N_4/SiO_2 stack and thus short the entire sample to ground. The resulting samples are characterized by an outstanding mechanical stability as there is no free-standing part of the magnetic layer (the Py layer is supported by the 200 nm thick Si_3N_4 bridge).

Improved process: Shadow mask evaporation

The second process (see Figure 2.6) was developed as an alternative to the time-consuming and very sensitive FIB-based process described above. First, separated 5 nm Ti / 50 nm Au contact pads are fabricated *ex-situ* on a Si/SiO_2 substrate. Then, a double layer resist mask consisting of two resists of different sensitivity (PMMA and MMA) is defined by electron beam lithography. With the hard-baked resist on its surface, the sample is mounted on a chip carrier and the contact pads are electrically connected to the sample holder by wire bonding. After thorough outgassing, a 24 nm thick Permalloy film is deposited on the sample at a rate of

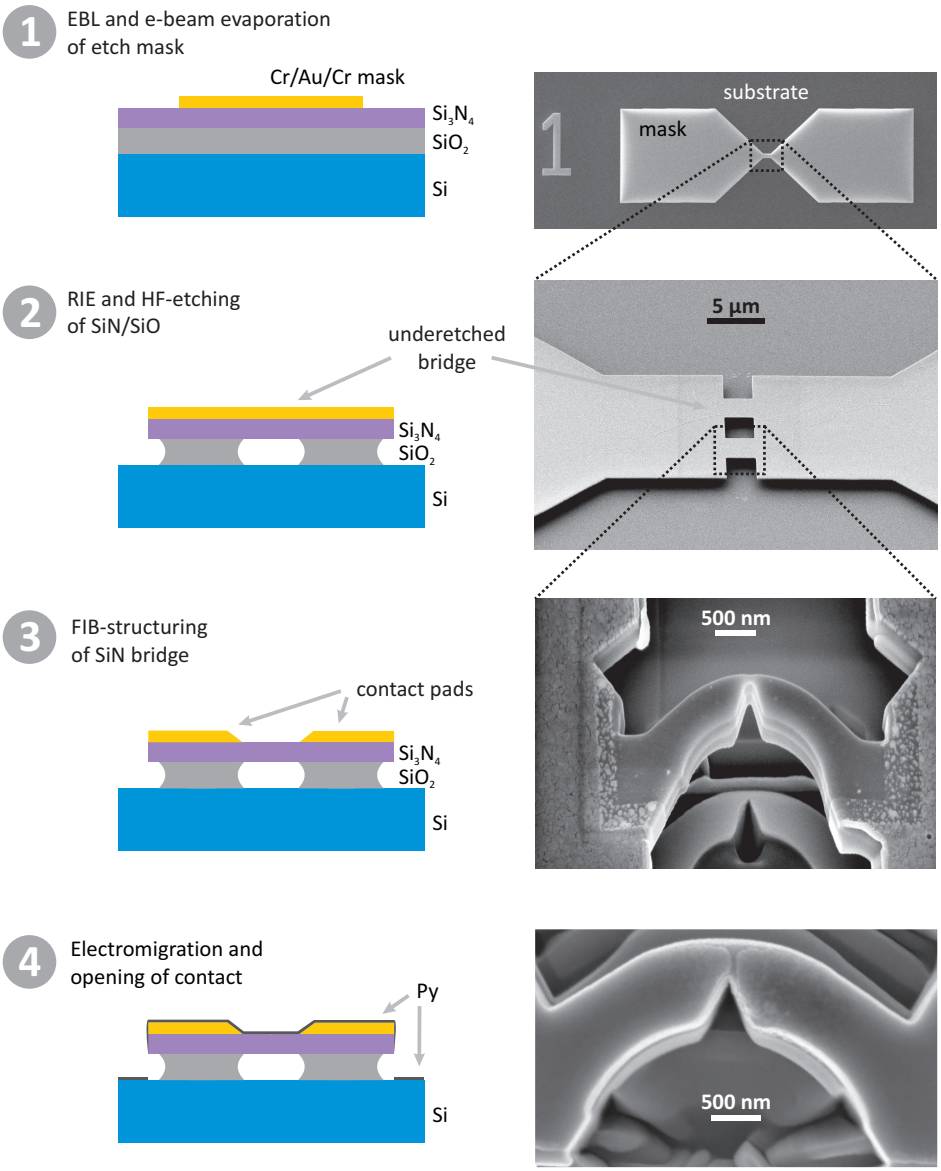

Figure 2.5 | Fabrication process I: suspended Si_3N_4-bridges tailored using FIB. Schematic illustrations (cross-sections) and corresponding scanning electron microscope (SEM) images. (1) Patterning of Au mask using electron beam lithography and e-beam evaporation (lift-off process). (2) Reactive ion etching of Si_3N_4 and subsequent isotropic wet (HF) etching of SiO_2 results in suspended Si_3N_4 bridges at the center. (3) Removal of Au layer and etching of notched ring section using high-resolution focused ion beam (FIB) lithography (SEM viewing angle $\alpha = 54°$). (4) Deposition of Py layer in UHV chamber establishes a contact across the Si_3N_4 bridge. The SEM image shows an opened Permalloy nanocontact obtained after several electromigration cycles. Process parameters and additional SEM images can be found in Appendix A.

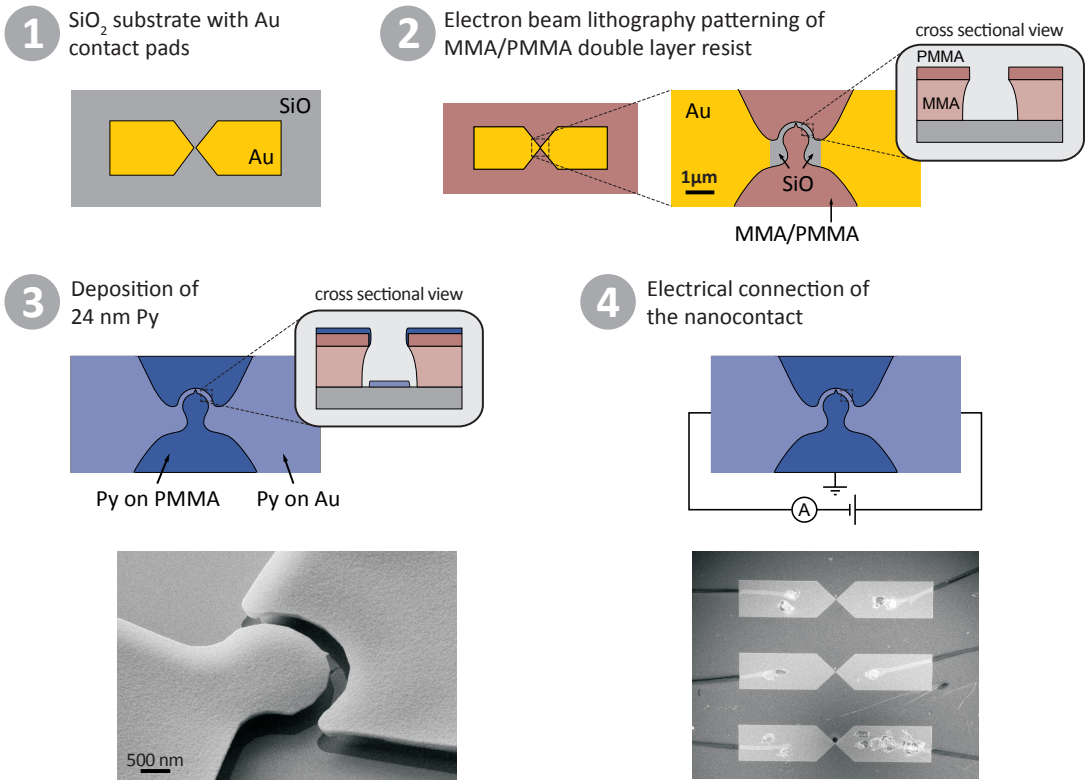

Figure 2.6 | Fabrication process II: Shadow mask evaporation. Schematic illustrations (top view and cross-sectional view) and corresponding scanning electron microscope (SEM) images. Process parameters and additional SEM images can be found in Appendix A.

$\sim 5\,\mathrm{nm\,h^{-1}}$. The resulting patterned film on the SiO_2 surface (see Figure 2.6(3)) establishes the electrical contact between the gold pads via the magnetic half-ring structure. Due to the large undercut along the edges of the resist, the contacted film is electrically isolated from the Py deposited on top of the resist, as can be seen in Figure 2.6(2-3). This is also confirmed by electrical measurements performed directly after the deposition of the Py film. Nanocontacts fabricated using this process offer an even better mechanical stability as the entire contact is rigidly attached directly to the substrate.

In-situ electromigration

To obtain nanocontacts of different cross-section, we carry out successive automated electromigration of the half-ring wire using the same electrical contacts used for MR measurements. A large current (~ mA, with the exact value depending on the state of the contact) is sent through the nanoring segment to induce electromigration (see Section 1.4). A computer-controlled process allows us to limit the temperature of the sample during electromigration such that local melting is prevented and the electromigration proceeds a in controlled fashion. The

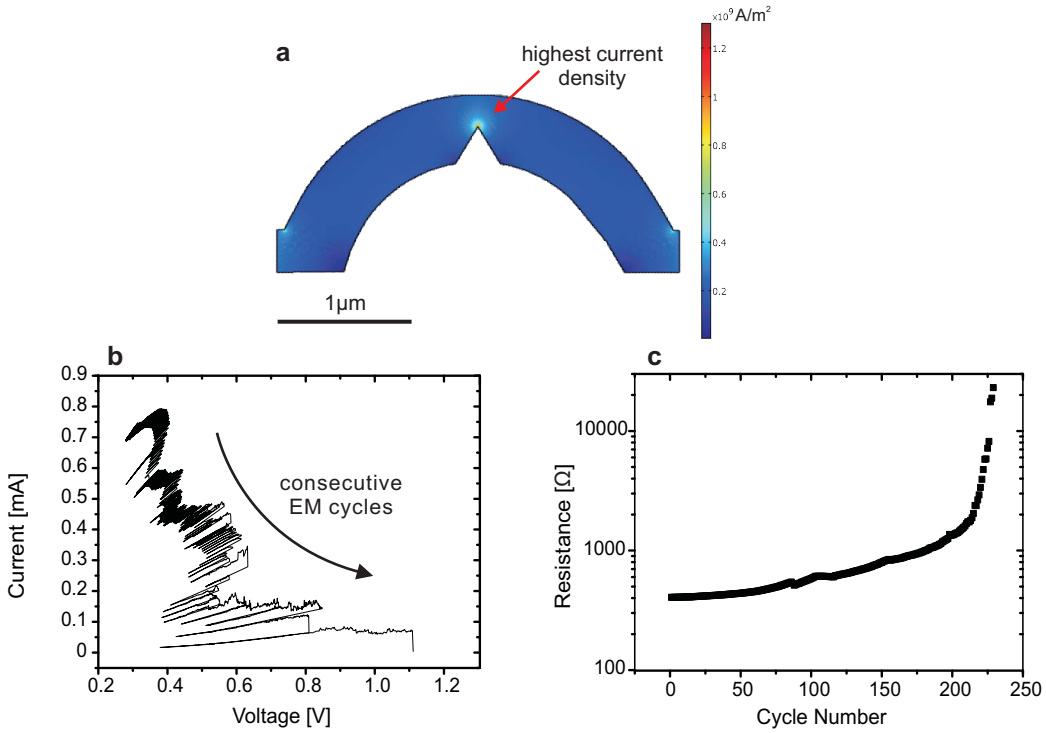

Figure 2.7 | Tailoring the constriction width by electromigration (EM). (a) Finite element method simulation of typical current density profile for a 500 nm wide and 20 nm thick nanoring segment (I = 1 µA). Current-voltage diagram (b) and contact resistance vs. EM cycles (c) for a typical EM process. Each line in (b) corresponds to one voltage ramp. A LabVIEW program dynamically adapts the termination condition with progressing EM (top left: virgin low-R contact, bottom right: high-R and breaking of contact).

constriction defines the position of the highest current density in the structure and it hence determines where electromigration sets in (see Figure 2.7(a) for a current density profile).

A typical measurement cycle consists of electromigration, where the constriction is thinned, followed by the in-situ characterization of the MR. As the constriction is thinned, it quickly starts to dominate the overall resistance. Hence, it is primarily the MR response of this area which is probed by the MR measurements. The electromigration is performed at a temperature of 80 K in order to reduce thermal noise and obtain mechanically stable contacts. The process is repeated until the contact is completely open, i.e. a gap has formed at the position of the constriction, resulting in an open circuit (Figure 2.7(b) and (c)). This procedure allows us to efficiently determine the evolution of the MR as a function of contact resistance.

2.3 Magnetoresistance measurements

Magnetoresistance measurements are carried out at 80 K in a two-probe configuration with an in-plane magnetic field H up to 100 mT. In order to avoid current-induced instabilities, the

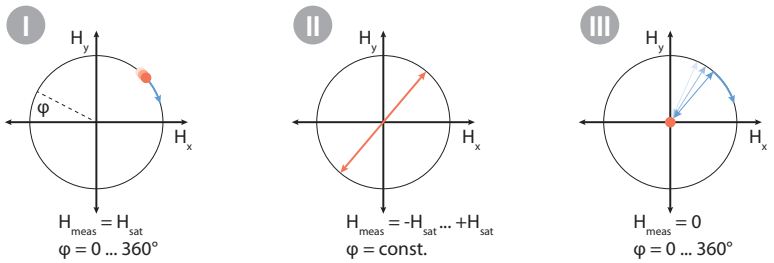

Figure 2.8 | In-situ MR measurement modes. Schematic illustrations of the applied magnetic fields for the three MR measurement modes (see text). The red dot and the red line indicate the field orientation and magnitude where resistance measurements take place.

measurement current is kept at least one order of magnitude below the critical current for electromigration (e.g. $I < 100\,\mu A$ for an as-grown contact). Three different types of measurements are employed to study the MR effects (see Figure 2.8):

I. **Angle sweep:** The resistance R of the contact is measured as a function of the angle φ of the applied field while keeping the magnitude of the applied field constant. This measurement can be used to determine the AMR.

II. **Field sweep:** The resistance is measured as a function of the field magnitude for a given field angle φ. This measurement is commonly called 'R(H)-loop'.

III. **Star mode:** The resistance is measured as a function of the field angle φ at remanence, i.e. after applying a magnetic field along φ and reducing the field to zero. This measurement mode enables the characterization of stable magnetic states at remanence in the absence of any applied field. As this helps reducing artifacts due to field-induced magnetostriction, some of our key measurements are based on this mode. For further details, see the quasi-static measurement scheme described in References [124, 42]).

In the following, the MR ratio is defined as $(R_{AP} - R_P)/R_P$, where $R_{P/AP}$ denotes the resistance of the nanocontact with both arms of the half-ring oriented in a parallel (P state, no DW) and anti-parallel (AP state, DW at the constriction) configuration, respectively.

3 Results and discussion

We perform two complementary studies on MR phenomena in Py nanocontacts. First, using fabrication technique I we focus on the evolution of the MR in the diffusive regime up to a contact resistance of about 500 Ω. In this study our primary goal is to shed light on the role of intrinsic DWMR in diffusive nanocontacts using our novel experimental approach. For the second study we employ fabrication technique II to explore DW-induced MR effects in the ballistic conduction regime in atomic nanocontacts.

3.1 Magnetoresistance in the diffusive regime

Freestanding Si_3N_4 bridges with a 12 nm thick Py film are prepared according to the FIB-based patterning procedure described in Chapter 2. The geometry and orientation of the ring segment is depicted in Figure 3.1(a). Before starting the electromigration the structure has a constriction width of 220 nm (≈ half of the ring width) and a base resistance (including leads) of 250 Ω. Constriction widths ranging from 220 nm to a few nanometers are obtained in a single nanocontact by successive electromigration. Figure 3.1(a) shows a successfully characterized nanoring with an open gap, indicating that localized and controlled electromigration at the

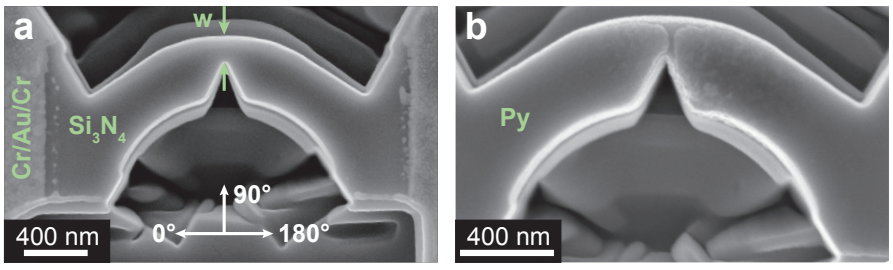

Figure 3.1 | Sample geometry for MR measurements in the diffusive regime (a) SEM image of the freestanding nanoring segment before deposition of Py. w denotes the constriction width defined by the shape of the bridge. White arrows indicate the orientation of the field angle φ. (b) SEM image of an opened Permalloy nanocontact obtained after a large number of electromigration cycles.

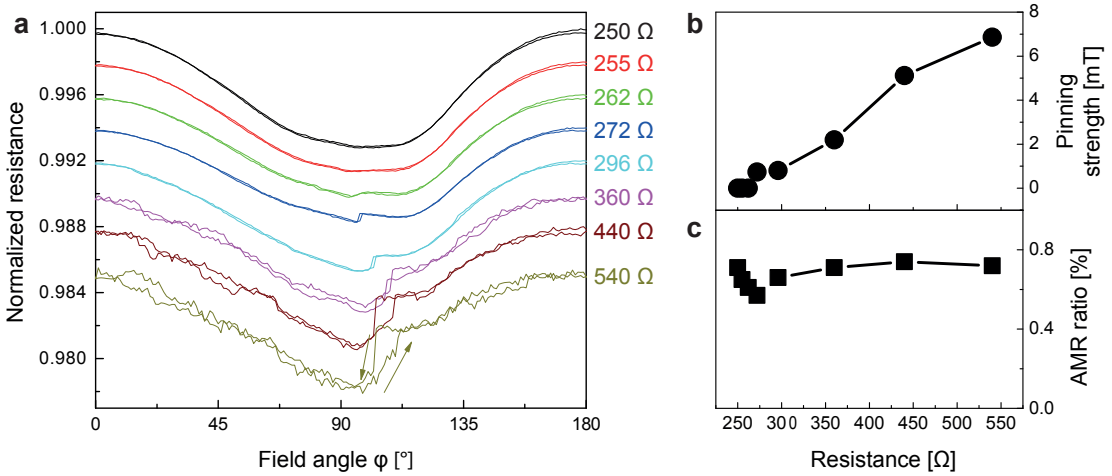

Figure 3.2 | Angle sweep MR measurements and analysis of magnetization pinning. (a) Angular variation of the magnetoresistance curves for different resistance values, obtained by progressive electromigration of the nanocontact, measured at 80 K with a 42 mT in-plane field. The curves are offset along the y-axis for clarity. (b) Pinning strength and (c) AMR ratio (extracted from the MR curves shown in (a)) as a function of the measured resistance.

position of the constriction has taken place.

For each resistance state (i.e. electromigration cycle), we first study the AMR of the nanocontact using an angle sweep measurement (see Section 2.3) at $\mu_0 H = 42\,\mathrm{mT}$ (see Figure 3.2(a)). The direction φ along which the magnetic field is applied is indicated in Figure 3.1(a). Before electromigration ($R = 250\,\Omega$), the normalized resistance as a function of φ shows the typical $\cos^2\theta$ behavior well-known from AMR in bulk samples (see Section 1.5.1). This confirms that the applied magnetic field is sufficiently strong to completely align the magnetization of the half-ring structure.

Unlike in the bulk, the angle θ between current and local magnetization varies across the ring segment: On the one hand, the current flow is static and has to follow the ring structure (see Figure 2.4). This means that, instead of flowing homogeneously along $\varphi = 0°$, there will be a slight deviation towards positive angles in the right arm and towards negative angles in the left arm. On the other hand, the magnetization of the sample is aligned nearly homogeneously along the applied field direction φ. Therefore, the mutual orientation of magnetization and current is never completely (anti-)parallel (maximum resistance) or perpendicular (minimum resistance). Consequently, we expect a small reduction of the AMR amplitude in comparison with an unpatterned thin film.

As expected, the measured resistance is larger for a magnetic field applied along $\varphi = 180°$ (or 0°), where the magnetization of most of the ring segment is roughly aligned parallel (or antiparallel) to the current direction. The resistance is lower for $\varphi = 90°$, for which magnetization and current are mostly perpendicular to each other. Already at the base resistance, the angle-dependence of the MR shows small deviations from the expected $\cos^2\theta$ behavior. We

ascribe this to imperfections (i.e. asymmetries) of the nanostructure geometry.

A similar functional dependence of the resistance on the field angle is observed for all successive electromigration states and their corresponding constriction widths (Figure 3.2(a)). For nanocontact resistances of $R_N \geq 272\,\Omega$ additional features appear. Reproducible hysteretic resistance jumps close to the angle corresponding to the constriction location (90°) are observed. These jumps and the hysteresis are indications of the pinning and depinning of the magnetization structure at the constriction. For smaller constriction widths, larger jumps and a more pronounced hysteresis are observed. From the hysteresis we can estimate the pinning strength of the constriction for a given resistance. The pinning strength is evaluated as $H \sin \Delta\varphi$ with $\mu_0 H = 42\,\mathrm{mT}$, where $\Delta\varphi$ is taken from the hysteresis of the MR curves (Figure 3.2(a)). The deduced pinning strength as a function of the sample resistance is depicted in Figure 3.2(b). As expected, we obtain stronger pinning when the constriction is narrowed down by electromigration and the contact resistance R_N rises. In this series of measurements, the effective depinning field reaches a value of about 7 mT for $R_N = 540\,\Omega$.

Moreover, we can extract the AMR ratio $[\{(R_{\mathrm{max}} - R_{\mathrm{min}})/R_{\mathrm{max}}\} \times 100]$ from the MR curves shown in Figure 3.2(a). As shown in Figure 3.2(c), the value stays approximately constant for the whole resistance range investigated. In addition, the maximum AMR ratio is just below 1 %, which is in agreement with reports on Py (References [100] and [119]) for constriction widths down to a few nanometers. In summary, the behavior obtained from angle sweep measurements suggests that the observed MR can be ascribed to bulk AMR.

Next, for the same contact resistance, we measure the resistance values for a DW located at various positions, in particular, at the constriction position as well as next to the constriction. For this we employed the 'star mode' measurement (see Section 2.3), where we saturate the sample along a certain direction φ (with $\mu_0 H_{\mathrm{sat}} = 42\,\mathrm{mT}$) and relax the field to zero to position the domain wall. At remanence the shape anisotropy of the narrow ring leads to three different situations as sketched in Figure 3.3(c):

(I) A domain wall can be situated *at the constriction*. This configuration is obtained for $\varphi \approx 90°$, meaning that the field points in the direction of the constriction position or along angles close to this direction. In this situation, the magnetization in the two arms follows the perimeter and is aligned in opposite directions, forming a domain wall at the constriction. As shown in Figure 3.4(b) and (c), micromagnetic simulations of the used contact geometry confirm the existence of this state. (II) A domain wall can be located *in the ring but outside the constriction*, and state (III) denotes the absence of domain walls in the ring. Configuration (III) is expected for fields applied at angles larger than 120° and smaller than 60°, where the magnetization configuration is determined by the perimeter of the ring.

Figure 3.3(a) shows the normalized resistance measured at remanence as a function of the field angle for two different overall nanocontact states ($R_{\mathrm{N}} = 272\,\Omega$ and $440\,\Omega$ as examples) established after different electromigration cycles. As expected, three different resistance levels are observed for both resistance values within the anticipated range of angles. The

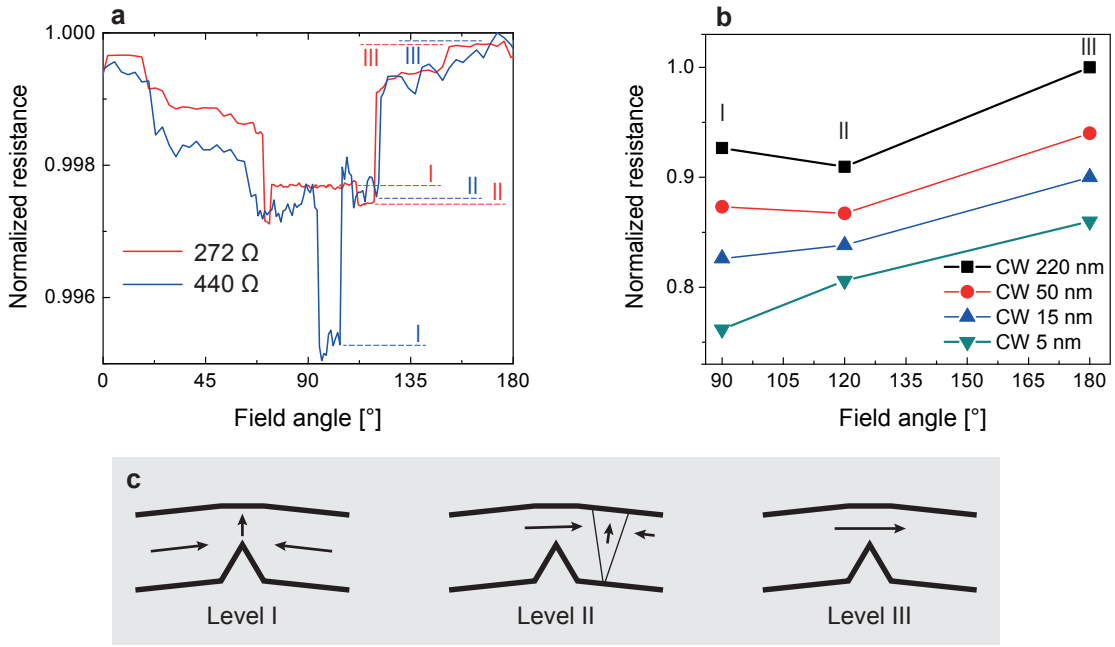

Figure 3.3 | Star mode MR measurements and comparison with simulation results. (a) Measured MR curves at remanence as a function of field angle φ for two selected resistance values. An in-plane field of 42 mT is applied at angle φ and then relaxed to zero before carrying out the resistance measurement. The constriction position corresponds to $\varphi \approx 90°$ (see Figure 3.1(a)). (b) Simulated MR values for different constriction widths. Lines in (b) are a guide to the eyes. (c) Schematic spin configurations of the constriction region. I, II and III denote three different resistance levels and correspond to the case of a domain wall at the constriction, a domain wall in the ring (but away from the constriction) and the absence of a domain wall.

appearance of these levels can be understood in terms of AMR when taking into account the magnetization configuration of the three scenarios discussed above. The current density profile is assumed to be static, always following the perimeter of the ring and reaching its highest value at the constriction (see Figure 3.4(a)). The resistance at $\varphi > 120°$ or $\varphi < 60°$ (level III) is largest, because in this situation current and magnetization are parallel to each other across the ring segment (AMR $\propto \cos^2\theta$ and $\theta = 0°$). Scenario I and II exhibit a domain wall. The magnetization direction inside the wall has a perpendicular component to the current direction ($\theta = 90°$). Therefore, again due to the AMR, the resistance of the nanocontact with a domain wall is lower compared to the situation without a wall.

Surprisingly, we observe a sign change from positive to negative in the MR difference $\Delta R_{(\mathrm{I-II})}$ between level I and level II when narrowing down the constriction. This suggests that the constriction width and thus the domain wall size plays a key role in the MR properties of the nanocontact. Given the large variety of results from previous studies on DWMR (see Section 1.5), such a contact size-dependence of the resistance can tempt one to attribute this behavior to positive or negative intrinsic DWMR. However, we will demonstrate in the following that the behavior can be understood using a model entirely based on AMR.

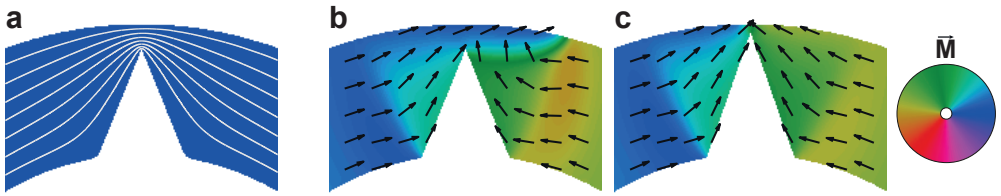

Figure 3.4 | Simulation of current density and magnetization configurations. (a) Current density profile for a constriction width of 90 nm. (b-c) Magnetization configuration for the case of a domain wall near the constriction (Level I in Figure 3.3) for (b) 90 nm and (c) 30 nm constriction width. The magnetization direction is indicated by the color disk to the right.

In general, the AMR is proportional to $\cos^2\theta$. This implies that the absolute resistance values of level I and II depend particularly on the magnitude of the current density j at the position of the domain wall and on the width of the domain wall. The influence of these two factors can be considered separately: As discussed previously, the geometry of the constriction leads to a smaller domain wall width for the wall residing in the constriction compared to the wall located in one of the half-ring segments. The area where the resistivity is lowered due to AMR is therefore much smaller when the wall is pinned at the constriction. Considering this factor alone, one would expect an increase in resistance for scenario I. However, when taking into account the current density, the situation reverses: a narrow constriction exhibits a higher current density than the rest of the ring. Hence, its contribution to the overall resistance (and AMR) is larger. In this case, the change in AMR due to a DW pinned at the constriction (scenario I) can lead to a decrease of the overall resistance.

The interplay of these two effects leads to the following observation: For a wide constriction, i.e. when differences in $\boldsymbol{j}$ across the ring segment are small, the resistance level I (domain wall at the constriction) is higher compared to level II (domain wall next to the constriction) and hence $\Delta R_{(\mathrm{I-II})}$ is positive. This behavior is indeed observed for $R_N = 272\,\Omega$ (red curve in Figure 3.3(a)). For narrow constriction widths, the current density at the constriction grows and resistance level I can be lower than level II. In fact, we do observe such behavior for $R_N = 440\,\Omega$ (see Figure 3.3(a) blue curve) where the constriction is only a few nanometers wide (see discussion of contact size based on Wexler's formula further below).

To verify this interpretation also quantitatively, we numerically compute $\Delta R_{(\mathrm{I-II})}$ as a function of field angle and constriction width by assuming a purely AMR-based magnetoresistance. We use the LLG micromagnetic simulator and COMSOL Multiphysics to determine the magnetization configuration and the current density profile, respectively. The simulation geometry is adapted from the initial geometry (before electromigration) shown in Figure 3.1(a), with the constriction width ranging from the initial value of 220 nm down to 1 nm. For the micromagnetic solver we use the following simulation parameters: saturation magnetization $M_s = 800 \times 10^3\,\mathrm{A\,m^{-1}}$, exchange stiffness $A = 10.5 \times 10^{-12}\,\mathrm{J\,m^{-1}}$, crystalline anisotropy $K_1 = 1 \times 10^2\,\mathrm{J\,m^{-3}}$, film thickness 12 nm and cell size 5 nm. To reduce the computation time we use a damping parameter of $\alpha = 1$, which leads to the same final spin configuration as a

small (realistically, $\alpha \approx 0.01$) damping parameter. In the case of constriction widths of less than 5 nm, the center cell at the constriction is replaced by a smaller (down to 1 nm) cell size. For this purpose, both, the magnetization structure and the current profile were taken from the result with 5 nm cell size and scaled down appropriately. A variable cell size approach was used for the current density simulations as well. A simulated current density profile for a constriction width of 90 nm and the magnetization configuration for the case of a domain wall near the constriction for two different constrictions widths (90 nm and 30 nm) are shown in Figure 3.4.

For each cell of the simulation mesh we calculate the AMR according to Equation (1.14). To account for the varying current density, we use a correction factor of $1/d$, where d is the width of the ring at the position of a given cell. The limiting resistivity values $\rho_{\parallel}$ and $\rho_{\perp}$ in Equation (1.14) are deduced by comparing the simulation result for these limiting cases to the maximum and minimum of the measured resistance. Adding up the AMR values of all cells yields the total AMR as a function of magnetization configuration.

We additionally take into account possible changes in the effective resistivity at the constriction due to the onset of the ballistic conduction regime in small contacts. For a given constriction width, the corresponding resistance is calculated using Wexler's formula (Equation (1.12)), which describes the transition from diffusive to ballistic conduction. We use a mean free path of $l = 1\,\text{nm}$ [44] and a resistivity of $\rho = 40\,\mu\Omega\,\text{cm}$ [125]. Then, from the calculated resistance we estimate an effective resistivity that also includes ballistic contributions for contacts approaching atomic dimensions. As expected, an increase in the effective resistivity with decreasing constriction width is observed. The effective resistivity for 1 nm constriction width is more than twice the original resistivity. Based on this result, we performed additional simulations with a smaller cell size and a locally varying effective resistivity. An influence was observed for the smallest constriction sizes. However the deviation is too small (below 2 %) to have a significant impact on the result of the simulations.

The normalized resistance values obtained from the simulation are shown in Figure 3.3(b). Similar to the experiment, we obtain three different resistance levels as a function of field angle. In agreement with the discussion above, the presence of a domain wall in the nanoring reduces the resistance (Figure 3.3(b): level I/II with DW and level III without DW). Moreover, the simulation results reproduce the experimentally observed sign change of $\Delta R_{(\text{I}-\text{II})}$ for smaller constriction widths (15 and 5 nm in Figure 3.3(b)).

For a more detailed verification of this agreement we normalize the experimentally obtained $\Delta R_{(\text{I}-\text{II})}$ with respect to the maximum AMR for the corresponding resistance value. Figure 3.5(a) shows the result plotted as a function of contact resistance for the experimental data. As discussed previously, $\Delta R_{(\text{I}-\text{II})}$ changes its sign from positive to negative when the nanocontact resistance increases beyond 340 Ω. Moreover, its magnitude grows with increasing resistance, i.e., for smaller constriction widths. The same trend can be identified in the data derived from the simulations, as shown in Figure 3.5(b) (filled circles). For this graph $\Delta R_{(\text{I}-\text{II})}$ is normalized

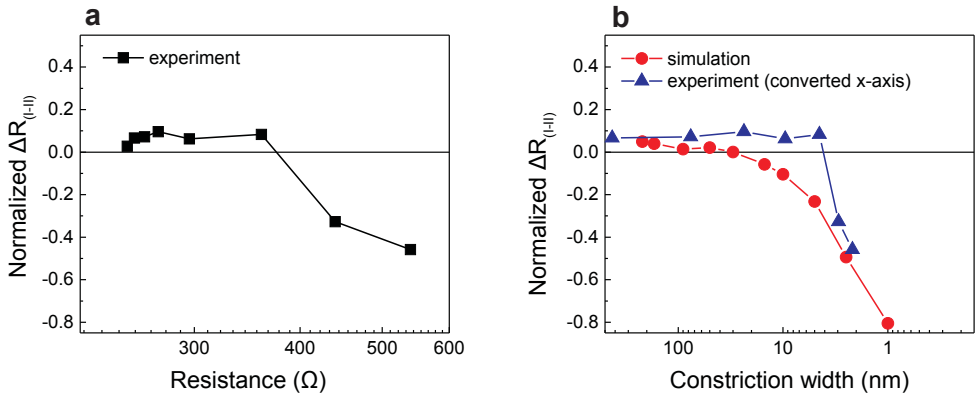

Figure 3.5 | Comparison of simulated and measured AMR for different constriction widths. (a) Measured resistance difference between level I (domain wall at the constriction) and level II (domain wall in the ring segment) normalized by the AMR ($(R_{max} - R_{min})/R_{max}$ measured at 42 mT) as a function of nanocontact resistance. (b) Comparison of simulated (circles) and measured (triangles) $\Delta R_{(I-II)}$ for different constriction widths (see text for details on the conversion from contact resistance to constriction width).

with respect to the maximum of the simulated AMR for a particular constriction width.

Next, we directly compare the measured with the simulated data. For this purpose, the experimentally measured resistance of the nanocontact is converted to a corresponding constriction width using Wexler's formula (Equation (1.12)) (with the same parameters as given above). Strictly speaking, the formula is only valid for circular cross-sections (thickness = diameter = constriction width). Therefore, deviations from this shape have to be taken into account. For large contact sizes the cross-section of our contacts is much better described by a rectangular conductor of size constriction width × film thickness. The first electromigration cycles will then narrow down mainly the width while keeping the thickness constant (the formation of a trench between the contact leads has been consistently observed and can also be seen in Figure 3.1). For contact sizes below the thickness of the Py film (12 nm) we assume a circular cross-section. As Wexler's formula does not describe the resistance of the leads, we also include a base resistance of 250 Ω. The converted experimental data points are depicted in Figure 3.5(b) (filled triangles) together with the simulated data (filled circles).

As one can see in Figure 3.5(b), the experimentally determined behavior of $\Delta R_{(I-II)}$ agrees qualitatively with the one obtained from simulation. We attribute the lack of quantitative agreement, especially regarding the position of the sign change, to the following reasons: First, as discussed previously, Wexler's formula is derived from a simplified model for ideal contact geometries with a circular contact cross-section. The corrections introduced above might not fully compensate for the geometrical deviation from this ideal shape. Thus, the conversion from resistance to constriction width might introduce a significant error in the x-axis position. Second, the discrepancy could arise from differences between the simulated and the real magnetization structure, particularly for small constriction widths. Locally changing surface morphology or magnetocrystalline anisotropy as well as residual surface contamination are

not taken into account but could considerably change the micromagnetic behavior. Additionally, we neglected any changes in the magnitude of the AMR. Despite the fact that such changes have only been observed and predicted for atomic contacts (see Section 1.5), we cannot completely exclude their occurrence for the smallest contacts investigated here ($d \approx 1\,\mathrm{nm}$). It should also be noted that additional weak responses from other intrinsic effects such as the domain wall magnetoresistance (DWMR) cannot be entirely ruled out either. According to most predictions, the DWMR should lead to a rapidly growing positive contribution to $\Delta R_{(\mathrm{I-II})}$ for small constrictions ($\propto 1/w^2$). However, our experimental data indicates the opposite trend (see Figure 3.5) without any signature of DWMR. If there is such an effect, it must be significantly smaller than the observed AMR effect.

In summary, although the simulated MR values based on the bulk AMR effect do not agree quantitatively with our measurement data, we find convincing qualitative agreement. It is particularly striking that the sign change in $\Delta R_{(\mathrm{I-II})}$ can be reproduced considering pure AMR as the source of the MR. We therefore conclude that AMR is the dominant contribution to the MR signal of these electromigrated Permalloy nanocontacts down to a size of a few nanometers.

3.2 Magnetoresistance in the ballistic regime

In a second study we employed the shadow mask evaporation technique presented in Section 2.2 to extend our analysis of DW-induced MR phenomena to the ballistic regime. Figure 3.6(a) shows an SEM image of the fabricated ring segment before electromigration, along with a description of the resist structure (b) and the magnetic field orientation with respect to the sample (c).

Before the initial electromigration step, all of the nominally identical samples exhibit a resistance of $275\,\Omega$ [Figure 3.7(a)]. For such low resistance values, the MR is dominated by AMR with a magnitude of approximately 1 %. Up to a contact resistance of $R \approx 1\,\mathrm{k}\Omega$ the AMR gradually increases as the constriction is slowly narrowed by electromigration (see inset in Figure 3.7(a)). This rise is due to the growing contribution of the constriction resistance to the total resistance, making other contributions such as that of the (in this sample largely non-magnetic) leads and the Permalloy film outside of the ring section negligible. In line with our previous results, we do not observe any sign of measurable intrinsic domain wall magnetoresistance in this low resistance regime, but only AMR.

Next we turn to the ballistic conduction regime above about $5\,\mathrm{k}\Omega$, where novel MR effects are expected to occur. As the diameter of the magnetic nanocontact approaches atomic dimensions, thermal and electromigration effects can lead to significant rearrangements on the atomic scale, changing the total resistance of the contact. In contrast to the low resistance regime, now the resistance changes during electromigration occur as distinct steps between stable levels, indicating that well-defined atomic reconfigurations take place at the narrowest part of the contact [65]. The MR changes significantly in this atomic contact regime: Its

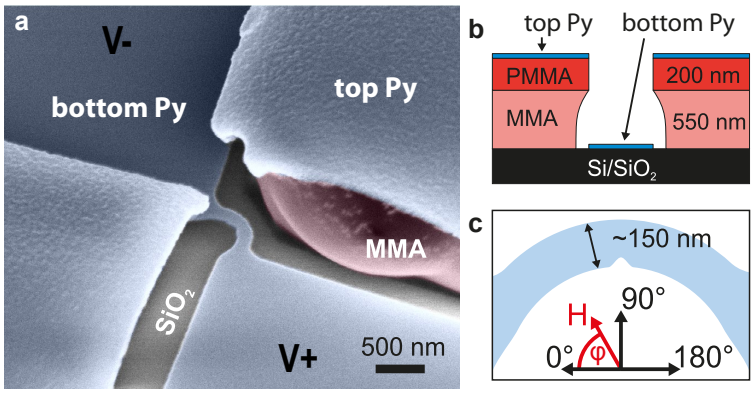

Figure 3.6 | Sample geometry for MR measurements in the in the ballistic regime. (a) Scanning electron microscope (SEM) image (viewing angle 45°) showing the constricted ring section before electromigration (blue: Permalloy, red: resist, gray: SiO_2 substrate). The deformation of the MMA/PMMA resist is due to the electron beam of the used SEM. (b) Schematic illustrations of the cross-sectional view of the sample and (c) the top view of the ring section indicating the orientation of the in-plane magnetic field H.

magnitude increases drastically to more than 50 % (Figure 3.7(a)) and we observe positive and negative MR. This large MR effect completely supersedes the small AMR [120] and dominates the overall MR.

In agreement with our previous findings for the diffusive regime, also in the ballistic regime we observe different resistance levels with and without a DW pinned at the constriction. The switching between these states is shown in the R(H) loop in Figure 3.7(b): when applying a field of +100 mT approximately along the direction of the constriction ($70° < \varphi < 110°$) the magnetization in the arms is aligned along φ. After removing the field, the spin orientation is determined by the shape anisotropy of the narrow structure, causing the spins to align parallel to the edge. A head-to-head DW is formed at the constriction, associated with a resistance value of the nanocontact of $R_{AP} \sim 19\,k\Omega$. When the field is reversed, the magnetization configuration changes to a quasi-single domain state without a DW ($R_P \sim 25\,k\Omega$) [42]. At higher reversed field, a new DW is nucleated. The corresponding spin structures for each of the resistance levels are schematically illustrated in the same figure.

The existence of a distinct MR effect in addition to AMR is verified by the measurement of the resistance as a function of applied field angle (measurement type (I)), as shown in Figure 3.8. The data for the two low-resistance contact states ($R \approx 272\,\Omega$ and $728\,\Omega$) confirm the previously discussed deviation from the $\cos^2\theta$ AMR behavior due to strong shape anisotropy in the contact region (see Figure 3.2). While we still observe AMR of the same order of magnitude as in the low resistance regime (about 1 % with the same angle-dependence), an additional MR contribution starts appearing in the ballistic conduction regime ($R \approx 9.7\,k\Omega$, blue curve in Figure 3.8). At even higher resistance levels this signal dominates the overall MR response, by far exceeding the observed bulk AMR signature. Here, the change in resistance occurs at the same field angles as the hysteretic jumps in the AMR signal in the diffusive regime (green

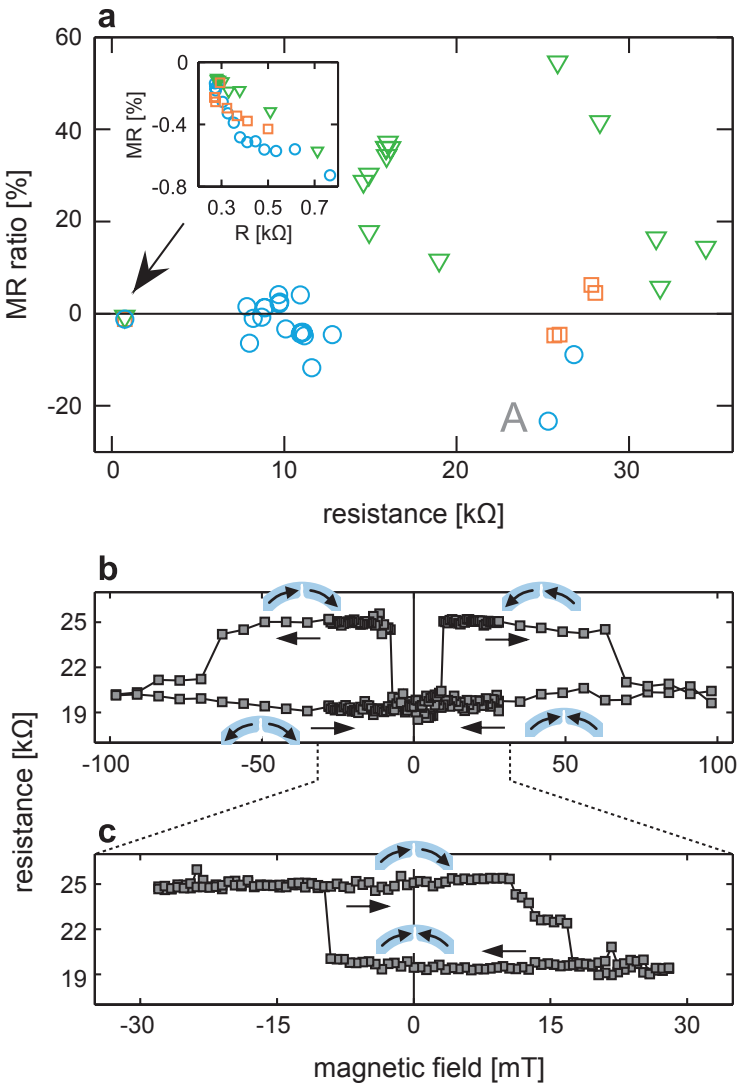

Figure 3.7 | MR response and magnetic switching behavior in the ballistic regime. (a) Magnetoresistance ratio MR = $(R_{AP} - R_P)/R_P$ vs. contact resistance in the parallel state (R_P) for three nanocontacts (blue, green and red). The data points are acquired from R(H) loops with $\mu_0 H_{max} = 100\,mT$ and $\varphi = 75°$ and 90°. Inset: evolution of AMR for low contact resistances at the beginning of the electromigration process. Resistance vs. magnetic field (b) major and (c) minor loop at field angle $\varphi = 75°$ for the contact state labeled 'A' in Figure 3.7(a). Sketches illustrate the magnetization configuration of the contact leads for different positions in the loop. The black arrows along the curve indicate the sweep direction.

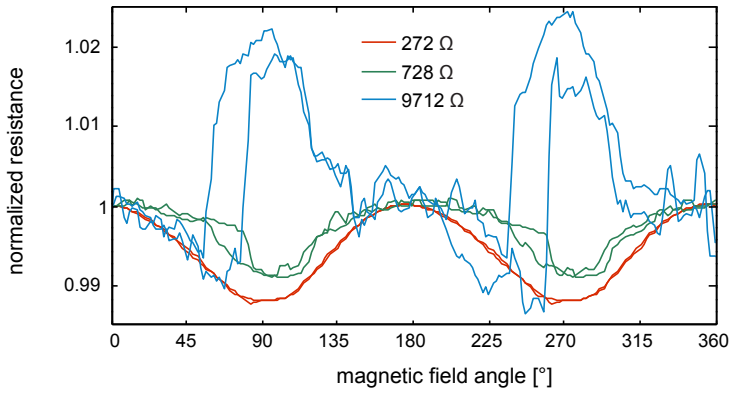

Figure 3.8 | Separation of AMR and DW-induced MR using angle sweeps. Normalized resistance as a function of applied magnetic field angle φ for three different resistance states of the same contact at a constant field amplitude of 50 mT.

curve), suggesting that the behavior of the magnetization largely remains the same. However, at the same time, the MR signal is of much larger magnitude than the AMR (about 2.5 %) and exhibits the opposite sign. AMR, including the larger AMR on the atomic scale, has never been shown to exhibit such a large change in the amplitude and sign (see for example studies by M. Viret). Supported by the fact that we still see the small AMR contribution, this allows us to distinguish between the contributing MR effects (AMR, DWMR) even without completely saturating the magnetization of the sample.

Importantly, also the switching fields in the R(H) loops do not change significantly during the thinning of the nanocontact, confirming that the magnetic states are fundamentally identical in both conduction regimes. As depinning fields usually depend strongly on the geometry and size of the constriction, a constant switching field indicates that the transition from the state with a DW to the one without does not occur by depinning of the wall. Instead, a reverse domain nucleates at one of the two ends of the half ring, which then annihilates the DW at the constriction. In contrast to previous studies (e.g. References [119, 115, 120, 114]), here the magnetization of the arms can be switched in low fields, independently of the precise geometry of the constriction. Hence, we can uniquely identify the presence of stable DW and the resulting impact on the MR even at zero field, as depicted in Figure 3.7(c).

In addition, one has to consider that in our head-to-head domain wall geometry the largest gradient of the magnetization M, i.e. the position of the domain wall center, tends to be located at the narrowest point of the nanocontact to minimize the exchange energy. This is an advantage over other geometries used (e.g. the one in Reference [119]), in which the magnetization points perpendicularly to the channel formed by the nanoconstriction. In such cases, the areas with the strongest magnetization gradients often form outside the narrowest part of the constriction (in particular as the magnetization aligns with the channel geometry due to shape anisotropy), making a reliable characterization of the DW-induced

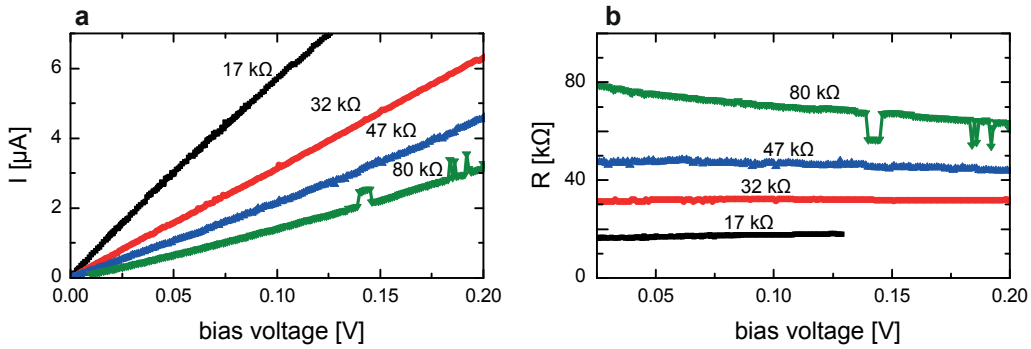

Figure 3.9 | I-V characteristics at high contact resistances. $I(V)$ (a) and $R(V)$ (b) diagrams for three different resistance states of the same contact, illustrating the transition from the ballistic ($dR/dV = 0$ or > 0 due to Joule heating at lower resistance values) to the tunneling regime ($dR/dV \leq 0$).

MR challenging. These observations further confirm that, despite the growing influence by pinning at the atomic level in nanocontacts, the two distinct resistance levels observed in R(H) loops in the high resistance regime (see Figure 3.7(c)) correspond in fact to levels with and without a DW pinned at the constriction. Moreover, this validates the schematic spin structures shown in Figure 3.7(b,c).

As discussed in Section 1.5, magnetostriction artifacts can lead to arbitrarily high MR values. Our nanocontacts are rigidly attached to the substrate and should therefore be mostly magnetostriction-free. Only a small part of the contact might become suspended during electromigration. A recent study on high-resolution AFM imaging of electromigrated nanocontacts [57] indicates that the grains establishing the nanocontact are still attached to the substrate. We therefore assume that the length of the suspended part is less than 10 nm. As Permalloy exhibits very low magnetostriction ($\lambda_{\mathrm{Ni}} < 10^{-5}$), the maximum displacement due to magnetostriction must be less than 0.1 pm. Similar assumptions were made by Bolotin et al. [119] to exclude artifacts in the tunneling regime. Such tiny displacements are not expected to lead to significant resistance changes in the ballistic regime either (see for instance Fig. 3(d) in Reference [126]). Even if we assume a (unrealistically large) relative change of the contact length of 1 %, according to Ref. [126], one would obtain only a few percent magnetostriction-induced MR, much less than what we observe.

A second potential artifact in the presented measurements is tunneling transport, which is known to give rise to large MR ratios (TMR effect, see Section 1.1). It is therefore crucial to analyze the tunneling contribution to the conductance and to separate ballistic transport from tunneling transport. The transition between the two regimes proceeds gradually, moving from electron transport between neighboring atoms via overlapping orbitals to transport across a small gap via rapidly decaying electron wave functions. Obviously, for a (predominantly) ballistic contact, there will be some tunneling conduction in parallel. Hence, the important issue is to determine the dominant transport mechanism. For this purpose, we analyze the I-V characteristics and the corresponding $R(V)$ curves of a series of different contact states

ranging from 17 kΩ to 80 kΩ (see Figure 3.9). A linear behavior of $I(V)$ usually indicates ballistic transport (or diffusive, which can be excluded in this case). Dominating tunneling transport is usually characterized by a strong non-linear behavior of $I(V)$ [119] (i.e. decreasing $R(V)$). The two states in the important resistance range with $R = 17\,\mathrm{k\Omega}$ and $32\,\mathrm{k\Omega}$ show linear $I(V)$ curves, suggesting that these contact states are predominantly ballistic. The slightly positive slope of $R(V)$ for $R = 17\,\mathrm{k\Omega}$, and to a smaller extent for $R = 32\,\mathrm{k\Omega}$, can be attributed to Joule heating in the vicinity of the contact, which is often observed for lower resistances. Its influence, however, is reduced with increasing R, going from the diffusive to the ballistic regime. At higher resistances, i.e. $R = 47\,\mathrm{k\Omega}$ and $R = 80\,\mathrm{k\Omega}$, the $I(V)$ curve becomes increasingly non-linear, with $dR/dV < 0$, indicating that the onset of tunneling transport occurs significantly above $32\,\mathrm{k\Omega}$. As the reported large DW-induced MR is mainly observed in a range from $10\,\mathrm{k\Omega}$ to $30\,\mathrm{k\Omega}$, we can conclude that the MR effects occur indeed in the ballistic conduction regime and that a significant TMR contribution can be excluded.

In order to rule out field-induced magnetostriction [127, 114], we compare the MR values at *zero* applied field: we obtain two distinct resistance levels with an MR ratio of up to 50 % (for an example see Figure 3.7(c)). Apart from the switching event, the resistance levels do not change significantly when a field is applied (Figure 3.7(b,c)), supporting our claim that magnetostriction-related effects do not significantly contribute to the observed resistance change. Lastly, we have also studied pure Ni and Co contacts where we find similar results, indicating that the concurrent presence of Fe and Ni atoms in Py is not responsible for the observed effects.

Ultimately, this indicates that it is the presence of a narrow DW in the ballistic transport regime that leads to this large MR. We can therefore conclude that we unambiguously observe DWMR in the ballistic conduction regime. Given the atomic size of the constriction in this resistance regime, it is the spin structure of the atoms at the very center of the contact, where the DW is located, that gives rise to the significant resistance changes observed.

Numerous models treat DWMR in the diffusive limit but few have considered the ballistic conduction regime (see Section 1.5). The reduced dimensions of such contacts require a self-consistent calculation of both the magnetic as well as the electronic structure of the nanocontact. Recent detailed ab initio calculations of this kind by Czerner et al. [91] yield DWMR values of around 50 % in line with our experimental observation. Jacob et al. [86] conclude that realistic MR values in Ni nanocontacts are of the order of 30 %, similar to what we observe.

A key observation in our experiments is the occurrence of a sign change in the MR for a number of contacts in the ballistic regime (see Figure 3.7(a)). This sign change is in contrast to previous experimental observations, where such behavior was only found in the diffusive and in the tunneling regime [119]. Figure 3.10 shows the quasi-static MR for two consecutive resistance states of a nanocontact: While the resistance changes from 12 kΩ to 9.5 kΩ, the MR jumps from −4 % to 3 %. The corresponding R(H) loops for $\varphi = 75°$ (shown as insets) are

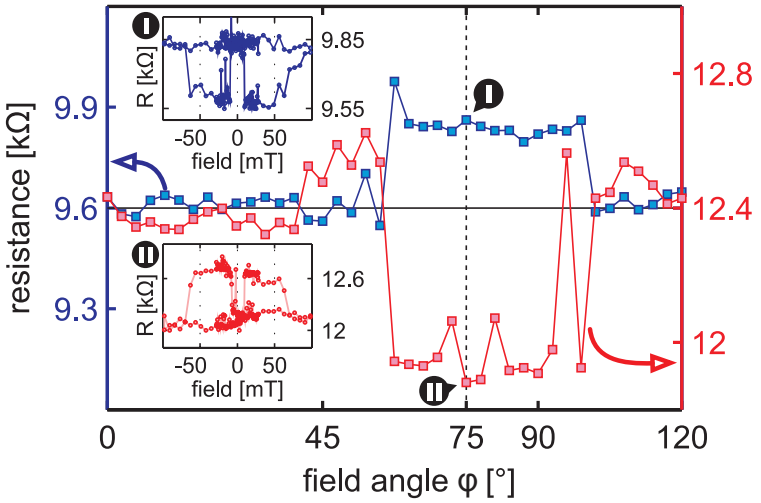

Figure 3.10 | Sign change of the magnetoresistance in the ballistic regime. Resistance of a nanocontact as a function of field angle φ after applying a magnetic field and relaxing it to zero along φ. The data was obtained for two consecutive resistance states of a nanocontact (blue and red), indicating a change in the sign of MR associated with a change in contact resistance. The insets show the corresponding R(H) major loops measured at $\varphi = 75°$ obtained for the same contact configurations.

consistent with this behavior. We attribute the sudden resistance change to a small atomic reconfiguration at the narrowest part of the contact. Interestingly, despite this change, the switching fields between the P and AP states remain at the same field values, allowing us to identify the magnetization configurations as explained above. The simultaneous occurrence of a resistance change and a sign change of the MR points to the same origin of the two effects.

We therefore conclude that the underlying MR associated with the presence of a DW depends on the precise atomic configuration of the constriction. Theoretical approaches that are limited to simple geometries of the constriction, such as single-atomic wires, cannot satisfyingly describe this situation. Recently, Achilles et al. [126] have considered different atomic configurations with resistance values similar to the ones observed in our experiments. Based on spin-dependent density functional theory, the MR is evaluated as the difference in resistance taken with and without a DW. Some of the atomic configurations considered differ only by the position of one or a few atoms. Precisely such atomic rearrangements can be induced by thermal activation, for instance during electromigration. In Reference [126] the authors predict that, depending on the chosen configuration, the MR can be positive or negative with a strongly varying magnitude. This surprising result (in line with our observation) can be understood based on symmetry considerations: It is shown that a reduction of the symmetry of the nanocontact drastically reduces the conduction through the majority channel in the P state $g_P^{\uparrow\uparrow}$. In contrast to that, $g_P^{\downarrow\downarrow}$ and the conduction values in the AP state $g_{AP}^{\uparrow\downarrow/\downarrow\uparrow}$ are much less affected. Depending on the specific symmetries of the contact, this behavior is shown to cause $g_{AP} > g_P$ (negative MR) or $g_{AP} < g_P$ (positive MR). This result corroborates the hypothesis that small changes in the configuration of the nanocontact, arising as changes in the mea-

sured resistance, lead to pronounced changes in the MR (including sign changes). Ultimately, this agreement between theory and experiment suggests that we can attribute the large MR changes to spin-dependent transport through discrete conductance channels that change their transmission depending on the atomic arrangement and the magnetic configuration of the narrowest part of the nanocontact. In addition, it also explains why simpler theories that do not take into account a variable atomic structure cannot explain our experimental results.

4 Concluding remarks

The two experiments discussed above represent one of the most comprehensive and reliable studies of domain wall-induced magnetoresistance effects in magnetic nanocontacts to date. The carefully chosen sample design and measurement scheme allowed us to control the magnetization structure at the constriction while minimizing artifacts due to magnetostriction and impurities. The MR properties were determined by the controlled positioning of a DW in the nanocontact. At the same time, the electromigration technique provided a well-controlled way to generate any desired contact size. With this unique experimental approach, we were able to explore DW-induced MR phenomena in magnetic nanocontacts, both, in the diffusive and the ballistic conductance regime.

Angle-dependent MR measurements of low-resistance contacts ($R_{\mathrm{max}} \approx 540\,\Omega$, contact size $> 1\,\mathrm{nm}$) revealed the existence of three distinct resistance levels at remanence. We show that these levels correspond to specific positions of the DW in the nanocontact. At smaller constriction widths we observed a sign change of the MR difference between the case of a DW pinned at the constriction and the case of a DW positioned next to the constriction. Down to a constriction size of a few nanometers the measured MR ratios did not exceed 1 %. To understand this behavior, we put forward an explanation based on the bulk AMR effect. Numerical simulations of the AMR, taking into account both, the magnetization and the current density as a function of contact size, confirmed our hypothesis qualitatively. A signature of intrinsic DWMR was not observed, though the effect might have been small and buried under the AMR effect.

From these results we draw our first main conclusion that the MR of Py nanocontacts in the diffusive regime is largely dominated by AMR. We therefore consider it extremely important to carefully evaluate the role of AMR when trying to determine the intrinsic signature of domain wall magnetoresistance.

These findings allowed us to separate the AMR from the additionally observed large MR effects in a subsequent study on nanocontacts in the ballistic conduction regime. In contrast to the diffusive regime, here we found large intrinsic DWMR up to 50 % with both positive and

negative sign. For the first time in the ballistic conduction regime, we demonstrated that the reproducible resistance states observed at zero applied magnetic field are associated with two stable magnetic configurations, with and without a DW pinned at the nanocontact. Our comparison of the measured MR behavior with available theoretical models shows that our results can only be reproduced by models that take into account different spatial and magnetic configurations of the atoms at the narrowest part of the nanocontact. Small changes in the atomic configuration, which appear as abrupt changes in the resistance, lead to a large change of the magnitude and even the sign of the MR that we observe. This emphasizes that both sign and magnitude of the DWMR are governed by the precise geometrical arrangement of the constriction on the atomic scale.

We believe that future theoretical work will have to focus even more on analyzing realistic atomic structures including complex magnetization configurations and their mutual interactions. Experiments on the other hand will have to take the degree of control to another level by reaching the ultimate limit of precise atomic control. If feasible, such a combination of research efforts would bring us closer to a complete understanding of the precise correlation between the MR and the atomic configuration.

Our study is, due to its high level of cleanliness and control and the wide resistance range explored, an important step towards understanding the phenomenology of MR phenomena in magnetic nanocontacts. In particular, given the long series of artifact-riddled attempts to measure DWMR in the past 15 years, it is crucial to gather more reliable data. We therefore hope that our results will spur new interest in the field and encourage others to confirm our new findings.

Finally, we believe that our results will be of increasing importance for magnetic nanodevices as dimensions are scaled down. Magnetic nanocontacts might even have the potential to revolutionize data storage technology by pushing the data storage density close to its theoretical limit, the atomic limit. However, there are many hurdles to take to reach that point. In particular, one will have to find a way to reproducibly fabricate *and* control large arrays of nanocontacts, which is, as the complexity of our fabrication process and measurement setup shows, by all means a big challenge.

Part II

Thermoelectric effects and ferromagnetic resonance in laser-heated microstructures

5 Theoretical and experimental background

Part II of this thesis focuses on the analysis of thermoelectric effects that occur in laser-heated metallic microstructures (Chapter 7). Additionally, ferromagnetic resonance measurements are performed in large temperature gradients to investigate the existence of thermally induced spin currents (Chapter 8). This initial chapter provides an overview of the relevant phenomena as well as previous studies related to this work. In Chapter 6 we present and characterize the employed experimental techniques.

5.1 Thermoelectric and thermomagnetic effects

5.1.1 Seebeck effect

It is well-known from basic solid state physics that an electrical conductor (semiconductor or metal) exposed to a temperature gradient develops an internal electric field [128, 129]. In a simplified picture, the effect can be understood as follows: As charge carriers at the hot end of the sample possess on average a higher thermal energy than on the cold side, there is a net diffusion of charge carriers towards the cold end. This charge imbalance gives rise to an electric field that compensates the effect of the temperature gradient and ultimately stops the net charge transfer. In the absence of a charge current ($\boldsymbol{J} = 0$), the generated internal electric field in the steady state is given by $\boldsymbol{E} = -\boldsymbol{\nabla} V = S\boldsymbol{\nabla} T$, where S is the Seebeck coefficient (often called thermopower). The Seebeck coefficient can be expressed by the longitudinal conductivity (σ) and its derivative with respect to energy (σ'), according to the Mott relation [130]

$$S = -\frac{\pi^2 k_B^2 T}{3e}\frac{\partial}{\partial E}\ln\sigma\bigg|_{E_F} = -\frac{\pi^2 k_B^2 T}{3e}\frac{\sigma'}{\sigma}\bigg|_{E_F}, \tag{5.1}$$

where E_F is the Fermi energy and k_B the Boltzmann constant. The effect can be measured in the configuration depicted in Figure 5.1, in which two metallic wires with Seebeck coefficients $S_A \neq S_B$ form a common junction at temperature T_1. The voltage measured between both

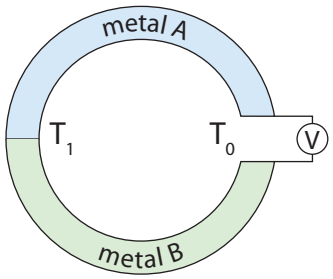

Figure 5.1 | Sketch of a typical Seebeck circuit. When $S_A \neq S_B$, a temperature difference between the junction temperature T_1 and the common reference T_0 gives rise to the Seebeck voltage V.

ends of the wires at the common cold junction temperature T_0 is given by

$$V = -\int_{T_0}^{T_1} (S_A - S_B)\, \mathrm{d}T \,.$$

This configuration, usually called *thermocouple* (TC), finds widespread use in electronic thermometers. For small enough temperature differences $\Delta T = T_1 - T_0$, it is a good approximation to assume that $S(T) = \text{const}$. By defining $S_{TC} \equiv S_B - S_A$ we obtain a (for technical applications very favorable) linear relation between the temperature difference and the resulting voltage:

$$V = -S_{TC}\Delta T \,.$$

More generally, the generation of charge and heat current densities ($\boldsymbol{j}$ and $\boldsymbol{q}$, respectively) by electric fields (∇V) and temperature gradients (∇T) can be expressed by

$$\begin{pmatrix} \boldsymbol{j} \\ \boldsymbol{q} \end{pmatrix} = -\begin{pmatrix} \sigma & \sigma S \\ \sigma\Pi & \kappa \end{pmatrix} \begin{pmatrix} \boldsymbol{\nabla} V \\ \boldsymbol{\nabla} T \end{pmatrix}, \tag{5.2}$$

where σ is the electric conductivity, κ the main contribution to the heat conductivity and Π the Peltier coefficient. As can be readily seen from Equation (5.2), the Peltier effect describes the inverse of the Seebeck effect, i.e. the generation of a heat current by means of a potential gradient (or electric field). As a direct consequence of Onsager's reciprocity relation [131], the corresponding coefficients are linked by the Thomson relation $\Pi = ST$.

5.1.2 Nernst effect

The Nernst effect [132] belongs to the class of thermo*magnetic* effects that describe thermoelectric phenomena in non-magnetic conductors subject to a constant magnetic field (for a review see Reference [129]) as well as in magnetic conductors: the *Righi-Leduc effect* is a heat flow resulting from a temperature gradient in the presence of a perpendicular magnetic field. Very similarly, the *Ettingshausen effect* leads to a temperature gradient perpendicular to

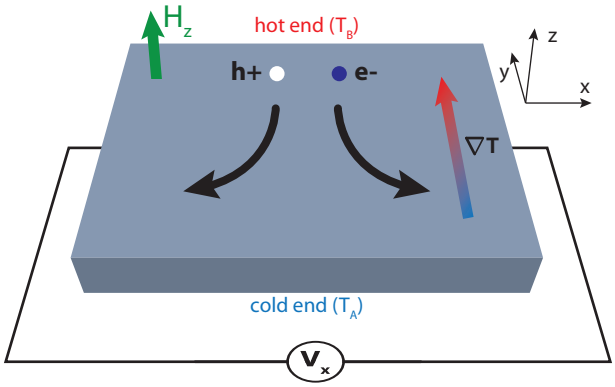

Figure 5.2 | Illustration of the Nernst effect for the general case of a non-magnetic conductor exhibiting both holes and electrons as charge carriers. (Figure adapted from Ref. [129]).

an applied electric current. Finally, the *Nernst effect* is observed when a sample is subjected to a temperature gradient ∇T and a perpendicular magnetic field H (e.g. along y and z, as illustrated in Figure 5.2). The effect results in an electric field $\boldsymbol{E}_{\mathrm{NE}}$ along x, normal to both ∇T and H. Hence, the effect is commonly described by the relation $\mathbf{E}_{\mathrm{NE}} = -N\mu_0 \mathbf{H} \times \boldsymbol{\nabla} T$, where N is the Nernst coefficient.

A simplified microscopic explanation of the effect is illustrated in Figure 5.2 for the general case of a conductor exhibiting both holes and electrons as charge carriers: As discussed previously (see Section 5.1.1), by applying a temperature gradient to a conducting sample, the charge carriers acquire a net drift velocity towards the cold end of the sample. Due to the magnetic field H_z, the electrons and holes experience a Lorentz force oriented along x and $-x$, respectively. The resulting charge built-up at the sample faces leads to a measurable voltage drop V_{x}. To first order, this transverse voltage is zero as there is obviously no net charge current in the stationary state. In fact, the Nernst effect is a second order effect due to the modulated charge carrier statistics arising from the temperature gradient. The effect can be derived more rigorously from a semi-classical single-band electron model (see Section 2.3 in [133]).

The same phenomenon can be observed in magnetic materials, where the resulting electric field depends on the sample's magnetization instead of the magnetic field, according to

$$\mathbf{E}_{\mathrm{ANE}} = -N_{\mathrm{ANE}}\, \boldsymbol{m} \times \nabla T\,, \tag{5.3}$$

where $\boldsymbol{m} = \boldsymbol{M}/|\boldsymbol{M}|$ is the reduced magnetization. In this case, the effect is called *anomalous Nernst effect* (ANE). While the Nernst effect and the *anomalous* Nernst effect (ANE) are phenomenologically similar, the true physical origin of the ANE is not as straightforward as described above. In fact, the ANE turns out to be closely related to the *anomalous Hall effect* (AHE). When applying a current $\boldsymbol{j}$ normal to the magnetization $\boldsymbol{M}$ of a FM, the AHE gives rise to a transverse voltage associated with the transverse Hall conductivity σ_{xy}. Its

origin can be of extrinsic (spin-dependent scattering) or intrinsic (Berry phase effect) nature[1]. Recent experimental [136, 137] and theoretical [138] results suggest that ANE and AHE have a common origin and that the Mott relation of Equation (5.1) also holds for the transverse conductivity. The latter immediately yields the transverse electric field (or voltage), in line with experimental observations of the ANE.

5.2 Spin caloritronics: *spin* Seebeck effect and beyond

Research in the field of spin caloritronics aims at understanding the interactions of spins and spin excitations with heat currents. A distinction is made between (i) *independent electron effects* in ferromagnetic metals and (ii) *collective effects* related to magnetization dynamics. In the following sections we provide a brief introduction to the main concepts that represent the basis and motivation for the measurements presented in Chapters 6 to 8. A more thorough review on spin caloritronics has been published very recently in a special issue of Nature Materials [4].

5.2.1 Independent electron effects and thermal spin-transfer torque

The effects belonging to (i) can be understood in terms of a spin-dependent generalization of the thermoelectric effects presented above. As discussed in Chapter 1, spin-polarized electron transport is often described in terms of the two-channel model. We can thus define the total electric current density as $\boldsymbol{j} = \boldsymbol{j}^{\uparrow} + \boldsymbol{j}^{\downarrow}$ and the spin current density as $\boldsymbol{j}_s = \boldsymbol{j}^{\uparrow} - \boldsymbol{j}^{\downarrow}$. Similarly, the effective and the spin-dependent polarization electric conductivities are given by $\sigma = \sigma^{\uparrow} + \sigma^{\downarrow}$ and $\sigma_s = \sigma^{\uparrow} - \sigma^{\downarrow}$, respectively. Applying this model to the thermoelectric relation of Equation (5.2) yields a thermodynamic three-current model, as described by Brechet and Ansermet in [139]

$$\begin{pmatrix} \boldsymbol{q} \\ \mathbf{j} \\ \mathbf{j}_s \end{pmatrix} = -\begin{pmatrix} \kappa T & \sigma S T & \sigma_s S_s T \\ \sigma S T & \sigma & \sigma_s \\ \sigma_s S_s T & \sigma_s & \sigma \end{pmatrix} \begin{pmatrix} \boldsymbol{\nabla} T/T \\ \boldsymbol{\nabla} V \\ \frac{1}{e}\boldsymbol{\nabla}\left(\Delta\mu\right) \end{pmatrix}, \tag{5.4}$$

where $S = \frac{\sigma^{\uparrow}S^{\uparrow}+\sigma^{\downarrow}S^{\downarrow}}{\sigma^{\uparrow}+\sigma^{\downarrow}}$ is the Seebeck coefficient and $S_s = \frac{\sigma^{\uparrow}S^{\uparrow}-\sigma^{\downarrow}S^{\downarrow}}{\sigma^{\uparrow}-\sigma^{\downarrow}}$ is the spin polarization Seebeck coefficient. $\Delta\mu$ is the difference in chemical potential between spin-up and spin-down charge carriers, i.e. the spin accumulation. In addition to the thermoelectric Seebeck/Peltier effect (coefficient $ST = \Pi$), heat transport (κ) and spin-polarized charge transport (σ_s), the relation describes two new spin-dependent thermoelectric effects: the generation of a spin current by means of a temperature gradient, called *spin-dependent Seebeck effect*, and the inverse effect, a heat current driven by spin accumulation, the *spin-dependent Peltier effect* (both are proportional to $\sigma_s S_s$).

[1] A more specific description of these mechanisms goes beyond the scope of this work. A comprehensive review on the AHE can be found in References [134, 135].

The spin-dependent Seebeck effect has been observed experimentally by driving a heat current (without any charge current) across a ferromagnet/normal metal (FM|NM) interface in a lateral non-local spin-valve geometry [140]. Due to the spin-dependence of the Seebeck effect, a spin current is injected into the NM, giving rise to a spin accumulation (see Section 1.1). By keeping the device dimensions small (distances and wire widths $\sim 100\,\mathrm{nm}$), the authors were able to detect the exponentially decaying spin accumulation in the NM using a second FM contact. In a similar study the same authors also demonstrated the spin-dependent Peltier effect [141].

In analogy to well-known MR effects, such as GMR and TMR (see Section 1.1), a pronounced dependence of spin-dependent thermoelectric effects on the magnetization configuration (parallel/anti-parallel configuration of the FM layers) has been predicted for spin valve structures and tunnel junctions [142]. Such a dependence, termed (giant/tunnel) magneto-Seebeck or Peltier effect, has been observed in a number of experimental studies: very early on (in this group) in multilayered magnetic nanowires [143] and recently for instance also in MgO [144] and Al_2O_3 [145] tunnel junctions, where very large magneto-Seebeck effects could be attained.

In Reference [140] Slachter *et al.* argue that the process of thermal spin injection can compete with electrical spin injection in terms of efficiency. In particular, the authors estimate that already a temperature difference of a few tens of K would be sufficient to generate the critical spin current density required for magnetization switching based on a thermally induced spin-transfer torque (STT, see also Section 5.3.3). The existence of such a thermal STT (a *collective* effect) was predicted theoretically [146]. Recently, it was observed experimentally in this group [147]. However, the model of Reference [146] did not apply unless one would assume unexpected values of the Seebeck coefficient. Instead, the model of Equation (5.4), which refers to a volume effect, not an interface effect, accounted for the data without unrealistic adjustment of the parameters. Experimental studies that focus on thermal STT in magnetic tunnel junctions or its effect on domain wall motion are expected to lead to new insights in the near future [4]. Also in the case of tunnel junctions, it may turn out that the thermal STT represents a viable alternative to the well-explored STT based on electrical currents.

5.2.2 Spin Seebeck effect

The *spin* Seebeck effect (SSE), first demonstrated experimentally in 2008 by Uchida *et al.* [20], is conceptually different from the spin-dependent thermoelectric phenomena discussed above. It describes the generation of a bulk spin current $\boldsymbol{j}_s$ (over macroscopic distances) in ferromagnetic materials due to a temperature gradient $\boldsymbol{\nabla} T$ along $\boldsymbol{m}$. Figure 5.3 shows the two basic configurations, in which the effect has been observed experimentally. In both cases the spin current is injected from a ferromagnetic layer into a normal metal (NM) with very strong spin-orbit coupling (e.g. Pt), where it generates a transverse voltage via the inverse spin-Hall effect (ISHE, [148, 149]) The resulting electric field in the NM is given by the mutual orientation of the spin current $\boldsymbol{j}_s$ and the spin polarization vector $\boldsymbol{\sigma}_{\mathrm{spin}} \parallel \boldsymbol{M}$, according to

$$\boldsymbol{E}_{\mathrm{ISHE}} \propto \boldsymbol{j}_{\mathrm{s}} \times \boldsymbol{\sigma}_{\mathrm{spin}} \,.$$

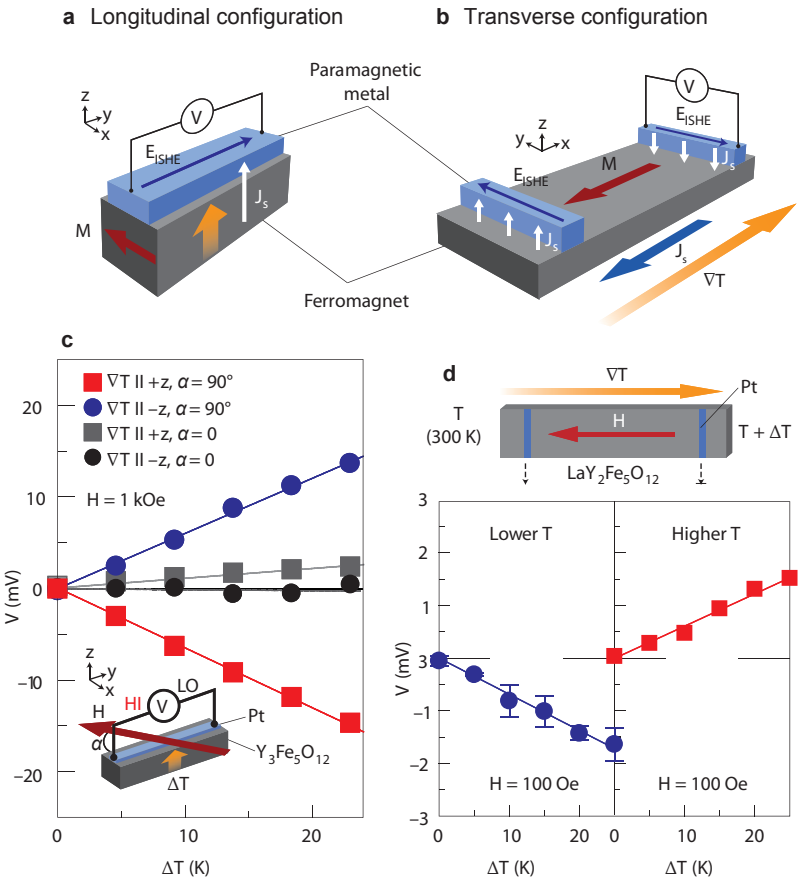

Figure 5.3 | The spin Seebeck effect in longitudinal (a) and transverse (b) configuration. The thermally generated spin current J_s is injected into a normal metal with strong spin-orbit interaction (usually Pt). Via the inverse spin-Hall effect (ISHE) the injected spin current generates a measurable voltage normal to the magnetization direction. (c) and (d) show typical measurement data obtained from measurements on a YIG/Pt sample in configuration (a) and (b), respectively. (Figure taken and adapted from References [4, 20])

The effect has been demonstrated in a range of different materials [4]: in ferromagnetic metals, such as Py [20], ferromagnetic semiconductors [150], magnetic insulators, such as yttrium iron garnet (YIG) [151], and even in non-magnetic materials [152].

Thermodynamically, the SSE can be explained in terms of the three-current model derived from Onsager's reciprocity relation (Equation (5.4)): Suppose an unbiased metallic sample (i.e. charge current $\boldsymbol{j} = 0$ and bulk spin accumulation $\Delta\mu = 0$) subject to a temperature gradient $\boldsymbol{\nabla} T$. Under these boundary conditions, Equation (5.4) yields the spin current $\boldsymbol{j}_s = -\sigma\,(S_s - S)\,\boldsymbol{\nabla} T$. As this result is independent of the spin diffusion length, such a thermally generated spin current should persist even on large scales (for a detailed discussion see Reference [139]).

Microscopically, the SSE is far less understood. One of the most widely accepted theoretical models for the SSE in ferromagnetic insulators explains the effect in terms of thermally excited spin currents across the FM|NM interface [4, 153]. First, thermal excitations of the FM spin

system inject a spin current into the adjacent NM via spin pumping (see Section 5.3.3). Such thermal excitations, governed by an effective magnon temperature T_F, can be induced by magnon heat currents (magnon-driven spin Seebeck effect) and/or phonon heat currents via the substrate (phonon-drag spin Seebeck effect). Second, electronic noise in the NM (governed by the electron temperature T_N) gives rise to partly spin-polarized currents that inject a spin current back into the FM. While the effects cancel out in thermal equilibrium, applying a temperature gradient to the FM might lead to a difference between T_N and T_F. According to the model, this is expected to result in a non-zero spin current across the FM|NM interface – as observed experimentally. However, due to the novelty of the effect and the small number of available experimental studies, the precise origin of the effect is still subject of discussion. For instance, very recently Agrawal *et al.* presented experimental data that indicate no significant difference between the magnon and phonon temperatures in a YIG|Pt structure in the transverse configuration [154] – which is one of the main assumptions of the model discussed above.

A microscopic model is completely lacking for the SSE in *metallic* samples, such as Py|Pt. In the pioneering experiment in the transverse configuration, where narrow Pt strips cross a wide Py pad subject to an in-plane temperature gradient, the voltage was shown to depend on the position of the Pt strip along the heat gradient in the FM (see Figure 5.3(d)). In particular, the signal changes its sign at the center of a several mm long sample. Initially [20], the temperature gradient within the FM was believed to cause the spin-dependent chemical potentials $\mu^{\uparrow}$ and $\mu^{\downarrow}$ to tilt, generating a position-dependent spin accumulation and thus a spin current $\boldsymbol{j}_s \parallel \boldsymbol{\nabla} T$. This was a surprising result, since metallic FMs are known to exhibit short spin-diffusion and magnon mean free path lengths. Therefore, in mm-sized samples, electron-mediated and magnon-mediated mechanisms within the FM layer, like the one presented above for magnetic insulators, are not likely to play a significant role. More recently, experimental data and new models [155, 156] seem to suggest that the SSE could be driven by phonons in the substrate that interact with the magnetization in the FM layer.

In addition to the uncertainty regarding the physics underlying the SSE, it has become a hotly debated question to what extend artifacts may play a role in SSE experiments and even whether the SSE exists at all. Most experimental demonstrations of the SSE claim that artifacts due to the ANE (see Section 5.1.2) can be excluded because the temperature gradient is applied in the plane of the sample along $\boldsymbol{m}$ and hence $\boldsymbol{V}_{ANE} \propto \boldsymbol{m} \times \boldsymbol{\nabla} T \approx 0$. However, several experiments [157, 158] and numerical calculations [159] have shown that generating a pure and homogeneous in-plane temperature gradient in a FM film attached to a substrate can be challenging. The original (transverse) spin Seebeck geometry (Figure 5.3(b)) is particularly prone to artifacts due to spurious (i.e. out-of-plane) temperature gradients, as heat conduction to and from the substrate cannot be neglected (see also the discussion of temperature profiles in Section 6.2.2). Hence, it is crucial to rigorously consider contributions to the transverse voltage due to the ANE.

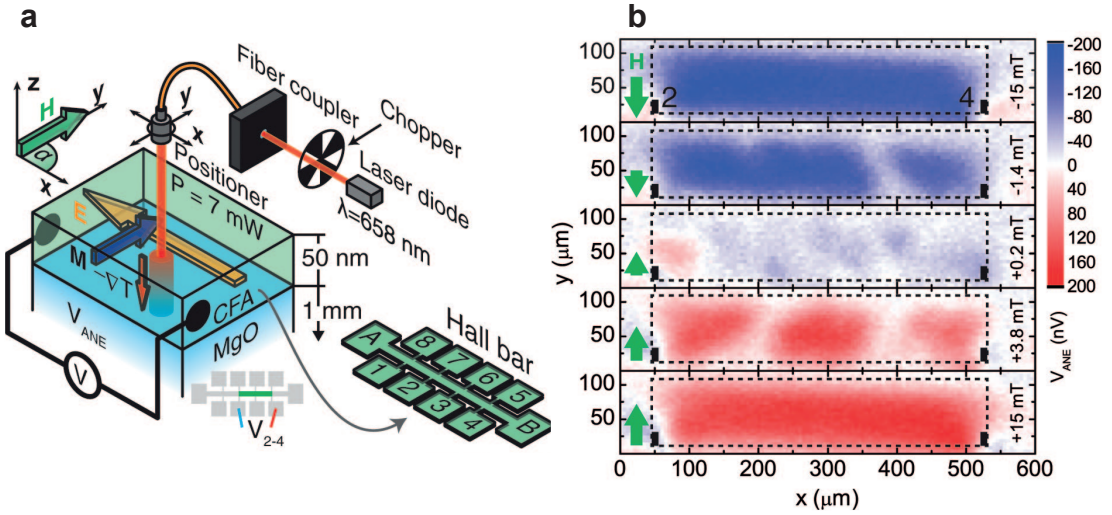

Figure 5.4 | Spatially resolved measurement of the anomalous Nernst effect as performed by Weiler *et al.* [160]. (a) Schematic illustration of measurement setup: a scanning laser beam (with diameter d = 10 µm) induces a temperature gradient perpendicular to the sample plane. The in-plane magnetization of the Co_2FeAl is controlled by a rotatable in-plane field H. The resulting ANE signal is measured using electrical contacts. (b) Position-dependent ANE voltage of a 0.5 mm long section of the Hall bar for different external magnetic fields, indicating the gradual reversal of the magnetization in the probed region. Figure taken from Reference [160].

Indeed, the experimental results shown in References [157, 158] confirm the presence of ANE due to an out-of-plane temperature gradient. The authors come to the conclusion that the ANE accounts for a part of the SSE voltage, possibly even for the entire signal. Recently, Weiler *et al.* addressed these issues by performing spatially resolved measurements of both ANE and longitudinal SSE using laser-induced heating [160] (see Figure 5.4). The voltage generated by the laser-induced out-of-plane temperature gradient was report to be dominated by the ANE for metallic FM thin films (Co_2FeAl or Ni without Pt on top) and by the SSE in YIG|Pt bilayers. Their results illustrate the similarity of ANE and SSE in both magnitude and symmetry. This underlines once more that great care has to be taken when identifying the origin of the transverse voltage in SSE experiments.

In principle, the SSE in magnetic insulators should not suffer from artifacts of this kind. Insulators (YIG) and materials without a spontaneous magnetization (Pt) are not expected to exhibit any ANE. However, recent data suggest that YIG induces magnetic moments in an attached Pt layer due to the magnetic proximity effect [161]. If the effect is sufficiently strong, the Pt layer in a YIG|Pt bilayer (longitudinal SSE configuration) could generate a significant ANE voltage. Due to the identical symmetry of the effects, the resulting signal would be hard to distinguish from the expected SSE.

Especially given the issue of possible artifacts and the still small number of material systems investigated, it is evident that more systematic investigations are needed. Future investigations will have to thoroughly assess the role of thermoelectric artifacts and the magnetic proximity

effect in both SSE configurations, possibly using novel approaches, to help clarifying the mechanism of SSE in general.

One of the (novel) ways considered experimentally to produce a large spin Seebeck effect is to shine a Gaussian laser beam on the sample [160]. Consequently, we decided to study in detail the voltages that appear on Py strips heated by a laser spot. We identified a charging problem, we demonstrated that we can quantify the obtained Seebeck voltage and we found clear evidence for an anomalous Nernst effect by using time resolved measurements. We have also tried to see if a heat-driven spin current may influence the ferromagnetic resonance (FMR) of Py. Hence, we give in what follows a quick summary of the basic principles of FMR.

5.3 Ferromagnetic resonance

In this section we provide a brief introduction to ferromagnetic resonance (FMR), the generation of the AMR voltage in metallic ferromagnets and the spin-transfer torque (STT). A more detailed treatment of the theoretical and experimental basics of FMR can be found in textbooks, such as References [162, 163].

5.3.1 Spin precession

We know from electromagnetism that a magnetic moment $\boldsymbol{\mu}$ in a homogeneous magnetic field $\boldsymbol{H}$ experiences the torque $\boldsymbol{\tau} = \mu_0 \boldsymbol{\mu} \times \boldsymbol{H}$. In the macrospin approximation, where the magnetization of the entire sample is expressed by a macroscopic magnetization vector $\boldsymbol{M}$, this equation becomes

$$\frac{\mathrm{d}\boldsymbol{M}}{\mathrm{d}t} = -\mu_0 \gamma \boldsymbol{M} \times \boldsymbol{H}_{\mathrm{eff}} \,. \tag{5.5}$$

Here, μ_0 is the vacuum magnetic permeability, $\gamma = \frac{e}{2m_e} g_e \approx 2\pi \cdot 2.8 \frac{\mathrm{MHz}}{\mathrm{Oe}}$ is the electron gyromagnetic ratio and $\boldsymbol{H}_{\mathrm{eff}}$ is the internal effective field that includes additional contributions to $\boldsymbol{H}$, such as effective fields due to shape anisotropy and crystalline anisotropy. The solution of this equation describes the precession of the magnetization vector $\boldsymbol{M}$ around the magnetic field $\boldsymbol{H}_{\mathrm{eff}}$. In the absence of damping, this corresponds to a free infinite precession with the Larmor frequency $\omega_0 = \mu_0 \gamma H_{\mathrm{eff}}$ and cone angle θ, as illustrated in Figure 5.5(a).

In general, there are two types of damping: While *longitudinal damping* describes the relaxation of the magnetization along the direction of the effective field ($\boldsymbol{H}_{\mathrm{eff}} \parallel \hat{z}$ in Figure 5.5), *transverse damping* describes the decay of the magnetization components perpendicular to $\boldsymbol{H}_{\mathrm{eff}}$. In a saturated ferromagnetic sample, it is a good approximation to assume that the magnitude of the magnetization is constant along the direction of saturation, i.e. longitudinal damping is negligible. Hence, spin relaxation in a ferromagnet is often described by only one phenomenological damping parameter, usually called α. Microscopically, magnetization damping is a complex process. Inelastic conduction electron scattering, phonon scattering

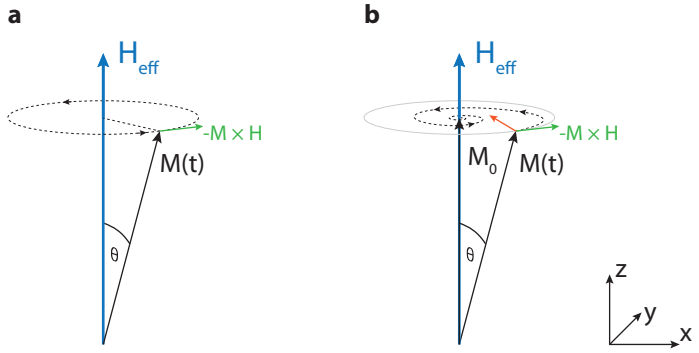

Figure 5.5 | Precession of the magnetization $\boldsymbol{M}$ in a static magnetic field $\boldsymbol{H}_{\text{eff}}$ (a) with and (b) without damping. In equilibrium the magnetization is aligned with the field, i.e. $M_z = M_0$. Green arrows denote the direction of the torque that induces precession, the red arrow in (b) indicates the direction of the damping term $\alpha \frac{\boldsymbol{M}}{|\boldsymbol{M}|} \times \frac{\mathrm{d}\boldsymbol{M}}{\mathrm{d}t}$ for $\alpha > 0$.

and magnon/spin wave scattering are only some of the possible mechanism through which the spin system can transfer angular momentum.

The magnetization dynamics in a ferromagnet with magnetization relaxation is commonly described by the *Landau-Lifshitz equation in Gilbert's notation* (LLG equation):

$$\frac{\mathrm{d}\boldsymbol{M}}{\mathrm{d}t} = -\mu_0 \gamma \boldsymbol{M} \times \boldsymbol{H}_{\text{eff}} + \alpha \frac{\boldsymbol{M}}{|\boldsymbol{M}|} \times \frac{\mathrm{d}\boldsymbol{M}}{\mathrm{d}t} \,. \tag{5.6}$$

The second term introduces magnetization relaxation towards $\boldsymbol{H}_{\text{eff}}$, perpendicular to both $\boldsymbol{M}$ and $\mathrm{d}\boldsymbol{M}/\mathrm{d}t$. The Gilbert damping constant α defines the strength of the damping and is generally material-dependent. When $\alpha > 0$ the precession of the magnetization vector $\boldsymbol{M}$ spirals down to the equilibrium magnetization along the field direction $M_0\hat{z}$, as illustrated in Figure 5.5(b).

5.3.2 Uniform excitation: Ferromagnetic resonance

In the previous section we have treated the damped precessional motion of the magnetization and the resulting alignment with the magnetic field. Here we look at the steady state precession of the magnetization induced by a homogeneous excitation in a microwave field. We adapt the geometry given in Figure 5.5(b) and add a harmonic high frequency field of the form $h_{\text{hf}} = h_x e^{i\omega t}$ applied along the x-axis. In this geometry, the vectors for the magnetization and the effective field are

$$\boldsymbol{M} = \{m_x e^{i\omega t},\ m_y e^{i\omega t},\ M_0\} \qquad \text{and} \qquad \boldsymbol{H} = \{h_x e^{i\omega t},\ 0,\ H_0\} \,.$$

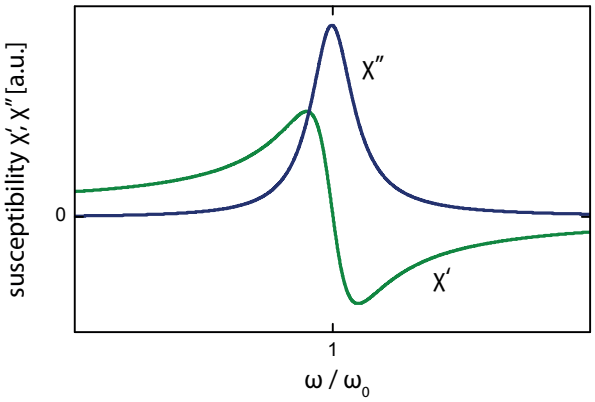

Figure 5.6 | Real and imaginary parts of the susceptibility χ.

As $m_{x,y} \ll M_0$ we can neglect changes in M_z and the equations of motion given by Equation (5.5) become

$$i\omega m_x = \mu_0 \gamma H_0 m_y \qquad \text{and} \qquad i\omega m_y = \mu_0 \gamma (M_0 h_x - m_x H_0) \,.$$

With $\omega_0 = \mu_0 \gamma H_0$ and $\omega_M = \mu_0 \gamma M$ we obtain for the transverse susceptibility without considering dissipation (i.e. $\alpha = 0$)

$$\chi_{xx} = \frac{m_x}{h_x} = \frac{\omega_0 \omega_M}{\omega_0^2 - \omega^2} \,.$$

For $\omega = \omega_0$ the microwave field is in resonance with the spin system and the precession amplitude m_x diverges. In a more realistic scenario with $\alpha > 0$ the resonance is broadened and the susceptibility becomes

$$\chi_{xx} = \frac{\omega_M(\omega_0 + i\alpha\omega)}{(\omega_0 + i\alpha\omega)^2 - \omega^2} \,. \tag{5.7}$$

More generally, the response of the oscillating part of the magnetization $\boldsymbol{m}(t)$ to a high-frequency field $\boldsymbol{h}_{\text{hf}}$ can be written as $\boldsymbol{m}(t) = \hat{\boldsymbol{\chi}} \boldsymbol{h}_{\text{hf}}$ where the susceptibility tensor $\hat{\boldsymbol{\chi}}$ is called *Polder tensor*. Here we discuss the simple case described above where we consider only χ_{xx} (in the following called χ).

Figure 5.6 shows the real and imaginary part of the susceptibility χ' and χ'', respectively. In this case, χ' is the response of m_x in phase with the excitation and χ'' is the dissipation term. On resonance ($\omega = \omega_0$) the dissipation is maximum and χ' crosses zero as the magnetization precession and excitation are out of phase by 90°. It can be shown that the microwave power absorbed by a magnetic sample is proportional to χ''. Hence, in a standard FMR experiment,

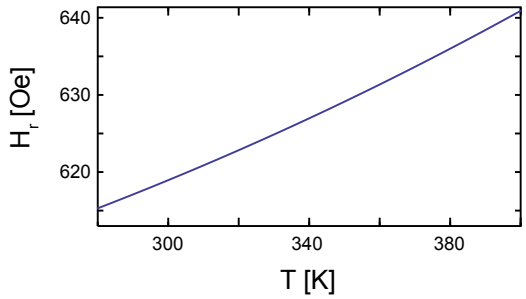

Figure 5.7 | Estimated temperature dependence of the resonance field H_r in Py for $f = \omega/2\pi = 7.19\,\text{GHz}$ and $M_0(293\,\text{K}) \approx 10.053\,\text{kOe}$.

where the microwave frequency is kept constant and the external magnetic field is swept through the resonance, the FMR lineshape (a Lorentzian line, see Equation (5.7) and Figure 5.6) is obtained by measuring the absorption as a function of the DC field H_0. Under this condition, the linewidth (FWHM) of χ'' is given by $\Delta H = \Delta H_i + \Delta H_G$. Here ΔH_i denotes the inhomogeneous broadening that may arise due to sample defects or inhomogeneities in the DC or excitation fields. ΔH_G is the broadening due to intrinsic (Gilbert) damping given by [164]

$$\Delta H_G = \frac{2\omega}{\gamma}\alpha\,.$$

Permalloy has a Gilbert damping parameter of about $\alpha \approx 0.008$ [165]. For a resonance frequency of $\omega = 2\pi f = 2\pi \cdot 7.19\,\text{GHz}$, one obtains an intrinsic linewidth of $\Delta H_G \approx 41\,\text{Oe}$.

In magnetic thin films, such as the Permalloy wires studied in this thesis, shape anisotropy has a significant effect on the precessional motion and the resonance frequency. In a thin film with thickness $\ll$ width and length, the demagnetizing field $\boldsymbol{H}_d = -\hat{\boldsymbol{N}}_d \boldsymbol{M}$ due to the conservation of magnetic flux at the sample surfaces (i.e. $\text{div}(\mu_0(\boldsymbol{H}+\boldsymbol{M})) = 0$), is dominated by the component perpendicular to the film plane. A film (or wide wire) in the x-z plane with H_0 applied along z and h_{hf} applied along x has an effective field of $\boldsymbol{H}_{\text{eff}} = \boldsymbol{H}_0 + \boldsymbol{H}_d = H_0\hat{\boldsymbol{z}} + M_0\hat{\boldsymbol{y}}$. $\boldsymbol{M}$ will thus follow an elliptical trajectory in the x-y plane with its minor axis along y. Solving the equations of motion taking into account the demagnetizing field term gives the resonance frequency

$$\omega_0 = \mu_0\gamma\sqrt{H_0(H_0+M_0)}\,. \tag{5.8}$$

For a thin film of Permalloy with saturation magnetization $M_0 = 10.053\,\text{kOe}$ in an external field of $H_0 = 600\,\text{Oe}$ we obtain $f_0 = \omega_0/2\pi \approx 7.08\,\text{GHz}$. This is an increase by a factor of about 4.2 compared to the bulk value $f_0 = \frac{1}{2\pi}\mu_0\gamma H_0$.

Since the saturation magnetization M_0 is a function of temperature, the resonance field H_r (or the resonance frequency if the field is kept constant) is expected to shift when the temperature of the sample is increased. For $T \ll T_C$, the thermal demagnetization is dominated by the

excitation of spin waves. To a first approximation, this can be described by *Bloch's* $T^{3/2}$*-law*: $\Delta M(T) = -M_0 \alpha T^{3/2}$ [166]. The itinerant nature of spins in metallic ferromagnets can be accounted for by adding a correction term of order T^2 [167]:

$$\frac{M(T)}{M_0} = 1 - \beta T^{3/2} - \beta_1 T^2 \,,$$

where $\beta \approx 5.5 \times 10^{-6}\,\mathrm{K}^{-3/2}$ and $\beta_1 \approx 3 \times 10^{-7}\,\mathrm{K}^{-2}$ for Py [167]. Based on $M(T)$ we can now predict the change in H_0 for elevated temperatures, as shown in Figure 5.7 for up to $\Delta T \approx 90\,\mathrm{K}$ above room temperature. We will use this result in the following chapters to deduce a rough estimate of the temperature rise from the shift of the resonance field.

5.3.3 Spin-transfer torque

When a spin-polarized current or a pure spin current is injected into a FM, electron spins that are oriented non-collinear with the local magnetization become aligned and lose their transverse angular momentum. The absorption occurs within the transverse spin coherence length, which has been shown to be of the order of 1 nm [168]. As spin angular momentum has to be conserved, the angular momentum absorbed by the ferromagnet exerts a torque on the magnetization according to the spin-transfer torque (STT) term [17, 169]

$$\left(\frac{\mathrm{d}\boldsymbol{m}}{\mathrm{d}t}\right)_{\mathrm{STT}} = -\frac{\gamma\hbar}{2eM_0V}\boldsymbol{m} \times (\boldsymbol{m} \times \boldsymbol{I}_{\mathrm{S}}) \,, \tag{5.9}$$

where $\boldsymbol{m} = \boldsymbol{M}/|\boldsymbol{M}|$ is the reduced magnetization, V the volume of the ferromagnet and $\boldsymbol{I}_S$ the spin current.

Equation (5.9) is usually used as an additional term in the LLG equation (Equation (5.6)) to describe spin-torque induced phenomena, such as current-induced switching, spin pumping or spin-torque oscillation (A recent in-depth review of the effect and its applications in spintronics devices can be found in Reference [18]). Depending on the polarization of the absorbed spin current, the torque is oriented either parallel or anti-parallel to the Gilbert damping term (see Figure 5.5) and thus gives rise to additional damping or excitation. Indeed, there is experimental evidence that the effect of a spin current on the FMR is detectable: Ando *et al.* [170] used the ISHE in Pt to generate a spin current that diffuses into a Permalloy thin film. The injected spin current was found to modulate the FMR signal, confirming the effect of the STT on the magnetization relaxation in the Py film. In Chapter 8 we attempt the detection of thermally generated spin currents by means of FMR measurements. The inverse effect, i.e. the generation of a spin current in a NM by magnetization precession in an adjacent FM layer, is called *spin pumping* [171].

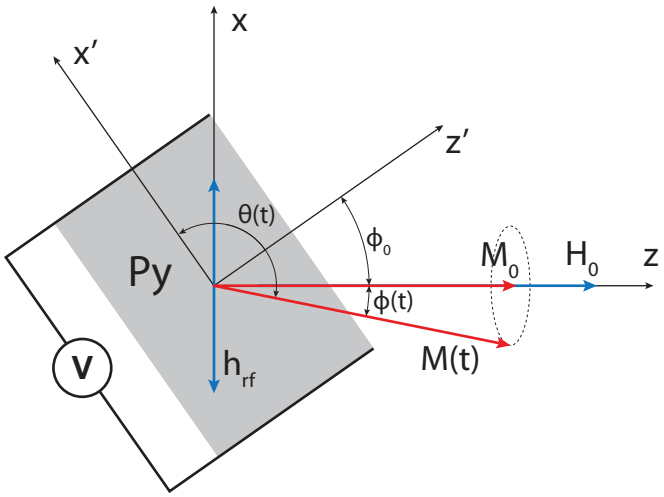

Figure 5.8 | Electrical detection of FMR: Illustration of sample orientation with respect to RF field h_{rf} and measurement contacts. The angle ϕ_0 denotes the rotation of the sample coordinate system (z'-x') with respect to the excitation and DC magnetic fields along x and z, respectively. $\phi(t)$ is the in-plane angle between the magnetization and H_0. (Figure adapted from Reference [172])

5.3.4 Anisotropic magnetoresistance voltage generated by FMR

As we have seen in part I (Section 1.5.1) of this thesis, the anisotropic magnetoresistance effect (AMR) causes the resistivity of a ferromagnetic sample to depend on the direction of the current $\boldsymbol{I}$ relative to the magnetization $\boldsymbol{M}$. The AMR typically follows a $\cos^2\theta$-behavior, where θ is the angle between $\boldsymbol{M}$ and $\boldsymbol{I}$. When performing FMR in the geometry described in the previous section, the in-plane microwave field $h_{\mathrm{rf}} = h_x e^{i\omega t}$ along x induces a transverse RF current $I(t) = I_0\cos(\omega t)$ along z. The projection of the induced current on the measurement direction x' (see Figure 5.8) yields the AMR voltage

$$V_{\mathrm{AMR}}(t) = (R_0 + R_A\cos^2\theta(t))(I(t)\sin\phi_0)\,,$$

where R_0 and R_{A} are the base resistance of the sample and the AMR amplitude, respectively. ϕ_0 denotes the rotation of the sample and $\theta(t)$ is the angle between $\boldsymbol{M}(t)$ and the current along the measurement direction. If the angle of the magnetization precession is small, the time average of $V_{\mathrm{AMR}}(t)$, i.e. the measurable DC signal, gives [172]

$$V_{\mathrm{AMR}}(H,\phi_0) \propto h_{\mathrm{rf}}\left[\frac{\Delta H^2\cos\varphi}{(H_0-H_{\mathrm{r}})^2+\Delta H^2} - \frac{(H_0-H_{\mathrm{r}})\Delta H\sin\varphi}{(H_0-H_{\mathrm{r}})^2+\Delta H^2}\right]\sin 2\phi_0\sin\phi_0\,, \tag{5.10}$$

where φ is the phase angle between the time-dependent magnetization $\boldsymbol{M}(t)$ and the induced RF current. φ is difficult to measure experimentally [173]. At the same time, however, it is a crucial parameter as it determines the symmetry of the FMR-induced voltage with respect to the resonance field H_{r}. Only for $\varphi = 0°$ ($\varphi = 90°$) we obtain a purely symmetric (anti-symmetric)

signal (similar to χ'' and χ' in Figure 5.6), otherwise the resonance signal is a convolution of the two components [174].

Another key parameter is the relative orientation of the sample and the measurement direction: the AMR voltage scales with $\sin 2\phi_0 \sin \phi_0$. Due to the $\cos^2 \theta$ symmetry of the AMR, the signal vanishes for both $\phi_0 = 0°$ and $\phi_0 = 90°$. In the case of a narrow wire oriented parallel to x' with in-plane shape anisotropy, this excludes the two basic configurations where the field is applied along the magnetic easy or the hard axis. The absolute value of the AMR voltage reaches a maximum for $\phi_0 = n \cdot 2\pi \pm 2\tan^{-1}\left(\sqrt{2 \pm \sqrt{3}}\right)$, for example at 54.7°. The electrical detection of FMR (EDFMR) in Chapters 7 and 8 is therefore carried out at angles close to one of these maxima ($\phi_0 \approx 45°$ for most of the data shown). Furthermore, we fit our measurement data with an asymmetric Lorentzian (similar to Equation (5.10)), allowing us to extract the linewidth and the resonance field for an arbitrary phase φ (see Section 6.3.2).

6 Experimental techniques

Studying thermomagnetic effects and ferromagnetic resonance (FMR) simultaneously in microstructured thin films requires a complex measurement setup. For the experiments presented in the following chapters, our setup has to provide a stable magnetic field, low-noise electrical contacts, precise sample positioning (better than 1 µm accuracy), a strongly focused laser beam (< 4 µm spot size) and local microwave excitation. The following pages will provide an overview of the most important parts and the techniques used.

6.1 Sample design and fabrication

Our measurements are based on two different sample batches fabricated by Florian Brandl from the group of Prof. Grundler (TUM, Munich). The substrate in batch I consists of GaAs with an insulation layer of 300 nm SiO_2 grown by sputter deposition. The GaAs is monocrystalline and undoped and has a specific resistivity of $\rho = 5 \times 10^7\,\Omega\,\mathrm{cm}$. Batch II is based on insulating monocrystalline MgO that is expected to offer much better electrical insulation characteristics than the samples based on the semiconductor/insulator combination.

Py and Au wires are fabricated in a two-step lift-off process using optical lithography and electron-beam evaporation (see Figure 6.1). Two pairs of closely spaced 50 nm thick and 2 µm wide Au wires are deposited on top of a single 22 nm thick Py wire of variable width ($w_{\mathrm{Py}} = 20$, 10 or 4 µm), forming four identical crosses. In order to keep the Py/Au interfaces clean, the Py surface is treated by a gentle ion milling step in the deposition chamber prior to the deposition of the Au wires. Figure 6.1 shows scanning electron microscope (SEM) images of a typical sample with $w_{\mathrm{Py}} = 20\,\mu\mathrm{m}$, illustrating the positioning and the lateral dimensions of the wires at their intersection points. The spacing between the Au wires is 5 µm and 11 µm for the outer pairs and the inner pair, respectively. All device dimensions are chosen in such a way that a focused laser beam with a diameter of about 2.5 µm can resolve the structure. This allows us to generate well-defined lateral and perpendicular temperature gradients at arbitrary positions.

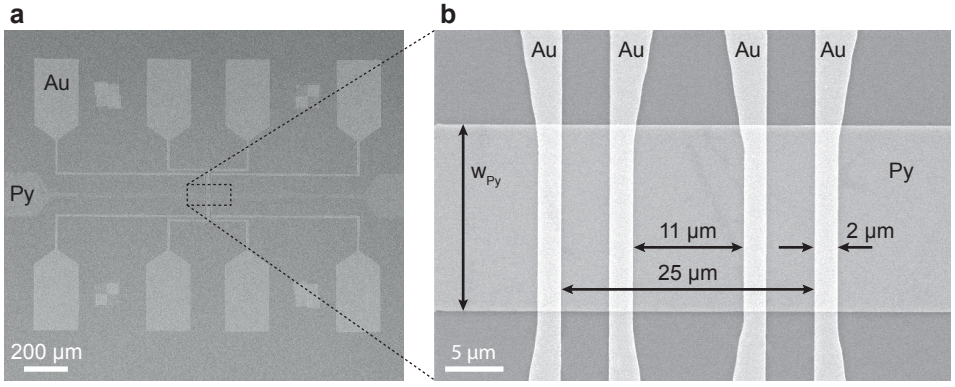

Figure 6.1 | Sample geometry for thermovoltage and EDFMR measurements. Scanning electron microscope (SEM) images showing (a) arrangement of the Au and Py bonding pads. (b) Close up of central region of a sample with $w_{Py} = 20\,\mu m$, showing four identical crossing points between the Py (22 nm thick) wire and the Au (50 nm thick) wires.

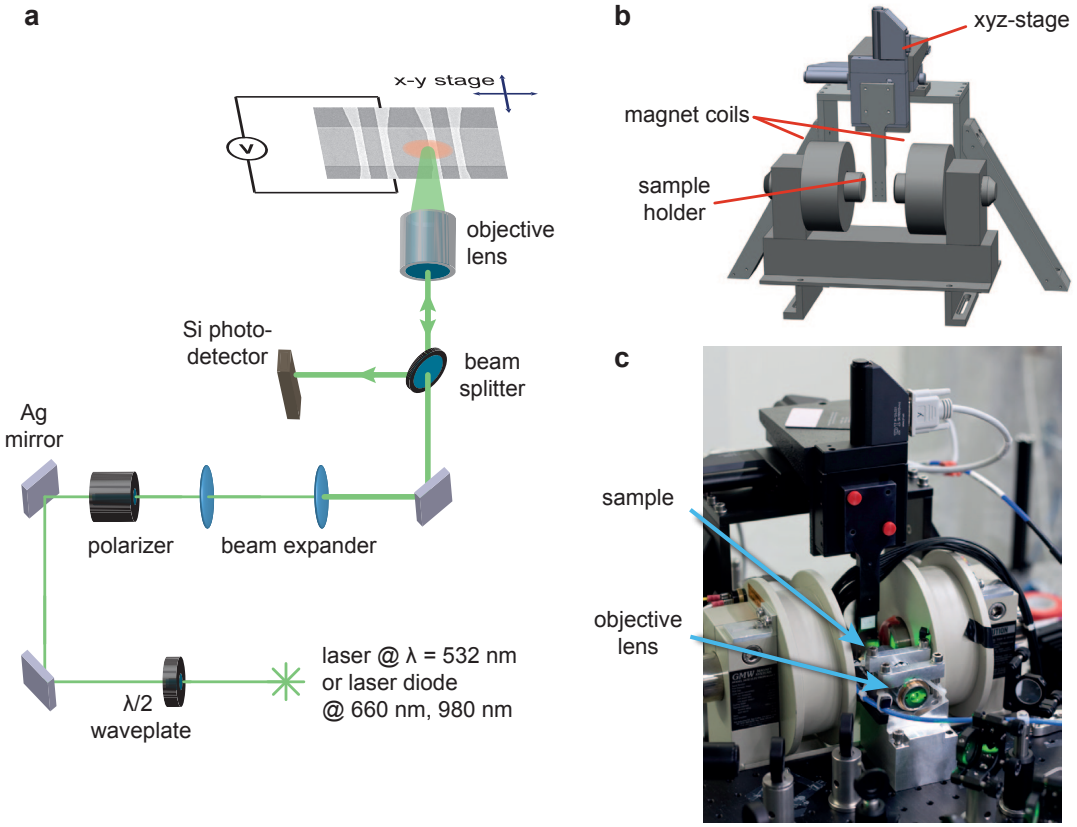

Figure 6.2 | Laser setup and sample holder for laser-heating experiments. (a) Schematic illustration of beam path with optical components and sample connected to multimeter for measurement of laser-induced voltage. (b) 3D-isometric view of custom built magnet system and movable sample holder, (c) photo of sample holder positioned between the pole faces of the magnet with the laser beam focused on the sample.

6.2 Laser-induced heating

6.2.1 Measurement setup

The measurement setup for the laser-induced heating experiments is presented in Figure 6.2. Three different laser sources are employed to investigate wavelength-dependent effects: A diode-pumped solid state (DSPP) laser with wavelength $\lambda = 532\,\text{nm}$ (Laser Quantum Excel, $P_{\text{max}} = 1.5\,\text{W}$), a laser diode with $\lambda = 660\,\text{nm}$ (opnext HL6545MG, $P_{\text{max}} = 120\,\text{mW}$) and a second laser diode with $\lambda = 980\,\text{nm}$ (Thorlabs L980P010, $P_{\text{max}} = 10\,\text{mW}$). While the laser diodes require an aspherical collimation lens to generate a collimated beam, the DSPP laser directly generates a collimated beam with radius $r = 1.5\,\text{mm}$. As shown in Figure 6.2(a), first the laser beam passes a variable attenuator, formed by a $\lambda/2$ waveplate and a polarizer. The beam intensity can be changed by rotating the waveplate and keeping the polarizer fixed (set to p-polarization in all experiments). Next, the beam diameter is adapted to the size of the entrance aperture of the objective lens to improve its focusing performance. We use a 20× infinity-corrected long working distance objective from Mitutoyo to focus the laser beam to a spot size of down to 2.5 µm (see Section 6.2.2). For the reflectivity measurements a beam splitter deflects a small part (~ 3 %) of the light reflected from the sample surface to a Si photodetector.

The sample is glued and wire bonded to a ceramic leadless chip carrier (LCC, 48 pin layout), which can be inserted into an appropriate fixture on the lower end of the sample holder (see Figure 6.2(b,c)). The sample holder provides 11 single-ended electrical connections to the sample (without a common ground point on the sample to avoid ground loops). 10 of these connections are used to connect the four Au wires as well as the Py wire from both ends. In order to reduce the risk of electrostatic discharges through the sample, the electrical contact to the measurement equipment is established via a custom-made grounding box. High-resolution voltage measurements are performed using a Keithley 2182 nanovoltmeter or a SR830 lock-in amplifier. A Keithley 6221 current source, a Keithley 2401 source meter and a Keithley 2000 multimeter complement the measurement equipment for reflectivity and magnetoresistance measurements.

Using a stack of three translation stages (travel range 25 mm, 100 nm resolution) the laser beam can be focused (z-axis) and positioned (x-y plane) on the sample. This allows for simultaneous position-dependent measurements of the reflectivity and laser-induced voltage signals. In this way we can record line scans and acquire 2D intensity maps (see Chapter 7).

An in-plane magnetic field oriented perpendicular to the incident laser beam is generated by a water-cooled magnet system (GMW, model 3470) driven by a KEPCO BOP power supply. In the configuration used for most of the experiments, (i.e. gap between the poles 45 mm, diameter of the pole faces 40 mm) the maximum field reaches a value of ~ 220 mT at the center of the gap. In order to avoid any remanence-induced measurement errors, the magnetic field is continuously monitored using a Hall sensor mounted on one of the pole faces.

Table 6.1 | Refractive index $\tilde{n} = n + i\kappa$, reflectivity R and decay constant α^{-1} (inverse absorption coefficient) of Au and Py for normal incidence at $\lambda_{\text{Laser}} = 532\,\text{nm}$ and 660 nm (refractive index data taken from [175, 176]).

λ	metal	n	κ	R [%]	α^{-1} [nm]
532 nm	Au	0.467	2.408	76.5	17.6
	Py	1.72	2.97	58	14.3
660 nm	Au	0.165	3.283	94.6	16
	Py	1.98	3.23	59	16.1

6.2.2 Heating profile and temperature distribution

The laser-generated temperature distribution in the sample is mainly defined by the absorbed power and the diameter and the shape of the incident beam. The incident laser power is measured using a thermopile power meter positioned between the beam expander and the last mirror. The losses between this point in the beam path and the sample position are taken into account in the data analysis ($\sim 22\,\%$ for $\lambda = 532\,\text{nm}$ and $\sim 19\,\%$ for $\lambda = 660\,\text{nm}$). The absorption also depends significantly on the optical properties of the irradiated part of the sample. The reflectivity of an air-metal surface is given by $R = \frac{(n-1)^2+\kappa^2}{(n+1)^2+\kappa^2}$. n and κ denote the (generally wavelength-dependent) refractive index and extinction coefficient, respectively, which define the complex refractive index $\tilde{n} = n + i\kappa$. As metals exhibit a large κ for visible light, the majority of the incident intensity is reflected. The fraction that passes the surface, however, is absorbed within a very short distance. The decay of the optical intensity within a metal is described by the *Beer–Lambert law* $I(z) = I_0 e^{(z/\alpha)}$, where z is the distance the light has traveled within the material, I_0 is the intensity of the incident light and $\alpha = 4\pi\kappa/\lambda$ is the absorption coefficient. A metallic film of a few tens of nm in thickness is therefore sufficient to absorb most of the incident power. Absorption in the substrate is either zero (in case of MgO due to its wide bandgap) or very weak (in case of SiO_2/GaAs) and can therefore be neglected. Table 6.1 summarizes the optical properties of the two metals used in this study.

To confirm the theoretically derived values, the reflectivity was also determined experimentally. For instance for $\lambda_{\text{Laser}} = 532\,\text{nm}$ at an angle of incidence of $\beta \approx 30°$ the reflectivity was found to be 72 %, which agrees within a few percent with the theoretical prediction for that angle (73.2 %). The deviation can be attributed to diffuse reflection from the sample surface, decreasing the amount of reflected light collected by the objective lens. As the reflectivity for normal incidence could not be precisely measured, any estimates of the absorbed power will be based on the theoretical values for reflectivity and absorption given in Table 6.1.

The shape and the size of the focused laser spot on the sample is analyzed by measuring the reflected intensity while scanning the laser spot across a sharp edge between two materials of drastically different reflectivity (see Figure 6.3(b)). Using this method, we obtain the integral of the transverse intensity profile of the beam along the scan direction. Laser beams often have a

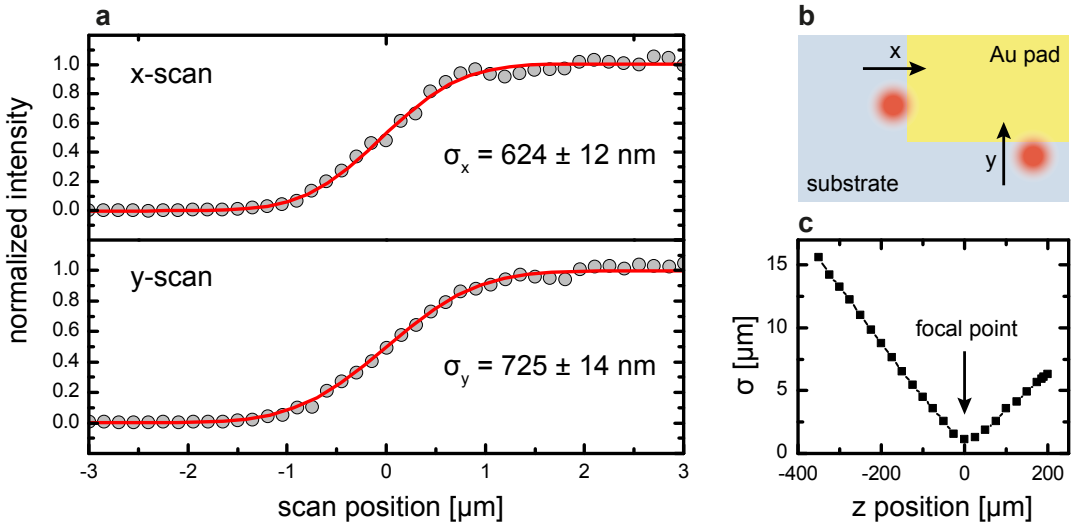

Figure 6.3 | Laser spot size measurement. (b) Schematic illustration of laser spot movement across horizontal and vertical edge of Au pad (from low to high reflectivity). (a) Normalized reflected intensity (gray circles) and error function fit (red line) for a typical scan along x-direction (upper panel) and y-direction (lower panel) as a function of position (0 µm = laser spot center positioned on edge). The data is offset by the reflectivity signal from the substrate. (c) Measured standard deviation σ as a function of out-of-focus position z (at $z = 0$ µm the sample surface coincides with the focal plane).

Gaussian intensity profile with

$$I(r) = \frac{1}{\sigma\sqrt{2\pi}} e^{-\frac{1}{2}\left(\frac{r}{\sigma}\right)^2},$$

where r is the distance from the beam center and σ is the standard deviation. Integrating such a Gaussian yields the error function.

Figure 6.3(a) shows the measurement data for two scans across the (horizontal and vertical) edges of an Au contact pad on an MgO substrate. In both cases we observe very good agreement with the fitted error function (red curve), indicating that the laser beam exhibits a Gaussian shape. From the fitted error functions we obtain the standard deviation $\sigma_{x/y}$ of the Gaussian distribution describing the beam profile along x and y. The beam diameter d is defined by the circumference where the intensity drops to $I_0 \cdot 1/e^2$, where I_0 denotes the peak intensity. This corresponds to a beam diameter of $d = 4\sigma$. Hence, we can conclude that the laser spot analyzed in Figure 6.3(a) has a slightly elliptic shape with $d_x \approx 2.5$ µm and $d_y \approx 2.9$ µm.

Figure 6.3(c) shows the standard deviation σ, obtained as described above, as a function of z-position of the sample holder. This results allows us to adjust the spot size by moving the sample slightly out of focus. By combining this method with the precise positioning based on reflectivity maps (see Chapter 7) we can generate very well-defined in-plane temperature

gradients using the large intrinsic intensity gradient of the laser spot. This is exploited in Chapter 8 for the investigation of FMR in temperature gradients.

We numerically simulate the laser-induced temperature distributions by solving the stationary heat equation (Poisson's equation: $\lambda\nabla^2 T = q$ with thermal conductivity λ, temperature T and heat source density q) using the finite element method (FEM) simulation package COMSOL Multiphysics[1]. In the example shown in Figure 6.4, the sample geometry is modeled using the parameters given in Section 6.1. We find that a $400 \times 400 \times 200\,\mu m^3$ large substrate block is sufficient to model the heat transfer characteristics of the entire substrate. The bottom face of the substrate is in contact with a thermal bath at room temperature $T = 293.15\,K$, all remaining boundaries are thermally insulating. We use a tetrahedral mesh, where the cell size is adapted to the geometry and the occurrence of temperature gradients, i.e. the mesh is strongly refined in the thin metal layers and particularly around the laser spot. Table 6.2 summarizes the material parameters employed in the simulation.

Another crucial simulation parameter is the interface thermal conductance between Py and the substrate (MgO in Figure 6.4) as it determines how efficiently the heat diffuses away from the heated Py/Au wires. In contrast to lattice-matched interfaces that have been shown to reach up to $700\,MW\,m^{-2}\,K^{-1}$ [177], in most cases there is a large mismatch in both, the lattice constant and the Debye temperature, leading to lower interface conductance values of the order of $100\,MW\,m^{-2}\,K^{-1}$or less [178, 179]. Given that the conductance depends not only on the material parameters but also on the growth conditions, its precise value can only be determined experimentally. As such a study would go beyond the scope of this work and as we are mainly interested in qualitative comparisons between experiment and numerical simulation, we use an approximated value of $100\,MW\,m^{-2}\,K^{-1}$. The interface conductance is much less crucial for the samples grown on a GaAs/SiO_2 substrate. In this case the thermal resistance is dominated by the 300 nm thick SiO_2 layer due to its low heat conductivity (a 300 nm thick SiO_2 layer corresponds to an interface conductance of only $4.7\,MW\,m^{-2}\,K^{-1}$). The interface conductance of the SiO_2/Py interface is therefore not taken into account in the simulations.

Figure 6.4(a) shows the surface temperature of the structure when heating the center of the Py wire with a 4 µm wide ($\sigma = 1\,\mu m$) laser spot with $P = 2\,mW$ incident power. Due to the low thickness of the Py film the absorbed power amounts to about $\sim 1.6\,mW$ (neglecting further reflections of the laser beam inside the metal). It is striking that the resulting temperature rise remains locally confined instead of spreading out into the Au leads. Figure 6.4(b) illustrates that the temperature profile (black line) resembles very closely the Gaussian intensity profile (or heating power profile) of the laser beam (dashed line), indicating that most of the heat diffuses directly into the substrate. The lower panel in Figure 6.4(b) shows that the lateral temperature gradient reaches extremely large values of almost $10\,K\mu m^{-1}$ due to the large slope of the heating profile.

[1] COMSOL AB, Stockholm, www.comsol.com

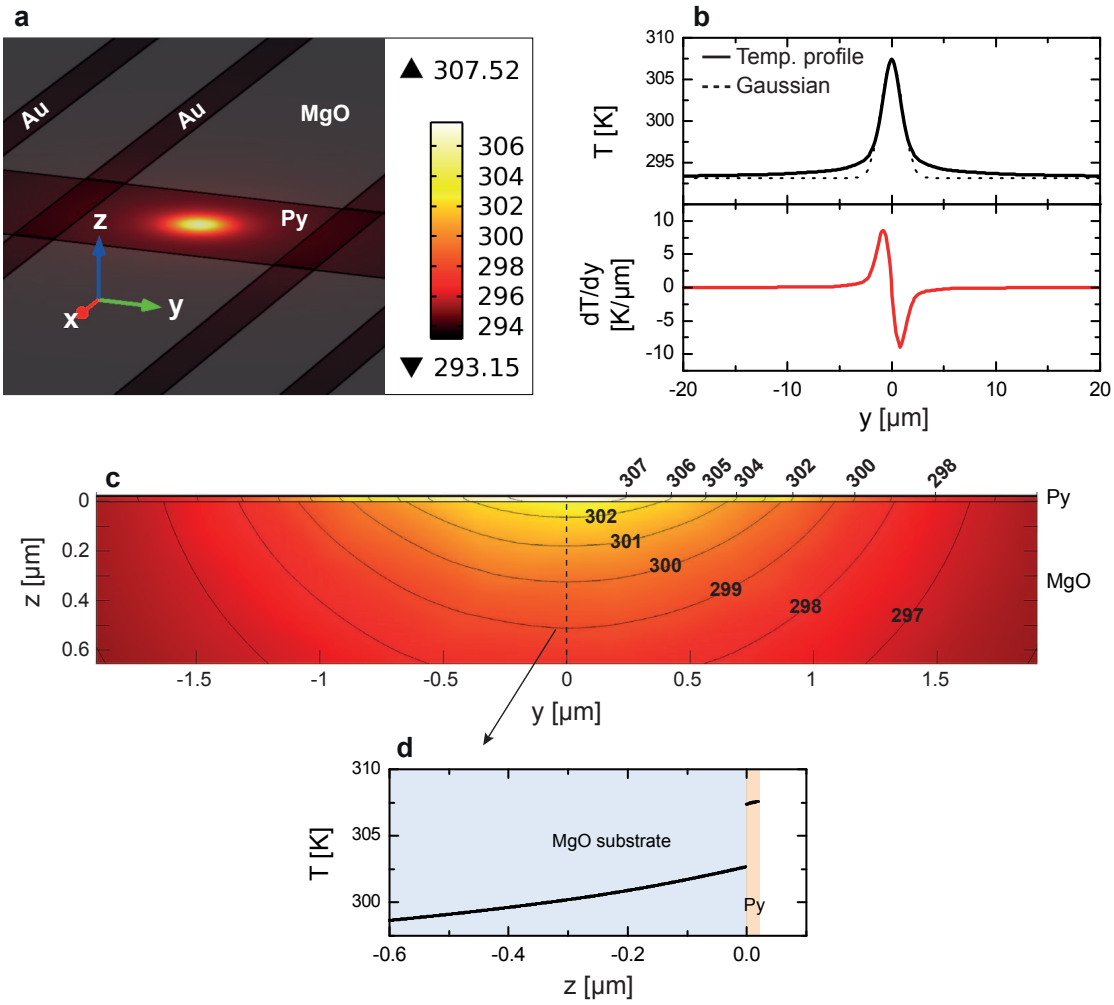

Figure 6.4 | FEM simulation of laser heating and resulting temperature distribution. (a) Surface temperature of a 10 µm wide Py wire with four traversing Au wires on an MgO substrate (for details on the geometry see Section 6.2.1), absorbed laser power $P_{abs} \approx 1.6\,mW$ with $\sigma_{x,y} = 1\,\mu m$. (b) Upper panel: Temperature profile within Py wire (black curve) and Gaussian intensity profile of laser beam (dashed curve) along y-axis ($x = 0$). (b) Lower panel: Temperature gradient dT/dy along the same line. (c) Temperature distribution in z-y-plane down to a depth of 600 nm showing heat diffusion away from the laser spot into the substrate. Black lines are isothermals labeled with the corresponding temperature in K. (d) Temperature profile along z-axis at spot center. The discontinuity of the temperature arises from the interfacial thermal resistance between Py and MgO.

Table 6.2 | Material parameters. Heat capacity C_p, thermal conductivity λ, density ρ, Seebeck coefficient S and conductivity σ used for the simulation of laser-induced temperature distribution and the Seebeck voltage (values taken from the material database in COMSOL Multiphysics and [140, 180] for $T = 0\,\mathrm{K}$).

Material	C_p [$\mathrm{J\,kg^{-1}\,K^{-1}}$]	λ [$\mathrm{W\,m^{-1}\,K^{-1}}$]	ρ [$10^3\,\mathrm{kg\,m^{-3}}$]	S [$\mu\mathrm{V\,K^{-1}}$]	σ [$10^6\,\mathrm{S\,m^{-1}}$]
Py	445	30	8.74	-20	2.9
Au	129	317	19.3	1.7	18
MgO	960	45	3.58	–	–
SiO_2	730	1.4	2.2	–	–
GaAs	550	33	5.316	–	–

The temperature profile in the y-z-plane is illustrated using a cross-section of the substrate at the position of the laser spot shown in Figure 6.4(c). Despite the low thermal interface conductance between Py and MgO, the laser-generated temperature rise spreads almost as quickly into the substrate as along the Py film. The large contact area between the heated region and the substrate more than compensates for the interface resistance. In addition to that, MgO conducts heat 50 % better than Py, turning the substrate into an efficient heat sink. It is exactly for this reason that spurious temperature gradients are difficult to avoid in most spin Seebeck experiments (see discussion in Section 5.2.2).

Figure 6.4(d) shows the vertical temperature profile along the z-axis at the center of the laser spot down to a depth of 620 nm. As expected from diffusion from a locally confined source into an open volume, the temperature decays rapidly with increasing distance from the heat source. The discontinuity at the interface between Py and MgO arises from the significant thermal interface resistance. This result highlights the large impact of the thermal interface conductance on the temperature distribution. It therefore cannot be neglected when estimating (out-of-plane) temperature gradients in thin film structures.

6.3 Ferromagnetic resonance

6.3.1 Microwave excitation using local resonators

For the investigation of ferromagnetic resonance (FMR) in temperature gradients we extend the laser-heating setup (see Section 6.2.1) by a microwave resonator that generates a magnetic RF-field h_{rf} at the position of the sample. Due to bandwidth limitations of the sample holder, lithographically defined strip lines cannot be used. Placing a coplanar waveguide resonator on top of the sample is also not considered an option as that would block the laser beam path. We therefore employ a local microwave resonator[2], as schematically illustrated in Figure 6.5(a). It consists of a small printed circuit board (PCB) with a thin loop (diameter $d \approx 50\,\mu\mathrm{m}$) at its end. Capacitors on the PCB form a resonating circuit with the loop and match the impedance

[2] Manufactured by: ez SQUID Mess- und Analysegeräte, Sinn, Germany

between the SMA cable/connector and the circuit. The relative orientation of the resonator, lens and sample is illustrated in Figure 6.5(a) and in a photo of the actual measurement setup in Figure 6.5(b). The resonator is positioned and oriented such that the microwave current fed through the loop generates a magnetic RF-field that is perpendicular to the DC magnetic field H at the position of the laser spot. The typical distance between the laser spot and the tip of the resonator is about 1 mm. Due to the small diameter of the loop, the generated field is inhomogeneous and decays rapidly with increasing distance from the tip of the resonator. It is therefore essential to position the resonator precisely and as close as possible to the laser spot on the sample.

Figure 6.5(c) shows a simplified circuit diagram of the microwave setup. The resonator is driven by a R&S SGS100A microwave generator ($f_{\text{out}} = 0.1 - 12.7\,\text{GHz}$) with an output power of up to 25 dBm. For more sensitive measurements with a lock-in amplifier, the signal can be modulated using a microwave switch driven by a function generator. For some of the measurements we use a broadband microwave amplifier (Minicircuits ZVE-3W-83+) to attain a maximum output power of 35 dBm ($\approx 3.2\,\text{W}$). After amplification, the signal is passed through a circulator, which protects the microwave source from any reflected power. At the same time the circulator allows us to measure the power reflected by the resonator using a zero bias Schottky detector (Narda 4503A-03).

Two different resonator models with $f_{\text{res}} \approx 4.3\,\text{GHz}$ and $f_{\text{res}} \approx 7.25\,\text{GHz}$ are employed for the FMR measurements presented in Chapter 8. The tuning, i.e. finding the resonance frequency f_{res} of the resonator, can be performed either based on the reflected power (measured by the Schottky diode) or based on the DC voltage induced in the structure (measured via the Au wires by a Nanovoltmeter). Figure 6.6 shows typical tuning curves of this kind.

The blue curve in Figure 6.6 shows the reflected power as a function of frequency. At around 7.2 GHz it reaches its absolute minimum. This means that the amount of power that is absorbed and emitted as microwave radiation is maximum at this frequency. Fitting a Lorentz function to the curve yields $f_{\text{res}} \approx 7.2\,\text{GHz}$ with $\Delta f_{\text{FWHM}} = 311 \pm 10\,\text{MHz}$ and a resonance quality factor of $Q = f_{\text{res}}/\Delta f_{\text{FWHM}} \approx 23$. Both the Q-factor as well as the position of the peak depend sensitively on the positioning of the resonator. Any movement can change the resonator's dielectric environment and hence the resonance condition. Irrespective of the precise position, both resonators are found to consistently exhibit low Q-factors between about 20 and 30.

The black curve in Figure 6.6 shows the DC voltage arising from the FMR-induced AMR voltage (see Section 5.3.2). As expected, the largest signal appears at the resonance frequency, i.e. when the excitation field h_{rf} reaches its maximum. Despite the strongly distorted shape of the resonance curve, the resonance width and peak position obtained using a Lorentian fit ($f_{\text{res}} \approx 7.25\,\text{GHz}$ with $\Delta f_{\text{FWHM}} = 327 \pm 7\,\text{MHz}$) agree well with the parameters obtained based on the reflected power. The tuning of the resonator is verified upon each change of either the position of the sample or the microwave power level. Once the resonance frequency is known, FMR can be measured using the two methods presented in the following.

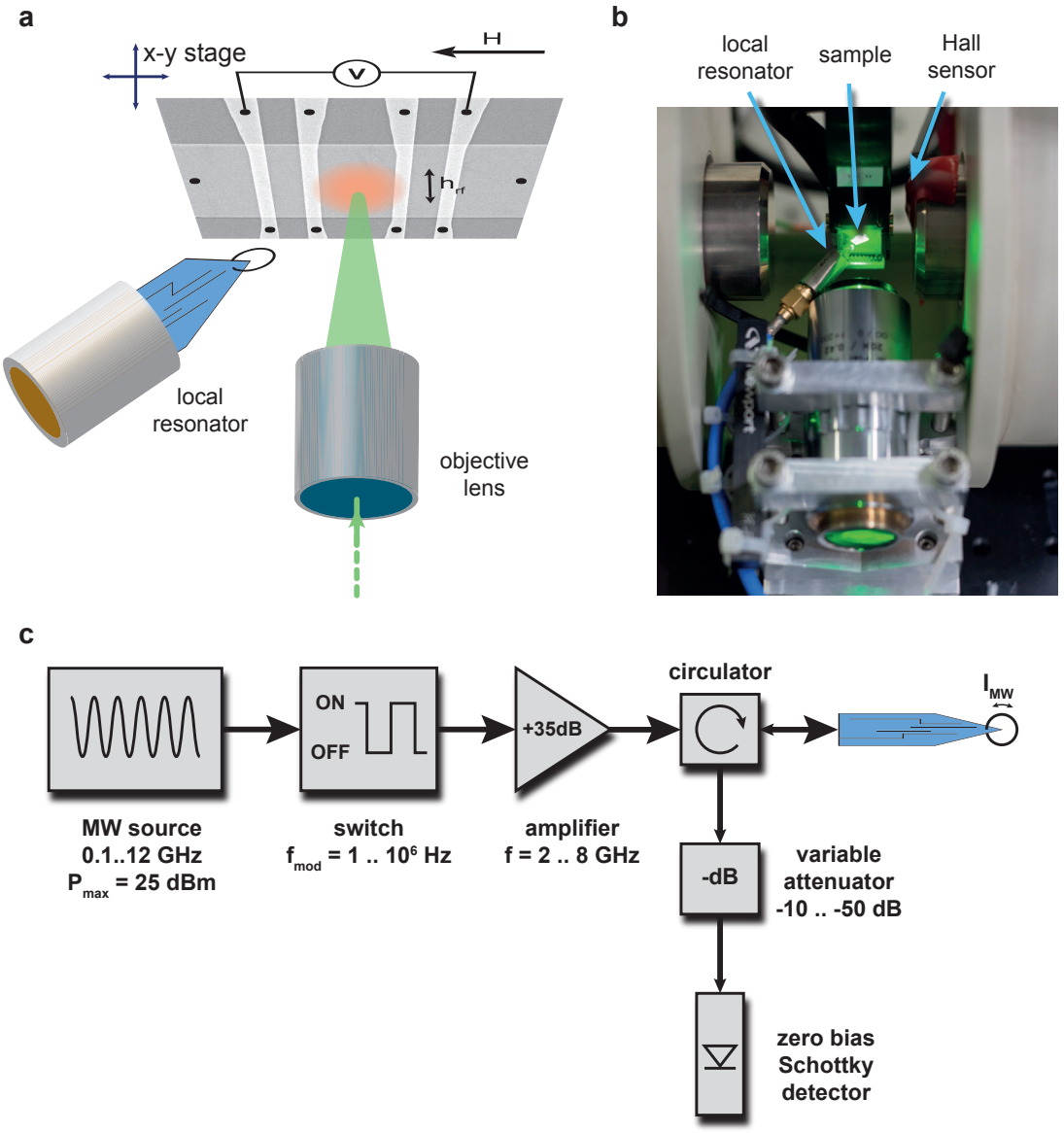

Figure 6.5 | Setup for inductive and electrical detection of FMR in laser-heated microstructures. Schematic illustration (a) and photo (b) of mounted sample with focused laser beam and local resonator positioned close to the laser spot. (c) Circuit diagram of microwave setup.

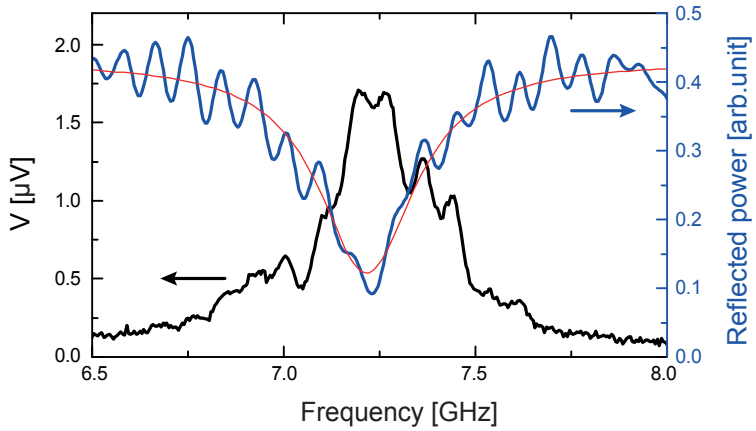

Figure 6.6 | Tuning curves of a local resonator with nominal resonance frequency $f_{\mathrm{res}} \approx 7.25\,\mathrm{GHz}$ at output power P $\approx 15\,\mathrm{dBm}$. Blue line: Power reflected by the resonator, reaching a minimum on resonance. Red line: Lorentz function fitted to the reflected power with parameters $f_{\mathrm{res}} \approx 7.2\,\mathrm{GHz}$, $\Delta f_{\mathrm{FWHM}} = 311 \pm 10\,\mathrm{MHz}$, corresponding to a quality factor of $Q \approx 23$. Black line: FMR-induced AMR voltage, measured between inner Au wire pair (see Figure 6.1).

6.3.2 Inductive detection with field modulation

When the applied field H_0 and the excitation frequency f_{res} meet the resonance condition for FMR, the microwave power absorbed by the sample (or χ'', see Section 5.3.2) increases significantly, which in turn decreases the power reflected by the resonator. This opens the possibility of reconstructing the FMR line shape by measuring the variation of the reflected power when sweeping the DC field H_0 through the resonance condition. The sensitivity of this measurement can be drastically enhanced using lock-in detection. Hence, in the present setup (see Figure 6.7(a)) we employ the field modulation technique, where the applied magnetic field is modulated by a small amplitude sine wave. We keep the peak-to-peak field amplitude $H_{\mathrm{m,p-p}}$ below 10 % of the line width to avoid distortions to the line shape. Instead of using separate modulation coils, we modulate the field generated by the main magnet by sending an appropriately modulated programming voltage from a waveform generator to the magnet power supply. The power supply then translates this voltage into a modulated current fed through the magnet coils, generating a sinusoidal magnetic field of amplitude H_{m} and frequency f_{m} with DC offset H_0. The signal obtained from the lock-in measurement is proportional to the derivative of the absorption with respect to the DC field, $\mathrm{d}\chi''/\mathrm{d}H$. Most of the measurements presented in this work are carried out at an integration time constant of $t_{\mathrm{int}} = 300\,\mathrm{ms}$ or 1 s.

Figure 6.7(b) shows the result of such a measurement performed on a 22 nm thick film of Py (deposited by electron-beam evaporation) at microwave frequency $f_{\mathrm{MW}} = 7.185\,\mathrm{GHz}$ and output power $P = 20\,\mathrm{dBm}$ (MW amplifier and MW switch (see Figure 6.5) inactive). The purpose of this test measurement is to investigate the reliability of the field-modulation FMR technique using local resonators. The upper panel of the figure depicts $\mathrm{d}\chi''/\mathrm{d}H$ for three different amplitudes of the modulation field $H_{\mathrm{m,p-p}}$ at fixed modulation frequency $f_{\mathrm{m}} =$

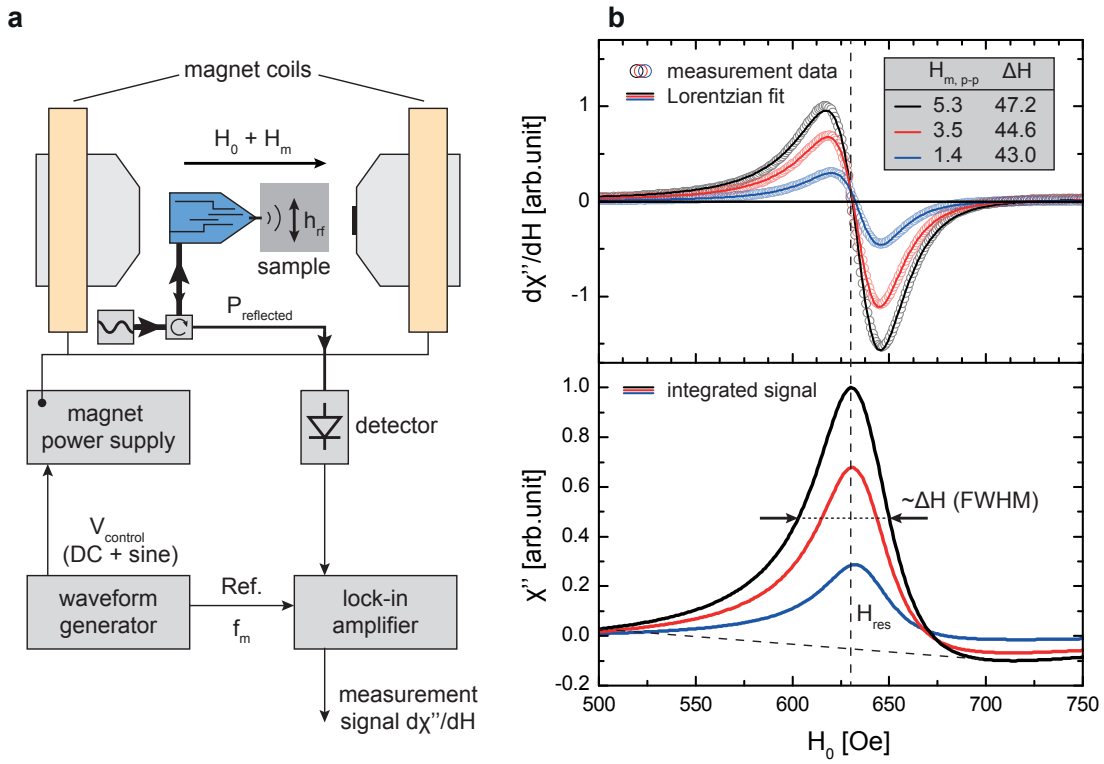

Figure 6.7 | Inductively detected FMR of an unpatterned 22 nm thick Py film using field modulation at $f_m = 17.234\,\text{Hz}$, $f_{MW} = 7.185\,\text{GHz}$ and $P = 20\,\text{dBm}$. (a) Simplified sketch of field modulation measurement setup. (b) Upper panel: $d\chi''/dH$ (open circles) as a function of DC magnetic field H_0 for three different modulation field amplitudes H_m. Solid lines are best fits based on an asymmetric Lorentzian. Extracted line widths ΔH are shown in the upper right corner (all values given in *Oe*). (b) Lower panel: Absorption χ'' as a function of applied DC field calculated from the data shown in the upper panel, reproducing the expected Lorentzian line shape. Dashed lines illustrate the baseline, the resonance field $H_{res} = 636\,\text{Oe}$ and the line width for $H_m = 5.3\,\text{Oe}$.

17.234 Hz. H_0 and $H_{m,p-p}$ are measured using an appropriately calibrated Hall effect sensor attached to one of the magnet poles. As expected, we obtain the derivative of a Lorentzian line shape (measurement data: open circles), which is confirmed by fitting a function (solid lines in Figure 6.7(b)) of the form

$$\frac{d\chi''}{dH_0} \propto \frac{d}{dH_0}\left(\frac{\Delta H + D(H_0 - H_{res})}{(H_0 - H_{res})^2 + \Delta H^2}\right)$$

to the data, where ΔH is the line width (FWHM) and H_{res} denotes the resonance field. This is an asymmetric Lorentzian line including both absorption and dispersion, where D denotes the ratio between dispersion and absorption (for details see Section 5.3.2). Further confirmation is provided by the integrated signals shown in the lower panel.

We extract a resonance field of $H_{res} = 636\,\text{Oe}$ and the resonance widths ΔH (FWHM) shown in Figure 6.7(b) from the fit. The observed linewidth of $\Delta H \approx 43\,\text{Oe}$ is slightly higher than the

value derived from Gilbert damping in Py at this frequency ($\Delta H_G \approx 41$ Oe, see Section 5.3.2). We attribute the discrepancy to inhomogeneous broadening. It is well-known that roughness of the sample surface and variations of the demagnetizing field across the sample can increase ΔH significantly [181, 182]. As expected, a large modulation amplitude $H_{m,p-p}$ leads to a larger detected signal. However, at 5.3 Oe the modulation amplitude starts to distort the line shape, which appears as a considerable increase of the linewidth. The measurements presented in Chapter 8 are therefore carried out at the lowest possible $H_{m,p-p}$ (usually around 2 Oe) that provides a sufficient signal-to-noise ratio without distorting the linewidth.

Apart from the modulation-induced broadening, we note that the resonance peak is slightly asymmetric, which is likely due to the interplay of inhomogeneities in both the excitation field and the effective field (see above for the latter). h_{rf} is particularly inhomogeneous as the local resonator generates a strongly confined field. In addition, different parts of the sample contribute to the signal with different phases. As the employed detection scheme is phase-insensitive, this may enhance the apparent dispersive character of the resonance peak.

Despite these effects, the measurements clearly demonstrate that we are able to obtain clean and reproducible FMR spectra using the local resonator. The inductive detection scheme will be employed in Chapter 8 to study FMR in temperature gradients.

6.3.3 Local excitation and electrical detection

In order to verify the suitability of the measurement setup for electrical detection of FMR (EDFMR), we perform a set of such electrical measurements on the same Py film as the one used in the previous section. As illustrated in Figure 6.8(a), in the EDFMR setup the lock-in amplifier directly measures the induced voltage between two points on the film surface at the field modulation frequency. The sample is contacted using Au wires glued to the surface using silver glue. ϕ_0 is the angle between the RF field direction and the axis along which the induced voltage is measured (i.e. the line connecting the contact points).

The upper panel of Figure 6.8(b) shows EDFMR data for two different angles ϕ_0. As described in Section 6.3.2, the experimental data (open circles) is fitted using the derivative of an asymmetric Lorentzian (solid lines). We obtain a resonance width of $\Delta H \approx 57$ Oe for $\phi_0 = 90°$ and $\Delta H \approx 51.2$ Oe for $\phi_0 = 45°$, similar to the values measured by inductive detection for the same modulation amplitude. We also observe a shift in resonance field H_{res} from 635 Oe to 644 Oe. As discussed in Section 5.3.4, the FMR-induced AMR voltage signal is expected to yield the same values for the linewidth and the resonance field as a standard FMR measurement. In particular, according to Equation (5.10) neither the width nor the resonance field depend on the orientation of the sample (ϕ_0). We therefore ascribe the observed angle-dependence to magnetic anisotropy, possibly due to slightly off-stochiometric Py or a partly antiferromagnetic oxide layer on top of the film. It should also be noted that the sample had to be repositioned on the chip carrier in order to change the angle ϕ_0. This may have caused a small difference in field geometry at the sample position (H_0 or h_{rf}), leading to a shift and/or narrowing of the

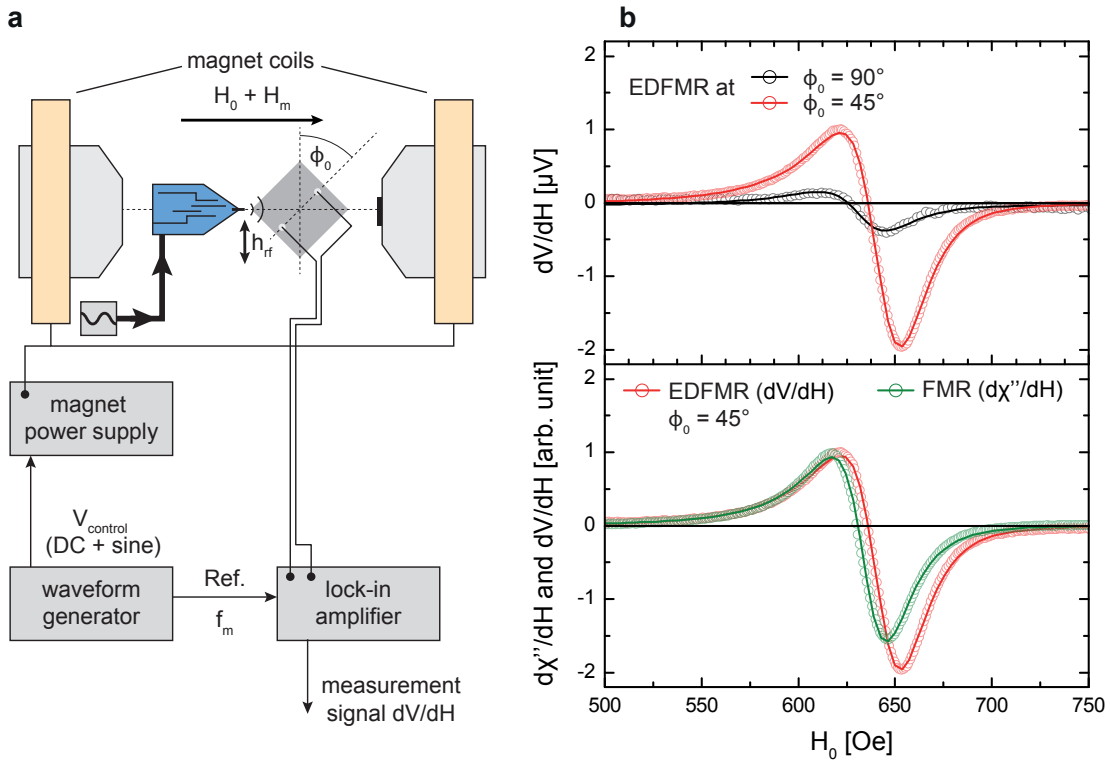

Figure 6.8 | Electrically detected FMR of an unpatterned 22 nm thick Py film using field modulation at $f_{\mathrm{mod}} = 17.234\,\mathrm{Hz}$, modulation field amplitude $H_{\mathrm{m}} \approx 5.3\,\mathrm{Oe}$, $f_{\mathrm{MW}} = 7.185\,\mathrm{GHz}$ and $P = 25\,\mathrm{dBm}$. (a) Simplified sketch of field modulation measurement setup modified for electrical detection (see Figure 6.7(a)). (b) Upper panel: EDFMR signal $\mathrm{d}V/\mathrm{d}H$ (open circles) as a function of H_0 for $\phi_0 = 90°$ and 45°. Solid lines are best fits based on asymmetric Lorentzian functions (see Section 6.3.2). (b) Lower panel: Comparison of inductively detected FMR and EDFMR for the same sample (curves are normalized to the maximum of the positive peak).

resonance.

The lower panel of Figure 6.8(b) shows a comparison of normalized FMR traces obtained from inductive and electrical detection (red curve taken from upper panel, green curve taken from Figure 6.7(b), $H_{\mathrm{m}} \approx 5.3\,\mathrm{Oe}$). Apart from the slight changes discussed above, we observe very good agreement between the two different measurement techniques. Our investigation of FMR in microstructures with large temperature gradients will be based partly on this electrical detection scheme as it allows for a strictly local detection when employing micro or nanopatterned magnetic thin films. This is in stark contrast to the inductive detection technique, where the probed surface area coincides with the area excited by the resonator, corresponding to an area of hundreds of μm in diameter.

7 Laser-induced voltages in magnetic microstructures

Based on the experimental techniques presented in the previous chapter we will now investigate the voltage signals generated upon laser irradiation. The first part of this chapter provides an overview of the observed effects and a detailed description of how they can be identified and separated from each other. In addition, the influence of the substrate material and the laser wavelength is addressed. In the second part we use the anomalous Nernst effect (ANE) to perform thermoelectrical magnetic imaging of Py wires. In particular, we examine the magnetization reversal and the role of laser-induced heating in the magnetic switching process.

7.1 Identification and separation of laser-induced voltage signals

7.1.1 Seebeck effect in Au/Py structures

As described in Section 6.1, the employed sample structure exhibits four identical points of intersection between the Py wire and the Au wires. Due to the different Seebeck coefficients of Au and Py (see Table 6.2), each of these Au/Py interfaces form a thermocouple with $\Delta S \approx$

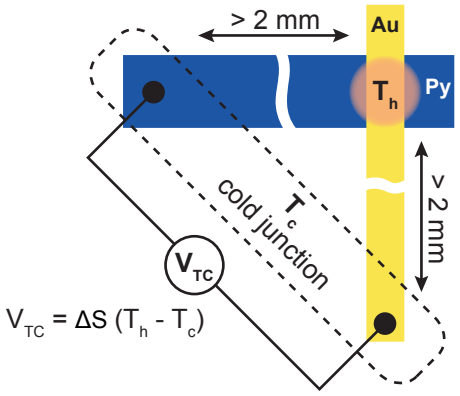

Figure 7.1 | Generation of Seebeck voltage in a Au/Py thermocouple

$21.7\,\mu V\,K^{-1}$ (at room temperature). As illustrated in Figure 7.1, their common 'cold junction' temperature T_c is defined by the substrate temperature far away from the position of the laser spot where the bonding pads are connected to the measurement equipment. Given that the heat diffusion along the wires is negligible (see Section 6.2.2) and that the temperature of the bonding pads remains unaffected by the local laser heating, we assume that T_c corresponds to room temperature (RT $\equiv$ 293.15 K). The voltage measured between one end of the Py wire and one of the Au wires is therefore expected to be a direct measure of the average temperature rise of the Au/Py interface above room temperature.

First, using the reflectivity signal, we verify the accuracy of the scanning technique (see Section 6.2.1) by imaging the sample structure (batch II: Py/Au wires deposited directly on MgO substrate). Then we characterize the laser-induced Seebeck voltages and compare the experimental data to simulation results, as summarized in Figure 7.2.

The upper panels in Figure 7.2(a-c) show reflectivity images obtained from three subsequent measurements of a sample with $w_{\mathrm{Py}} = 10\,\mu$m. All images shown have a size of $30 \times 70\,\mu m^2$ and were recorded with a step size of 500 nm at laser wavelength $\lambda = 660$ nm and laser power $P \approx 8$ mW. Despite the spot size of about $4\sigma \approx 4\,\mu$m, i.e. twice as large as the width of the Au wires, the images clearly reproduce the sample geometry (see Figure 6.1). Consistent with the reflectivity values given in Table 6.1, the Au wires appear brighter than the wide Py wire. The MgO substrate, being transparent for visible wavelengths, reflects almost no light and therefore appears black. These reflectivity images allow us to correlate the position-dependent voltages, depicted as voltage maps in the middle panels of Figure 7.2(a-c), to the structure of the sample. The probed wires as well as the polarity of the connected Nanovoltmeter are indicated by the circuit diagrams in the reflectivity images. The lower panels in Figure 7.2(a-c) show line scans of the measured voltage along the horizontal dashed line shown in the voltage maps. Here, circles (left y-axis) denote the experimental data extracted from the corresponding voltage map and the dashed line (right y-axis) shows the corresponding simulation result for ΔT (see below).

Figure 7.2(a) and (b) shows the results for the voltage measured between the Py wire and two neighboring Au wires. In both cases the detected voltage reaches a minimum (dark blue spot) when the laser beam is positioned on top of the crossing point of the two contacted wires. The signal levels off to zero when the distance between the laser spot and the cross is increased. This behavior strongly suggests that the measured voltage is due to the Seebeck effect and thus depends only on the temperature of the relevant Au/Py interface. Furthermore, as can be seen in both the voltage maps and the line scans, the gradual decay is interrupted when the spot crosses any of the other Au wires. This can be attributed to reduced heating due to the significantly higher reflectivity of Au. The measurements shown were performed at room temperature at zero magnetic field. Control measurements did not show any significant dependence on the applied field (up to ~ 200 mT) or the polarization of the laser light, excluding thermomagnetic effects as the origin of the observed voltage signal.

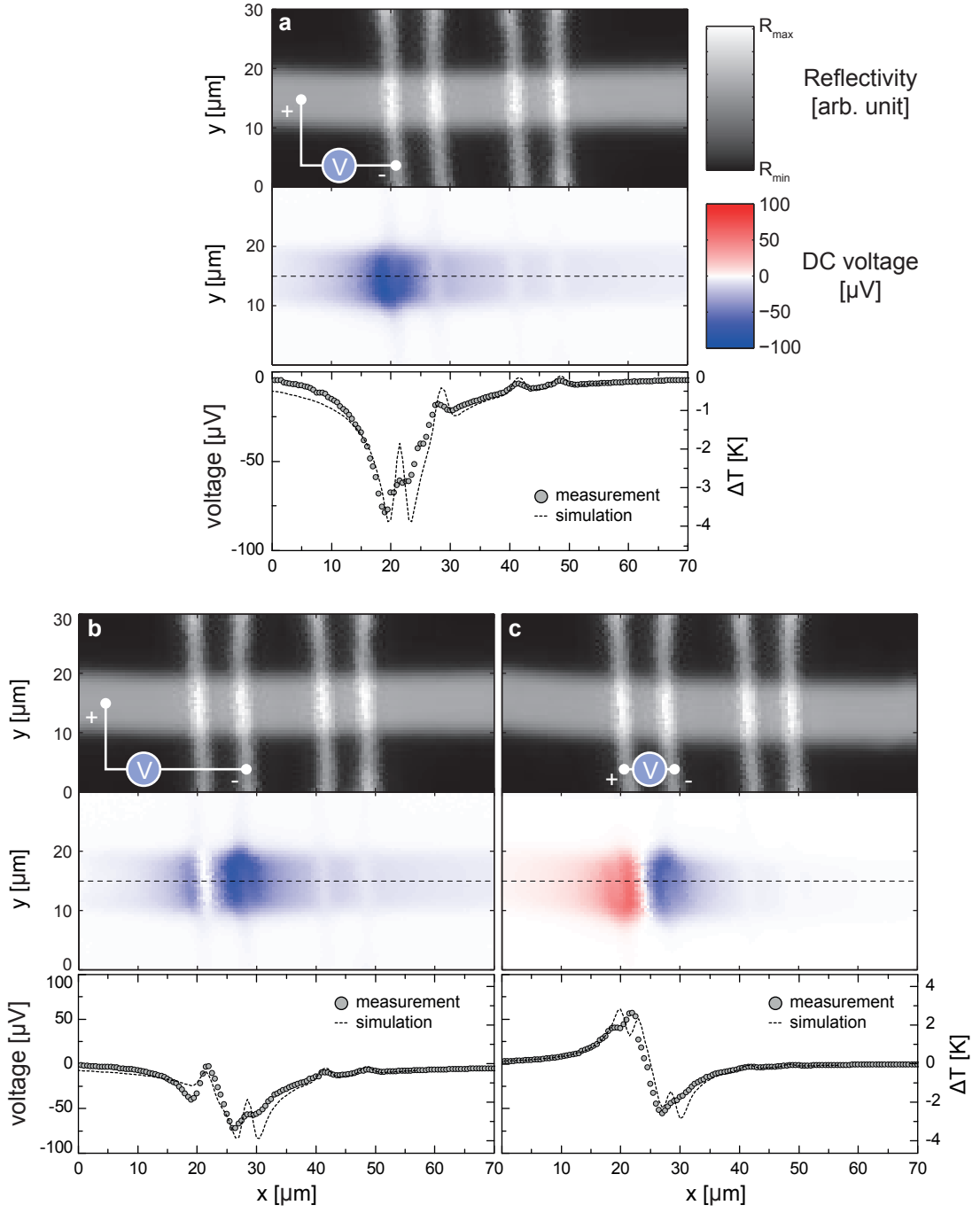

Figure 7.2 | Seebeck voltage generated by laser-heating of Py/Au thermocouples (sample batch II, MgO substrate) and comparison with numerical simulation. (a-c) Reflectivity images (upper panels) and voltage maps (middle panels) obtained by scanning a laser spot of wavelength $\lambda = 660\,\text{nm}$, power $P \approx 8\,\text{mW}$ and spot size $4\sigma \approx 4\,\mu\text{m}$ across the sample surface while simultaneously measuring the reflected intensity and the voltage drop. Colorbars shown in (a) are also valid for (b-c). Circuit diagrams in the reflectivity images indicate wiring and polarity used for voltage maps. Bottom panels show the temperature profiles (circles: experimental data, dashed line: simulation) in the Py wire along the dashed lines shown in the voltage maps.

The lower panels in Figure 7.2(c) show the behavior of the voltage measured between the two Au wires that were connected separately in (a) and (b). In this case, the generated voltage is effectively measured across two oppositely oriented Au/Py interfaces (or two thermocouples of opposite polarity). We call this the 2-thermocouple configuration. As previously, we obtain a negative thermovoltage when the laser spot heats the Au/Py interface to the right, which is connected in the same sense as in (b). In contrast to that, heating the oppositely oriented interface results in a positive voltage of the same magnitude. This sign change further confirms that the observed thermovoltages sensitively depend on the Au/Py interfaces, as expected from the Seebeck effect.

Based on the simulation model presented in Section 6.2.2, we perform numerical simulations of the temperature distribution as a function of laser spot position along the dashed line in the voltage maps. Simulation parameters are adapted according to the used wavelength and laser power. The bottom panels in Figure 7.2(a-b) show the average temperature difference ($\Delta T_{\mathrm{Au/Py}} = T_{\mathrm{RT}} - T_{\mathrm{Au/Py}}$) of the respective Au/Py interfaces extracted from the simulated temperature profile (dashed line, right y-axis). The simulation result shown in Figure 7.2(c) depicts the difference between the average temperature rise of the two interfaces ($\Delta T = \Delta T_{\mathrm{Au/Py,r}} - \Delta T_{\mathrm{Au/Py,l}} = T_{\mathrm{Au/Py,l}} - T_{\mathrm{Au/Py,r}}$, where l = left, r = right). The left and the right y-axis, associated with the experimental data and the simulation result, respectively, are scaled according to the Seebeck coefficient $\Delta S \approx 21.7\,\mu\mathrm{V\,K^{-1}}$. This allows us to quantitatively compare the measured voltage with the simulated temperature rise.

In all presented cases we find very good agreement between measurement and simulation. The simulation data accurately reproduces the absolute minimum/maximum of the thermocouple signal when directly heating the corresponding crossing point. The data also indicates the decay of the signal including the local dips when the laser is positioned on one of the other Au wires. However, some of the features appear sharper in the simulation, in particular close to the contacted interface. For instance the simulated curve shown in Figure 7.2(a) exhibits a symmetric double peak structure due to the increase in reflectivity when the laser spot is centered on the Au wire. This feature is hardly observable in the experimental data. We attribute this to imperfections in the real sample geometry (smoothed edges) and a non-ideal laser beam profile (i.e. not purely Gaussian as assumed in the simulation), resulting in a modified effective heating profile.

Surprisingly, voltages of the same order of magnitude were also observed when measuring the voltage along the Py wire (see Figure 7.3(a)). The voltage changes its sign, depending on the position of the laser spot with respect to the center of each of the Au wires. As illustrated in the cross section of one of the Au/Py crossing points (Figure 7.3(b)), the direct path between the cold junction contacts does not cross any Au/Py interface that would give rise to a Seebeck signal like in the previously discussed cases. However, due to the much higher electrical conductivity of the Au layer, the current is expected to redistribute and enter the Au layer. The Au-covered part of the Py wire can therefore be considered as a region with an effective Seebeck coefficient S_{eff} that forms interfaces with the Py wire to either side of the Au wire,

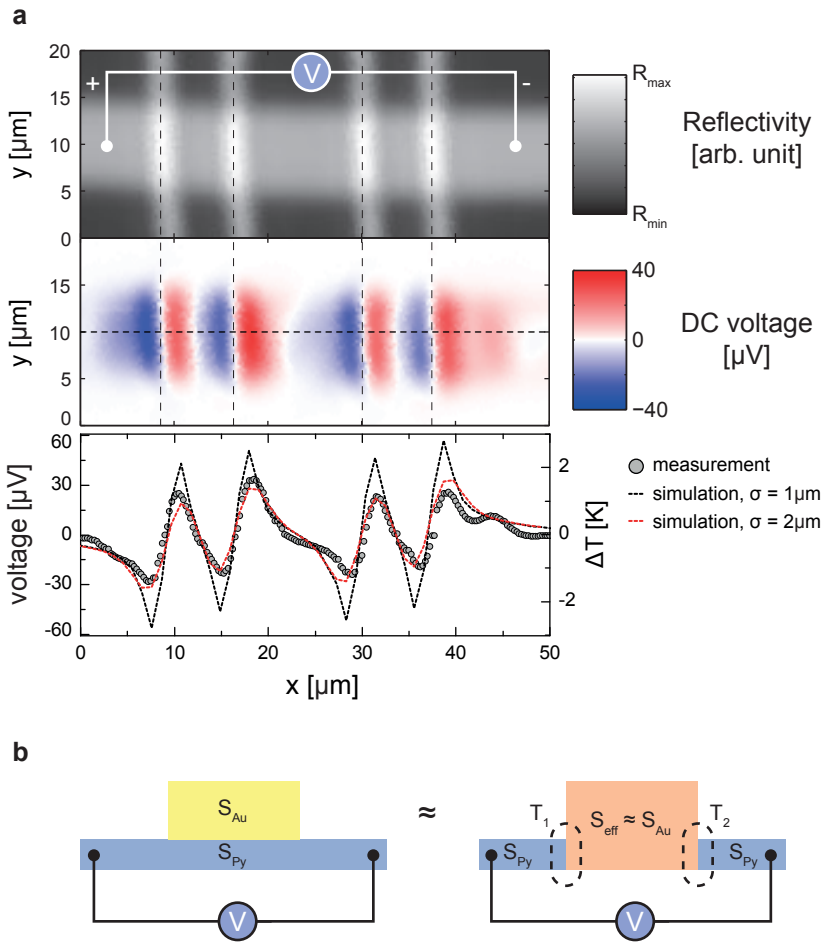

Figure 7.3 | Seebeck voltage generated by laser-heating of Py/Au thermocouples II. (a) Same sample, measurement parameters (except smaller scan area) and presentation of data as in Figure 7.2 for voltage measured between both ends of the Py wire. Simulation data is shown for $4\sigma \approx 4\,\mu m$ and $8\,\mu m$ spot size. (b) Cross-section of a Au/Py interface and equivalent structure with two oppositely oriented thermocouples.

as illustrated in Figure 7.3(b). It can be shown that the effective Seebeck coefficient of two metallic layers A and B connected in parallel is given by

$$S_{\mathrm{eff}} = -\frac{\sigma_{\mathrm{A}} S_{\mathrm{A}} + \sigma_{\mathrm{B}} S_{\mathrm{B}}}{\sigma_{\mathrm{A}} + \sigma_{\mathrm{B}}}$$

where $\sigma_{\mathrm{A,B}}$ and $S_{\mathrm{A,B}}$ (taken from Table 6.2) denote the conductances and Seebeck coefficients of the two layers, respectively. For the geometry and materials used here, this approach yields $S_{\mathrm{eff}} = 0.26\,\mu\mathrm{V\,K^{-1}}$, resulting in a total Seebeck coefficient at the interface with the Py wire of $\Delta S = 20.26\,\mu\mathrm{V\,K^{-1}}$. A temperature difference between the left and the right Au edge thus gives rise to a measurable Seebeck voltage, as observed in our experiments (see Figure 7.3(a) middle and bottom panel).

Further confirmation for this is provided by the comparison with the simulation data shown in the bottom panel of Figure 7.3(a). Here, the temperature difference (right y-axis) corresponds to the total temperature difference between all eight Au/Au-Py interfaces, taking into account their polarity (similar to the case shown in Figure 7.2(c)). While the result obtained for $\sigma = 1\,\mu\mathrm{m}$ reproduces the sign changes very well, it overestimates the signal strength and exhibits much sharper peaks than the experimental data. However, very good quantitative agreement is found for $\sigma = 2\,\mu\mathrm{m}$, clearly confirming the Seebeck effect due to the top Au layer as the origin of the observed voltage pattern. Furthermore, this suggests that the measured beam size is not accurate. This could be caused by a variation of the z-position that occurred after the spot size measurement or a slightly tilted sample plane, changing the focus as a function of x-y-position.

In summary, from the four different experiments we conclude that the observed voltage signals are due to thermovoltages dominated by the Seebeck effect. In addition to that, the excellent agreement between experimental data and simulation confirms the reliability of the modeling.

7.1.2 Influence of sample substrate and laser wavelength

Initial measurements were carried out on samples fabricated on GaAs/SiO_2 (batch I, as described in Section 6.1). Complications arise in this case because of photo-induced space charge, as shown below. Figure 7.4(a) shows the reflectivity images as well as the simultaneously acquired voltage maps for three wavelengths between $\lambda = 532\,\mathrm{nm}$ and $\lambda = 980\,\mathrm{nm}$ at $P_{\mathrm{laser}} \approx 15\,\mathrm{mW}$ and σ between 1 and 2.5 µm. The sample is wired in the 2-thermocouple configuration, very similar to the one shown in Figure 7.2(c).

In line with our previous results, for all three wavelengths we observe both a local maximum and a local minimum of the voltage at the positions of the two contacted Au/Py interfaces. The polarity of the generated voltage is consistent with the data shown in Figure 7.2(c), which we explained by the Seebeck effect. The variation of the signal strength as a function of wavelength is attributed to the wavelength-dependence of both the sample reflectivity and

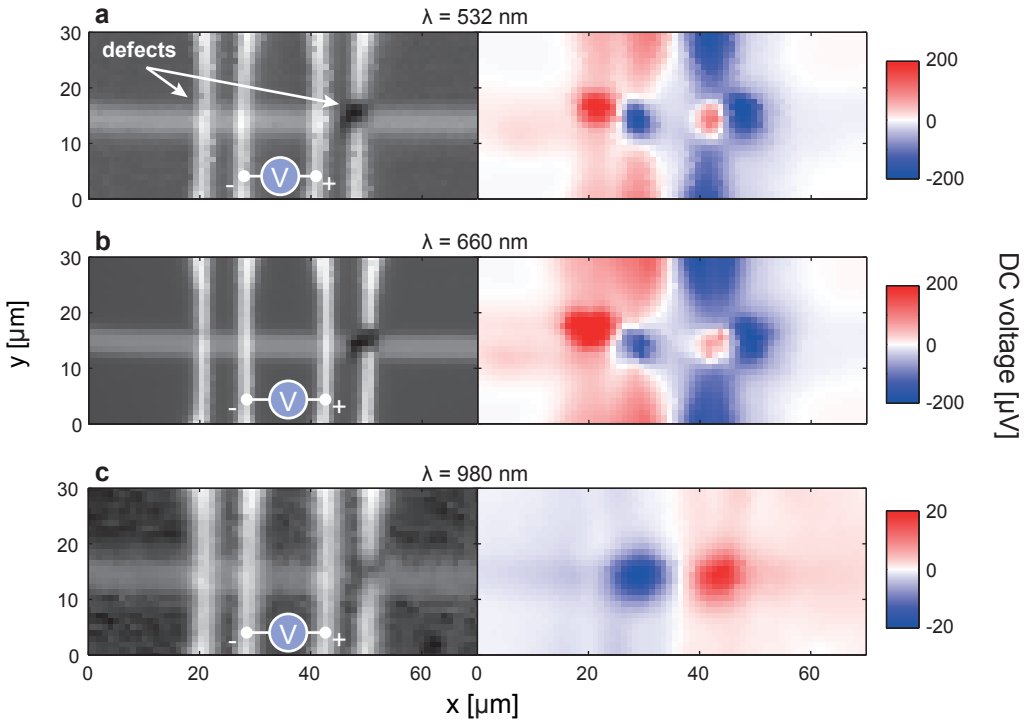

Figure 7.4 | Wavelength-dependence of laser-induced voltage in samples based on GaAs/SiO_2 substrate. Reflectivity image (left panels) and corresponding voltage map (right panel) for wavelength $\lambda = 532\,\text{nm}$ (a), $\lambda = 660\,\text{nm}$ (b) and $\lambda = 980\,\text{nm}$ (c). Sample from batch I with $w_{\text{Py}} = 4\,\mu\text{m}$.

the absorption of the objective lens as well as to the different beam and spot profiles of the three laser sources. In the following we focus on a qualitative comparison of the data.

In contrast to the MgO-based sample where the signal levels off to zero when the laser is moved away from the crossing points (see Figure 7.2(c)), additional voltage signals can be identified in the GaAs/SiO_2-based samples: Figure 7.4(a) and (b) indicate that significant voltages on the order of 200 µV are generated when illuminating the sample at $\lambda = 532\,\text{nm}$ and $\lambda = 660\,\text{nm}$ close to the Au and Py wires. Voltages of the same magnitude are observed even several hundreds of µm away from the Au/Py interfaces, excluding a Seebeck-related origin. The signal shows the same symmetry with respect to the contacted Au wires as the Seebeck voltage, and it is particularly strong close to the defects being present in the structure. These defects (see left panel in Figure 7.4(a)) are most likely caused by electrostatic discharges that may have damaged the SiO_2 insulation layer between the Au/Py wires and the GaAs substrate. This and the fact that such voltages could not be observed in the MgO samples suggest that the observed effect is related to the GaAs substrate.

GaAs has a bandgap of 1.43 eV, which corresponds to a photon wavelength of about 868 nm. In the case of Figure 7.4(a) and (b) the laser beam will thus generate free carriers in GaAs by creating electron-hole pairs, which in turn change the surface potential at the GaAs-SiO_2 interface. The resulting voltage, commonly called surface photo voltage (SPV), is well-known

from metal-insulator-semiconductor (MIS) structures like the ones formed by the Au/Py wires on top of SiO_2/GaAs (for a review on SPV see Reference [183]). The effect is expected to be weaker or to disappear completely for sub-bandgap photon energies. In fact, at $\lambda = 980\,\text{nm}$ (Figure 7.4(c)) we obtain a voltage map without significant photovoltages, very similar to the one obtained from the MgO-based sample. The major differences compared to Figure 7.2(c) are that Figure 7.4(c) has an inferior resolution (due to $\sigma \approx 2.5\,\mu\text{m}$) and that the Seebeck signal is non-zero for illumination away from the wires. The latter is due to the non-zero absorption in GaAs, as opposed to MgO that is completely transparent for visible wavelengths.

We therefore conclude that the voltage observed along the Py and the Au wires at the two shorter wavelengths are due to the SPV effect in the MIS structure formed by Au or Py on SiO_2/GaAs.

7.1.3 Anomalous Nerst effect

We now turn to the Anomalous Nernst effect (ANE) that is expected to induce a magnetization-dependent voltage in magnetic structures subjected to heat currents (see Section 5.1). First, the magnetic switching behavior of the Py wire is characterized using AMR measurements. Figure 7.5(a) illustrates the employed 4-point resistance measurement that eliminates resistance contributions from the leads and the Au/Py interfaces. A current of $I_{\text{DC}} = 200\,\mu\text{A}$ is fed through the Py wire using the outer Au wire pair while the resulting voltage drop is measured using the inner pair.

Figure 7.5(b) shows the resistance change due to AMR as a function of applied magnetic field H for a sample from batch I with $w_{\text{Py}} = 4\,\mu\text{m}$. Here the MR is given by $\Delta R = (R(H) - R_{\parallel})/R_{\parallel} - 1$, where $R_{\parallel} = 128.9\,\Omega$ is the resistance of the two stable magnetization configurations with the magnetization aligned along the wire. The external magnetic field is applied along the direction of the wire. Due to the large lateral dimensions, the wire does not behave as a single-domain particle. The magnetization thus reverses by the formation and propagation of one or several domain walls. As discussed in Part I of this thesis, domain walls give rise to a decrease in resistance via the AMR as they introduce regions with the magnetization pointing perpendicular to the current flow. Hence, Figure 7.5(b) allows us to identify the magnetic reversal of the wire. We extract a coercive field of $H_{\text{c}} \approx 41\,\text{Oe}$, considering the sharp drop of the MR to $\Delta R \approx -0.2\,\%$.

Figure 7.5(c) and (e) illustrate the way ANE signals can be acquired and interpreted in the present sample geometry and measurement setup. We call V_{x} and V_{y} the voltages measured between a pair of Au wires and between both ends of a single Au wire, respectively. As discussed in Section 6.2.2, the laser-based heating generates both an in-plane temperature gradient (mainly defined by the Gaussian beam profile) as well as a large out-of-plane temperature gradient as most of the heat is immediately absorbed by the substrate. Strong shape anisotropy keeps the magnetization of the 22 nm thin Py wires in the plane of the sample. Therefore, we do not expect a measurable in-plane ANE voltage due to the in-plane temperature gradient

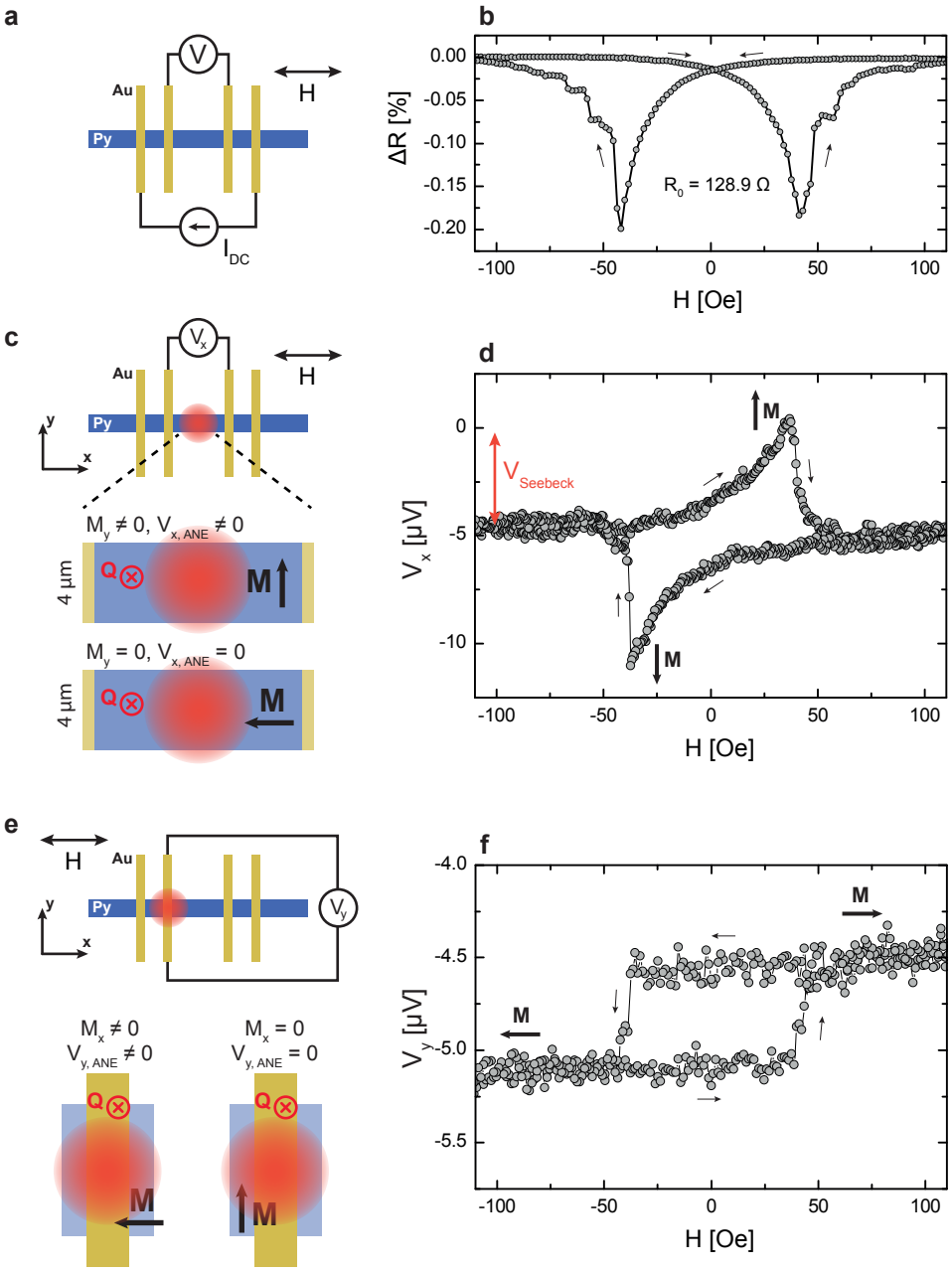

Figure 7.5 | AMR and anomalous Nernst effect in a 4 µm wide Py wire. (a) Circuit diagram illustrating the sample region probed by the AMR measurement, (b) MR vs. H loop taken at $I_{DC} = 200\,\mu A$, indicating magnetization reversal with coercive field $H_c \approx \pm 41\,Oe$. (c) Longitudinal ANE measurement with $V_{x,ANE} \propto M_y$. (d) Hysteresis loop indicating non-zero M_y at reversal field H_c. (e) Transverse ANE measurement with $V_{y,ANE} \propto M_x$. (f) Hysteresis loop showing different ANE signal levels for M parallel and anti-parallel to x with switching at H_c. Sample taken from batch I with $w_{Py} = 4\,\mu m$. Small black arrows in (b), (d) and (f) indicate the sweep direction. ANE measurements were taken at an incident laser power of $P \approx 11.7\,mW$ at $\lambda = 532\,nm$ and $\sigma \approx 1.5\,\mu m$.

[see Equation (5.3)].

In contrast to the use of an in-plane gradient, an out-of-plane temperature gradient in an in-plane magnetized sample generates a voltage pointing perpendicular to both the magnetization and the temperature gradient, i.e. in the plane of the sample. Hence, the magnetization-dependent part of V_x is expected to be proportional to M_y, the y-component of the magnetization in the laser-heated region (see Figure 7.5(c)). The x-component of the magnetization, M_x, can be probed by measuring the voltage drop along the y-direction V_y, as illustrated in Figure 7.5(e). In the latter case, however, the voltage signal is expected to be small as the Au wire electrically shorts the heated region. It is also important to note that in the present measurement configuration V_x and V_y always represent a superposition of the ANE voltage and the (usually dominating) Seebeck voltage (see Section 7.1.1).

Figure 7.5(d) shows V_x as a function of the magnetic field H. For this measurement the laser spot is positioned between the two Au probe contacts. If one positions the laser spot exactly at the center, the Seebeck signals from the two contacted thermocouples cancel out [see Figure 7.2(c)]. When moving away from the center, a Seebeck voltage develops that conceals the ANE voltage already for small deviations ($\sim 1\,\mu$m) from the center position. In this case, we have observed increased noise, making the measurement of the ANE effect less reliable. In Figure 7.5(d) we attribute the offset of about $-5\,\mu$V to a small remaining Seebeck voltage due to a slightly off-center position of the laser spot.

In line with the AMR measurements discussed above, V_x exhibits a peak/dip close to the coercive field H_c. This indicates that the magnetization is not collinear with the applied field H and $M_y \neq 0$ at H_c, confirming the in-plane rotation of the magnetization in the heated region. The magnetization reversal occurs at slightly smaller fields than predicted by the AMR measurement (37 Oe vs. 41 Oe). As we will see later (in Section 7.2) this can be attributed to heat-assisted magnetization reversal due to the continuous laser-heating of the probed region of the sample. We obtain $V_x(H > H_c) = V_x(H < -H_c)$, as the ANE ($V_{x,ANE}$) vanishes at saturation (see Figure 7.5(c)). In contrast to the AMR, which exhibits a $\cos^2$-dependence on the angle between magnetization and current, the ANE signal allows us to extract the sense of rotation as $V_{x,ANE}$ changes its sign when reversing M_y. In a perfectly symmetric geometry with a perfectly aligned magnetic field, the sense of rotation is expected to be random from field sweep to field sweep. However, we consistently observe a sign change of $V_{x,ANE}$ depending on the sweep direction (see Figure 7.5(d)), suggesting that the field is slightly misaligned with respect to the direction of the wire. Additionally, the observed sign change excludes AMR as the origin of the magnetization-dependent signal.

Next we study V_y as a function of the applied field H (Figure 7.5(f)) using the configuration depicted in (e). For this measurement, the laser spot is positioned at the center of one of the Au/Py interfaces in order to heat the Py wire underneath the Au wire while avoiding large Seebeck-induced signals [see Figure 7.3]. V_y exhibits a hysteretic behavior, with the voltage alternating between the values of $V_{y,ANE}$ that correspond to the parallel and the anti-parallel

magnetization configuration of the Py wire. Like in Figure 7.5(d), the switching fields are close to the ones determined by the AMR measurement. The significantly reduced signal amplitude of only $V_{\mathrm{y,ANE}} \approx 550\,\mathrm{nV}$ (compared to $V_{\mathrm{x,ANE}} \approx 11.5\,\mu\mathrm{V}$ in Figure 7.5(d), i.e. $\frac{V_{\mathrm{x,ANE}}}{V_{\mathrm{y,ANE}}} \approx 0.047$) is attributed to two different factors: First, as noted previously, the Au wire represents a metallic shunt exactly above the part of the Py wire where the ANE voltage is generated. Taking into account the difference in thickness and conductivity of the two wires, a reduction by a factor of approximately $t_{\mathrm{Py}}/t_{\mathrm{Au}} \cdot G_{\mathrm{Py}}/G_{\mathrm{Au}} = 0.07$ can be expected. Second, when the incident laser power is kept constant, the absorbed power for a laser spot position on the Au surface is smaller compared to the Py surface (see discussion of reflectivity in Section 6.2.2). The observed reduction by a factor of ~ 0.047 is hence within the expected order of magnitude.

Having confirmed that the observed signals agree well with the expected behavior of the Nernst effect, we now calculate a first estimate of the Nernst coefficient based on the data presented in Figure 7.5(d): As the sample cannot be saturated along the y-axis in the used geometry, we assume as a rough estimate that the y-component of the average magnetization between the Au wires m_{y} reaches a maximum of 50 % of $|\boldsymbol{m}|$ at the maximum of the observed voltage signal of $\Delta V_{\mathrm{x}} \approx 5.75\,\mu\mathrm{V}$. From numerical simulations (see Section 6.2.2) we deduce a value of $\nabla_z T \approx 5.6 \times 10^6\,\mathrm{K\,m^{-1}}$ for the average out-of-plane temperature gradient at the center of the laser spot . As the intensity within the laser spot follows a Gaussian distribution given by $I(x,y) = 1/(2\pi\sigma^2)\exp\left[-(x^2+y^2)/(2\sigma^2)\right]$, we consider the same distribution for $\nabla_z T$. We then approximate this Gaussian profile by an equivalent square profile of width $w = 4\,\mu\mathrm{m}$ and homogeneous temperature gradient $(\nabla_z T)' \approx 0.88\nabla_z T$. This allows us to define a homogeneous ANE-generated electric field $E_{\mathrm{ANE}} = \Delta V_{\mathrm{x}}/w$. Additionally, due to clipping of the beam (the spot size d is larger than the width of the Py wire w), only $\int_{-\infty}^{+\infty}\int_{-2\,\mu\mathrm{m}}^{+2\,\mu\mathrm{m}} I(x,y)\mathrm{d}x\,\mathrm{d}y \approx 82\,\%$ of the incident beam intensity reaches the Py wire. Hence, the effective temperature gradient reduces to $(\nabla_z T)_{\mathrm{eff}} = 0.82(\nabla_z T)' = 0.72(\nabla_z T)$. Finally, using Equation (5.3) we obtain an anomalous Nernst coefficient of

$$N_{\mathrm{ANE}} \approx \frac{E_{\mathrm{ANE}}}{m_y(\nabla_z T)_{\mathrm{eff}}} = \frac{\Delta V_{\mathrm{x}}}{\frac{1}{2}\cdot w \cdot 0.72(\nabla_z T)} \approx 0.71\,\mu\mathrm{V\,K^{-1}}\,,$$

a value between the ones previously reported in Reference [184] for Py ($2.6\,\mu\mathrm{V\,K^{-1}}$) and in Reference [160] for Ni ($0.13\,\mu\mathrm{V\,K^{-1}}$). This agreement further confirms that we can attribute the observed magnetization-dependent voltages to the anomalous Nernst effect.

7.1.4 Time-resolved measurement of Seebeck and ANE signals

The observation of the ANE presented above was restricted to selected positions of the laser spot where the usually dominating Seebeck effect cancels out. A separation and simultaneous investigation of both effects at arbitrary positions of the laser spot is not feasible using DC measurements as the strong Seebeck signal masks the ANE for most positions of the laser spot. As we will see in the following, the two signals can be distinguished by analyzing their time-evolution.

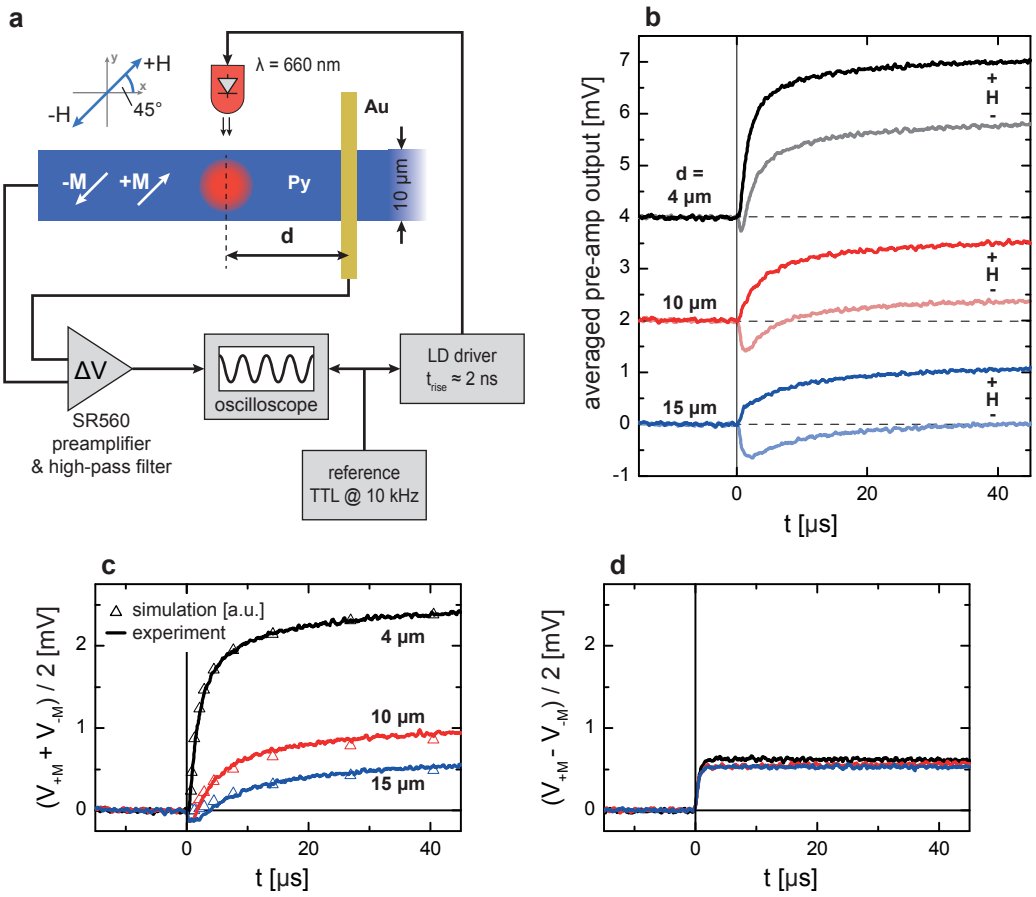

Figure 7.6 | Time-resolved measurement of Seebeck and ANE signals. (a) Modified measurement setup and schematic illustration of laser positioning and electrical connections (see text for description). (b) Time-evolution of voltage (sample batch II with MgO substrate, $w_{\mathrm{Py}} = 10\,\mu\mathrm{m}$) upon arrival of a laser pulse with $P_{\mathrm{peak}} = 39.5\,\mathrm{mW}$ and $\lambda = 660\,\mathrm{nm}$ for both magnetization states (-M, +M) and three different distances d between the position of the laser spot ($\sigma \approx 1.4\,\mu\mathrm{m}$) and the contacted Au/Py thermocouple. For clarity, the curves are offset along the y-axis by 2 mV (indicated by the dashed lines). (c) Field-independent part $(V_{+\mathrm{M}} + V_{-\mathrm{M}})/2$ due to the Seebeck effect (solid lines) along with simulated temperature rise at Au/Py thermocouple (open symbols, data is fitted to the experimental data using one common scaling factor). (d) Field-dependent part $(V_{+\mathrm{M}} - V_{-\mathrm{M}})/2$ of the data shown in (a) due to the anomalous Nernst effect.

To perform time-resolved measurements using pulsed laser heating, we extend the measurement setup presented in Section 6.2.1, as illustrated in Figure 7.6(a). A reference (TTL) signal with $f_{\mathrm{ref}} = 10.223\,\mathrm{kHz}$ triggers an Agilent 81110A pattern generator ($t_{\mathrm{rise}} = 2\,\mathrm{ns}$), which drives the laser diode ($\lambda = 660\,\mathrm{nm}$) with a square wave voltage. This generates a train of laser pulses with $P_{\mathrm{avg}} = 19.75\,\mathrm{mW}$ at a duty cycle of 50 % (i.e. $P_{\mathrm{peak}} = 39.5\,\mathrm{mW}$). In a separate measurement, the optical rise time of the laser diode was determined to be $t_{\mathrm{rise}} \approx 3\,\mathrm{ns}$. As the heating power is proportional to the optical intensity, it reaches its maximum of $P_{\mathrm{heat}} = (1-R)P_{\mathrm{peak}} \approx 16.2\,\mathrm{mW}$ within the diode's rise time. The size of the laser spot on the sample is $4\sigma \approx 5.6\,\mu\mathrm{m}$. We use a voltage preamplifier (Stanford Research SR560, maximum bandwidth 1 MHz) to amplify the potential difference between one of the Au wires and the end of the Py wire, as shown in Figure 7.6(a). The amplifier suppresses low-frequency noise using a high-pass filter with $f_{-3\mathrm{dB}} = 100\,\mathrm{Hz}$. A digital storage oscilloscope is employed to average and measure the amplified signal. The overall nominal amplification factor is about 20.

The time-evolution of the laser-generated voltage is measured at the rising edge of the laser pulse ($t_0 = 0\,\mu\mathrm{s}$) for two oppositely oriented magnetization states (see Figure 7.6(a)). The magnetization is aligned using a magnetic field $|H| \approx 350\,\mathrm{Oe}$ applied at $\alpha \approx 45°$ with respect to the wire axis. Additionally, prior to each measurement, the magnetization is saturated in a magnetic field of $|H| \approx 2\,\mathrm{kOe}$ to exclude hysteresis effects. Figure 7.6(b) shows the experimental data obtained for three different distances $d = \{4, 10, 15\}$ µm between the position of the laser spot and the contacted Au/Py thermocouple (the definition of d is illustrated in Figure 7.6(a)). In all three cases we obtain a convolution of two distinct contributions exhibiting different time evolution: We observe a slowly growing increase of the voltage that dominates the overall voltage for small d and saturates for large t (of the order of 50 µs). In addition to that, there is a fast-rising magnetization-dependent offset that does not significantly change its magnitude as a function of d.

In order to directly compare the two contributions we separately plot the magnetization-independent contribution and the magnetization-dependent contribution in Figure 7.6(c) and (d), respectively. Strikingly, the magnetization-independent component of the signal declines rapidly with increasing distance d, suggesting that the signal depends on the temperature at the thermocouple, i.e. the crossing point of the Au and the Py wires. At the same time we observe a prolongation of the rise time (15.4 µs, 21.3 µs and 25.8 µs for $d = 4$, 10 and 15 µm, respectively).

To confirm the origin of the signal we additionally perform numerical simulations of the time-dependent temperature rise of the Py/Au interface as a function of d, as described in Sections 6.2.2 and 7.1.1. For qualitative comparison the simulation data is scaled using a constant factor to fit the experimental data. As shown in Figure 7.6(c) (open symbols) we obtain excellent qualitative agreement between experiment and simulation, both in terms of the rise time as well as the relative strength of the signals as a function of d. The behavior of the rise time can be understood considering the heat current between laser spot and thermocouple: It can be shown that the heat current through a spherical shell for a given

temperature difference is proportional to $1/(1/r_h - 1/d)$, where r_h is the radius of the heat source and d the radius of the outer shell (derived from Fourier's law). The heat rate drops for increasing d, leading to an increasing rise time. Our data confirm that the measured signal is in fact proportional to the temperature rise at the thermocouple and we therefore attribute the magnetization-independent component of the signal to the Seebeck effect.

In contrast to that, the magnetization-dependent component shown in Figure 7.6(d) does not exhibit any significant dependence on d and it shows a much faster rise time of 1.3 µs. In this case, the rise time is limited by the measurement setup (pre-amplifier bandwidth: 1 MHz, bandwidth of measurement setup ≤ 1 MHz) and we assume an instantaneous generation of the voltage signal on the timescale considered here (µs). This indicates that the effect depends both on the magnetization and on the laser-induced temperature (or temperature gradient) right at the position of the laser spot. We therefore conclude that this fast-rising signal is due to the ANE. The measurement geometry is similar to the geometry shown in Figure 7.5(c) and (d), where $V_{\mathrm{x,ANE}} \propto M_{\mathrm{y}}$. Due to the field angle of $\alpha = 45°$ the measurable ANE signal is reduced by a factor of $\sin(45°) \approx 0.71$.

In summary, we have performed measurements of the laser-induced voltage in Py/Au structures as a function of laser position, magnetization and time. Based on these measurements we have unambiguously identified and separated two major contributions to the generated signals in samples based on an MgO substrate: The Seebeck effect, appearing upon heating of the sample in the vicinity of the Au/Py crosses, and the anomalous Nernst effect, which is due to the out-of-plane temperature gradient in the magnetic Py wire. Substrates based on SiO_2/GaAs showed in addition surface photovoltage generation. In the following we use the ANE to perform thermoelectrical magnetic imaging of a Py wire.

7.2 Thermoelectrical magnetic imaging of magnetization reversal

Following the work of Gönnenwein et al. [160] we perform thermoelectrical magnetic imaging of a Py wire based on the anomalous Nernst effect signal. In contrast to Reference [160], our laser spot diameter is of microscopic diameter (down to $\sigma \approx 550$ nm) allowing for significantly better spatial resolution. For this purpose, we use the configuration shown in Figure 7.5(c), where the voltage is measured such that its magnitude is proportional to the y-component of the magnetization (i.e. across the wire).

As discussed above, the ANE is difficult to separate from the Seebeck effect when both signals are generated simultaneously. In order to obtain an ANE-dominated signal, we therefore move the laser spot to a position along the Py wire that is far away (about 500 µm) from the Au/Py thermocouples. Figure 7.7(a) shows a reflectivity image of a 50 µm long section of the Py wire at this position. As illustrated, the in-plane magnetic field is applied at an angle of $\alpha \approx 45°$ to the wire.

First, we characterize the magnetization reversal of the 10 µm wide Py wire based on the

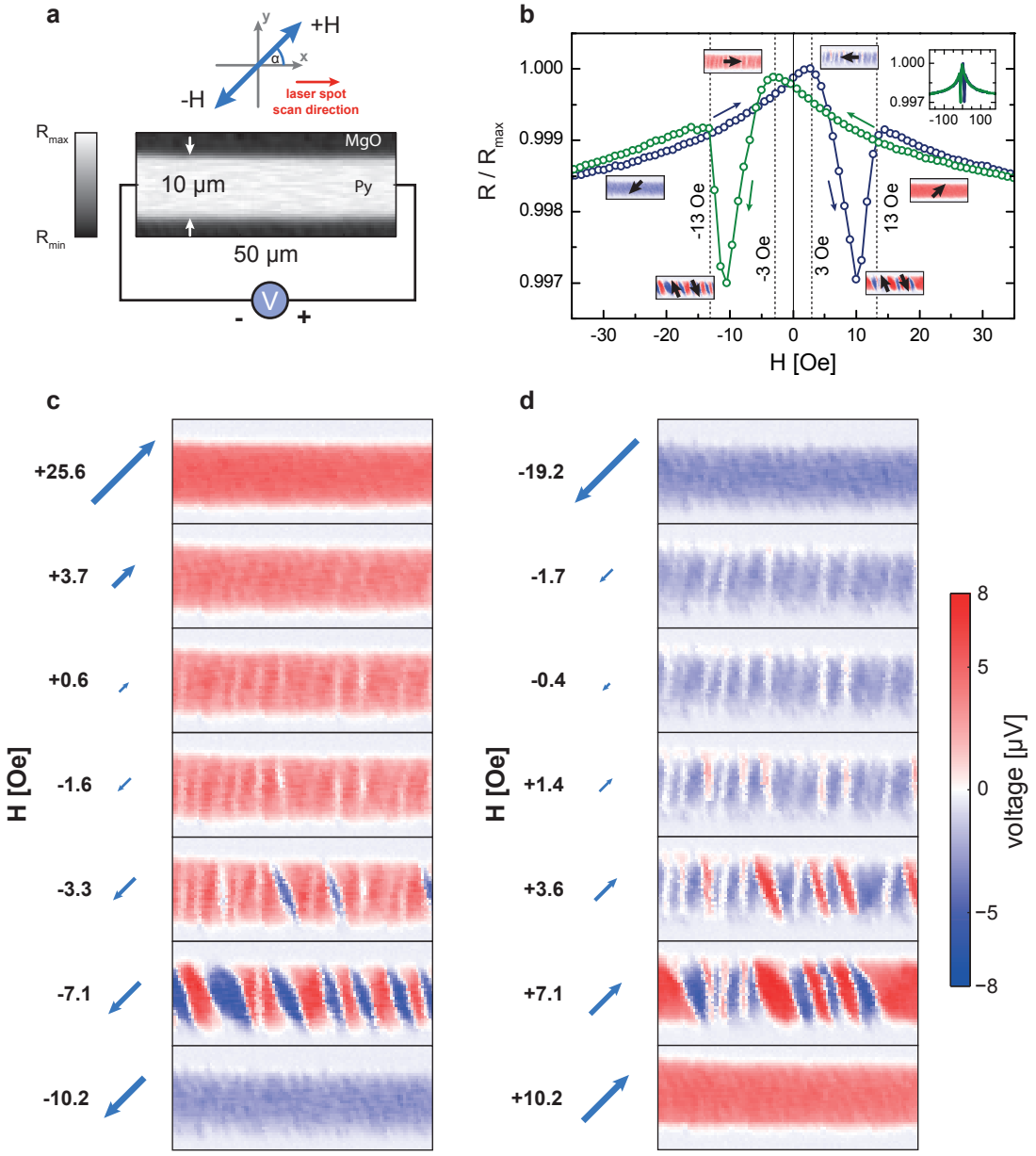

Figure 7.7 | Magnetization reversal of a Py wire imaged using the anomalous Nernst effect. (a) Reflectivity image (50 µm × 20 µm) of a 10 µm wide Py wire (sample batch II with MgO substrate) at $d \approx 500\,\mu m$ from Au/Py thermocouples, measured at $\lambda = 532\,nm$, $P = 7.8\,mW$ and $\sigma_x \approx 550\,nm$, $\sigma_y \approx 800\,nm$. Magnetic field H is applied at angle $\alpha \approx 45°$ with respect to the wire, DC voltage shown in (c) and (d) is measured between both ends of the Py wire. The laser is scanned along lines parallel to x. (b) AMR as a function of applied field (blue: left to right, green: right to left), indicating magnetization reversal of the wire between 5 and 13 Oe ($H_c \approx 10\,Oe$). Inset: same data for wider field range. Schematic magnetization configurations along with voltage maps taken from (c) and (d) are shown for specific field values. Data normalized to $R_{max} = 4.28\,k\Omega$. (c & d) V_{ANE} maps with $V \propto M_y$ (see Figure 7.5(b)) for both sweep directions of the magnetic field.

AMR effect. As discussed previously, a magnetic structure of this size cannot be treated as a single-domain particle but reverses its magnetization via the formation and propagation of domain walls. Figure 7.7(b) shows the electrical resistance of the wire as a function of magnetic field. As expected, we observe a pronounced dip when the magnetization is reversed (see Section 7.1.3 and Part I of this thesis). The reversal occurs between $|H| \approx 3\,\mathrm{Oe}$ and $|H| \approx 13\,\mathrm{Oe}$ where the lowest point of the dip at $|H_c| \approx 10\,\mathrm{Oe}$ exhibits an MR ratio of about 0.3 %. The decreased resistance at this field indicates the formation of domain walls in the wire leading to a significant part of the magnetization pointing along the y-axis. At $H \approx 13\,\mathrm{Oe}$ the magnetization is completely reversed and the resistance returns almost to its initial level. The slow decay of the resistance for $|H| > 13\,\mathrm{Oe}$ is due to the interplay between the shape anisotropy and the field applied. At zero field the shape anisotropy forces the magnetization to point along the wire, leading to maximum AMR. However, when a large enough field is applied at $\alpha \approx 45°$, the magnetization uniformly rotates away from the wire direction, which lowers the resistance (see inset in Figure 7.7(b)).

Next, we turn to the ANE-based magnetic imaging of the Py wire. Figure 7.7(c) and (d) show sequences of ANE voltage maps that illustrate the spatial distribution of the y-component of the magnetization as a function of magnetic field. Here, (c) and (d) correspond to the sweep directions indicated by the green and the blue color in (b), respectively. Prior to both of these field scans, the magnetization is aligned with the field direction by applying a large field of $H \approx 500\,\mathrm{Oe}$. According to the definition of the anomalous Nernst effect [Equation (5.3)] and in line with the direction of the applied field, a positive (negative) sign of the detected voltage indicates a magnetization M pointing along (opposite to) the y-direction. This is confirmed by the top and bottom images in Figure 7.7(c) and (d) that show the uniformly magnetized state of the wire.

During the reversal process we observe the following behavior: when decreasing the field from saturation to zero (moving from top to bottom in Figure 7.7(c/d)), we observe a reduced ANE signal. This can be attributed to the influence of the shape anisotropy, which partly aligns the magnetization along the edges of the wire and hence reduces M_y. Reversing the field leads to the formation of oppositely magnetized domains in the wire that grow in size, as can be seen in (c) for $-3.3\,\mathrm{Oe}$ and $-7.1\,\mathrm{Oe}$ as well as in (d) for 3.6 Oe and 7.1 Oe. Magnetic wires of this size typically exhibit a diamond-like domain pattern [39]. We thus believe that the imaged magnetization structure exhibits a similar pattern that is distorted (i.e. tilted) by the applied field or locally changing anisotropy fields. Instead of one domain wall propagating through the entire wire, we observe a large number of locally nucleated domain walls that gradually reverse the magnetization. In both cases, the magnetization is completely reversed at $|H| \leq 10.2\,\mathrm{Oe}$.

The magnetization imaging qualitatively agrees with the data obtained from the AMR measurement discussed above. We can thus assign the magnetization states as resolved by thermoelectrical imaging to the most prominent features of the AMR curve shown in Figure 7.7(b). Interestingly, the switching fields are found to be consistently lower in the imaging experiment

and the magnetization structure is observed to be highly reproducible instead of randomly generated in each measurement. Parts of the observed magnetization structure even show some periodicity in the domain pattern (with a pitch of ~ 1.5 µm). This unexpected behavior is investigated in a subsequent measurement that we present in the following.

For a more detailed analysis of the field-dependence, we perform high-resolution line scans along the center of the wire, and we sweep the field in smaller steps [see Figure 7.8(a)]. From these line scans we then generate an image with the same color code as in Figure 7.7, where each row represents one line scan, i.e. the magnetization configuration for one specific field value. Figure 7.8(b) shows the result for a series of 80 µm long line scans carried out on a different part of the wire imaged in Figure 7.7. For both sweep directions of the field, magnetic domains of opposite orientation start to form at $H \approx 0$ Oe, increasing in size and difference in M_y when ramping up the field magnitude: vertical thin white lines turn into wide blue (red) regions in the lower (upper) panel. Complete magnetization reversal is observed at $H_c \approx 8$ Oe, in agreement with the results presented in Figure 7.7.

Strikingly, the x-positions where the domains start to appear are consistently the same, irrespective of the field sweep direction (see vertical dashed lines in Figure 7.8(c), 16 additional data sets (data not shown) exhibit the same behavior). It should be noted that the resolution of these line scans (and the technique in general) is defined and limited by the size of the laser spot. The sharp transitions between regions of opposite V_{ANE} (and thus opposite M_{y}) in Figure 7.8(a) can be well described by error functions with standard deviation $\sigma \approx 600$ nm, which is comparable to the measured spot size along x, $\sigma_x \approx 550$ nm. This suggests that the size of the DWs separating these regions is small compared to the laser spot size.

The results obtained from ANE line scans are further corroborated by the position-dependent ANE hysteresis loops presented in Figure 7.9: in this measurement, we keep the position of the laser spot constant while sweeping the magnetic field. The positions are indicated by dashed vertical lines in the upper panel. As a result, we obtain narrow hysteresis loops for positions that coincide with nucleation sites as indicated in Figure 7.8(b) (at 8 µm and 15 µm) and wide loops for positions outside these regions (at 5 µm and 11 µm), confirming the reproducibility of the magnetization pattern. This is in stark contrast to the random behavior expected from a perfect wire without defects, where thermal fluctuations play a dominating role in the reversal process. As the magnetization is 'reset' in the beginning of each measurement, persistent pinned domains that initiate the subsequent magnetization reversal are unlikely to exist. We believe that the observed behavior is due to nucleation sites induced by structural irregularities that are fixed in position. Such irregularities could be due to enhanced edge or surface roughness of the Py wire possibly induced by a rough substrate or the lithographic process.

In Figure 7.8(c), we study the influence of the laser power on the magnetization reversal. Each of the images depicts a close-up of the region indicated in Figure 7.8(b) (20 µm × 15 Oe), containing two well-separated nucleation sites. The incident laser power ranges from 3.9 mW

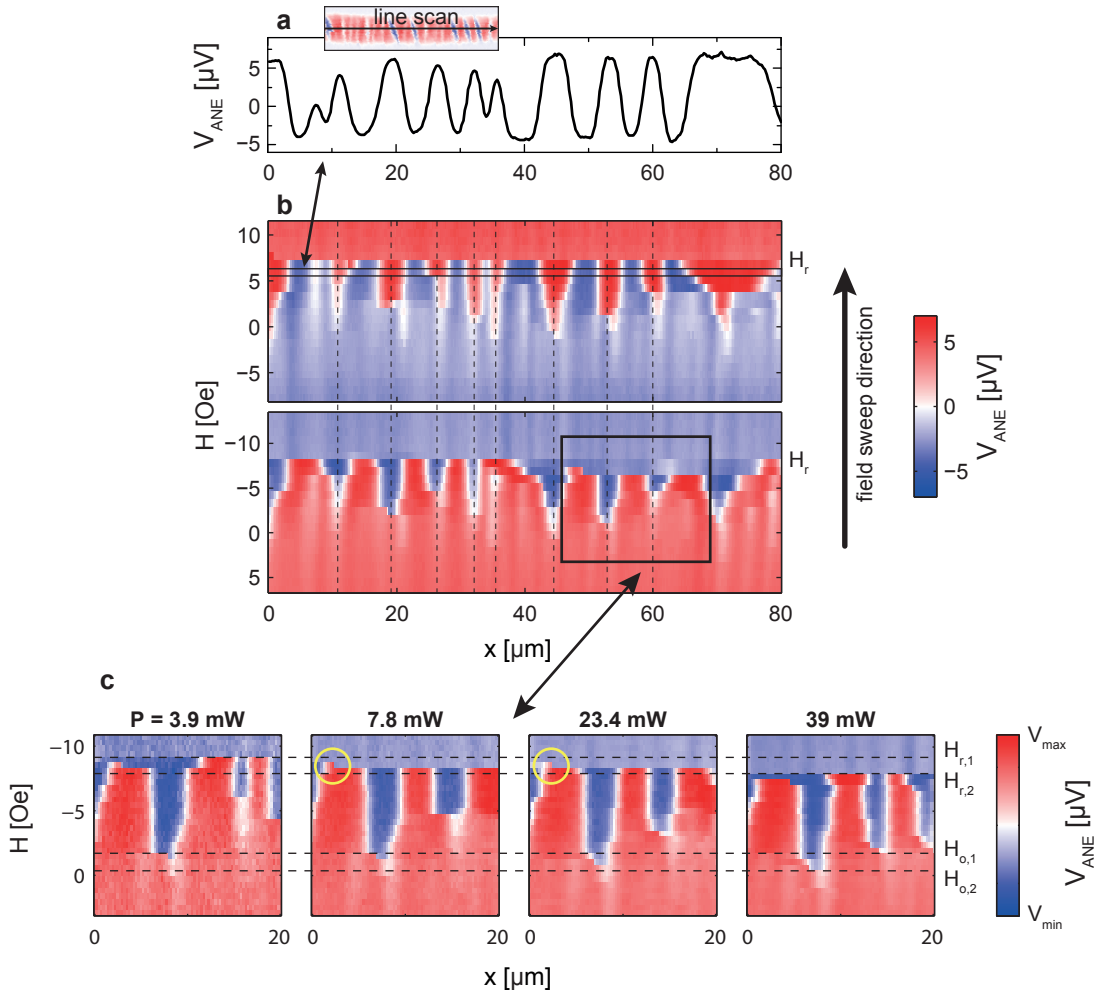

Figure 7.8 | Analysis of magnetization reversal using ANE line scans. (a) ANE voltage as a function of laser spot position for a 80 µm long line scan along the center of the Py wire (see inset for orientation of line scan). The ANE signal is acquired as described in Figure 7.7 at $H \approx 6$ Oe and $P \approx 7.8$ mW. (b) Field-dependent line scans: Each horizontal line represents the ANE voltage measured along the line shown in (a) for a different magnetic field H. Bottom panel: from H_+ to H_-, Upper panel: reversed direction. Vertical dashed lines indicate the reproducible occurrence of reversed domains. (c) Close-up line scan images of a 20 µm section of the data shown in (b) for four different levels of the incident laser power (data normalized to maximum voltage). Dashed lines indicate the minimum and maximum of the observed switching fields, yellow circles label the positions where magnetization switching occurs.

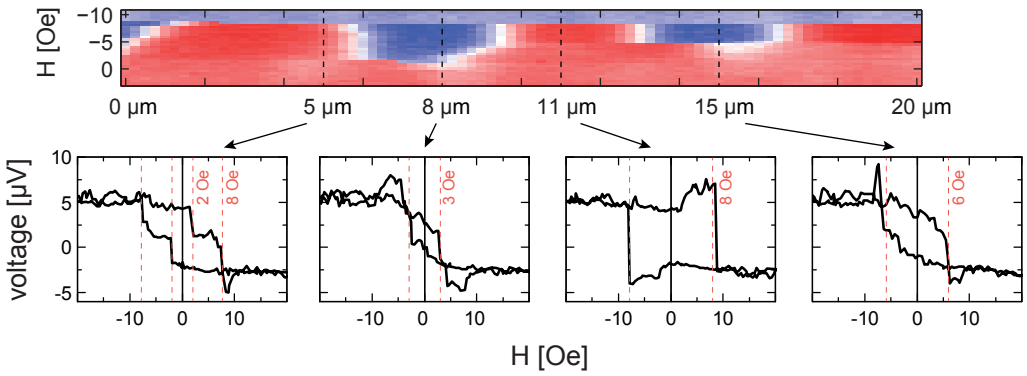

Figure 7.9 | Local position-dependent hysteresis loops. Upper panel: 20 µm line scan image taken from Figure 7.8(c) for 7.8 mW. Bottom panels: Local hysteresis loops ($V_{\mathrm{ANE}} \propto M_y$ vs. magnetic field H) for four different positions of the laser spot.

to 39 mW, which corresponds to a maximum temperature rise ΔT at the center of the spot of approximately 18 K and 180 K, respectively (values obtained from numerical simulation). Because these are separate measurements taken at a much smaller step size and scan area, the data for 7.8 mW is not exactly the same as shown in Figure 7.8(b) for the same power. The dashed horizontal lines indicate the smallest ($H_{\mathrm{r},2}$) and the largest ($H_{\mathrm{r},1}$) switching field for this set of measurements. Here, H_{r} is defined as the smallest field showing no pronounced inhomogeneity of the magnetization structure. Its value gradually drops from 9.4 Oe at 3.9 mW to 8.1 Oe at 39 mW, i.e. the reversal field is lowered by 1.3 Oe. At the same time, we observe an earlier onset of the domain formation with increasing P , as can be easily seen by comparing the bottom edges of the two blue regions in Figure 7.8(c). These are indicated by dashed horizontal lines at $H_{\mathrm{o},1} \approx 0.3$ Oe and $H_{\mathrm{o},2} \approx 1.6$ Oe. The onset field of the reversal process H_{o} is thus lowered by the same amount as the reversal field (about 1.3 Oe).

It is well-known that thermal excitation influences the rate of nucleation, propagation and annihilation of magnetic domain walls [185]. We therefore attribute the observed power-dependence to thermal effects due to the laser heating, which is inherent to the ANE-based imaging technique employed here. Hence, laser-induced heating is also the reason why the imaging experiments consistently yield a lower reversal field than the one deduced from the AMR measurement shown in Figure 7.7(b) ($H_{\mathrm{r,max}} \approx 9.4$ Oe vs. $H_{\mathrm{r,AMR}} \approx 13$ Oe).

In summary, we have successfully performed thermoelectrical magnetic imaging of a 10 µm wide Py wire using the anomalous Nernst effect. Despite the technique's limitation to probing only one axis of the magnetization at a time (here: M_y), it revealed some essential aspects of the micromagnetic behavior of the wire during magnetization reversal. We obtain qualitative agreement with the AMR measurements in terms of the reversal field, confirming the reliability of the technique. Our results indicate that the magnetization reversal in the Py wire investigated here is dominated by imperfections in the shape of the wire, giving rise to nucleation sites and partial pinning of magnetic domains.

8 Ferromagnetic resonance in laser-induced temperature gradients

In the two following experiments, we investigate the influence of a temperature gradient on the FMR. In a first step, we use the inductive detection scheme (see Section 6.3.2) to measure the FMR in thin Py strips subject to a macroscopic laser-induced temperature gradient. We then use the electrical (local) detection scheme (see Section 6.3.3) to measure the FMR in narrow Py wires subject to much larger microscopic temperature gradients induced by the intensity profile of the laser spot (see Section 6.2.2).

8.1 Inductive detection: Py thin film

In this experiment, we generate a homogeneous temperature gradient along a macroscopic ferromagnetic thin film, very similar to the geometry investigated in the pioneering work on the spin Seebeck effect [20, 4]. As shown in Figure 8.1(a), we use a Py film grown on a Si/SiO_2 substrate ($\sim 1\,\mathrm{mm} \times 7\,\mathrm{mm}$), where one end is attached to a large Cu block that acts as a heat sink. A thin layer of thermal paste holds the sample in place. The other (suspended) end is heated using a focused laser beam with $\lambda = 532\,\mathrm{nm}$, a spot size of $d = 4\sigma \approx 0.5\,\mathrm{mm}$ and a power of up to $P = 800\,\mathrm{mW}$ at a distance of about 3 mm from the position of the local resonator. Thanks to the relatively high thermal conductivity of Silicon ($148\,\mathrm{W\,m^{-1}\,K^{-1}}$ [21]) the absorbed laser power is mainly dissipated via the Cu block, resulting in a stationary temperature gradient along the length of the strip. As the heat source is small compared to the distance between the laser spot and the probed region of the sample, the temperature gradient across the long dimension of the sample is expected to be homogeneous (to first approximation only, i.e. neglecting other dissipation channels such as convection).

The FMR is measured at $f_{\mathrm{MW}} = 7.19\,\mathrm{GHz}$ using a local resonator positioned about 1 mm from the edge of the Cu heat sink and about 0.5 mm above the surface of the Py film. We use the field modulation technique presented in Section 6.3.3 with $f_{\mathrm{m}} = 77.234\,\mathrm{Hz}$ and a modulation field H_{m} sufficiently small to avoid distortions to the linewidth. Figure 8.1(b) shows $\mathrm{d}\chi''/\mathrm{d}H$ as a function of the DC magnetic field H_0 for various levels of the laser power (from 0 mW up to 800 mW). The experimental data (open symbols) is fitted by the derivative of a Lorentzian

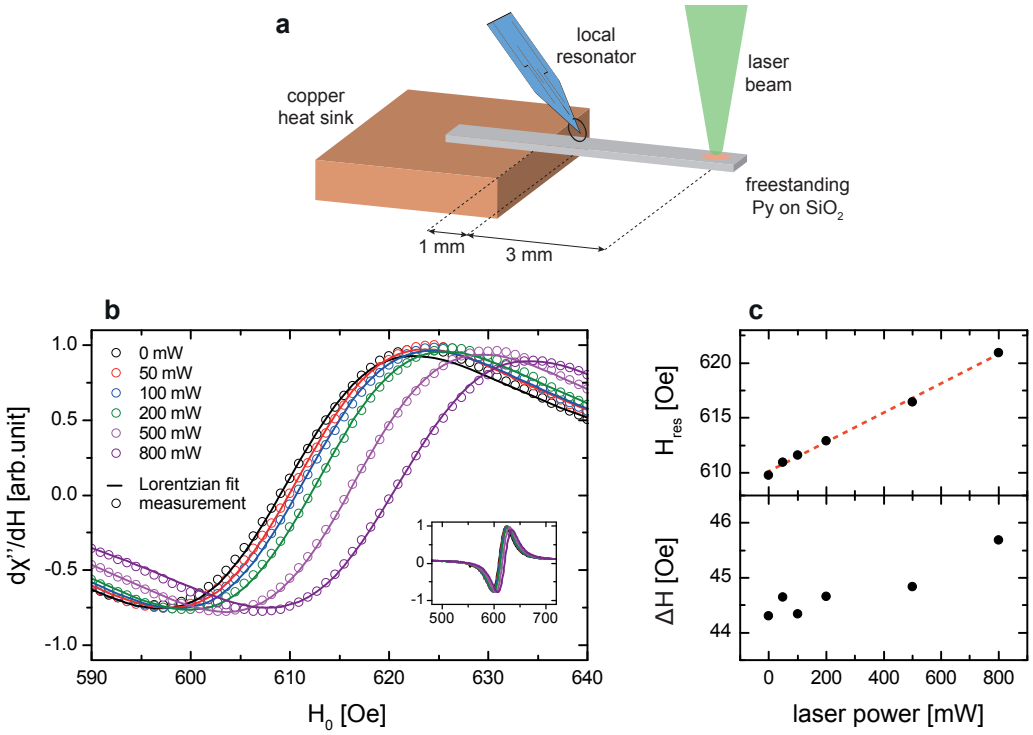

Figure 8.1 | FMR in a laser-heated freestanding Py/SiO$_2$ strip. (a) Measurement layout: Laser beam ($\lambda = 532\,\mathrm{nm}$) heats suspended end of Py strip (20 nm Py grown on a SiO_2 substrate). FMR is excited and measured using the field-modulation technique close to the edge to the Cu heat sink ($f_{\mathrm{MW}} = 7.19\,\mathrm{GHz}$, $P_{\mathrm{MW}} = 25\,\mathrm{dBm}$, $f_{\mathrm{m}} = 77.234\,\mathrm{Hz}$). (b) FMR spectra for laser power between 0 mW and 800 mW. Symbols indicate measured data points, solid lines represent best fits based on an asymmetric Lorentzian function, inset: same data for wider field range. (c) Position of resonance field H_{res} (upper panel) and linewidth ΔH (lower panel) as a function of laser power.

function (solid lines) from which we extract the properties of the resonance curve.

In Figure 8.1(c), we present both the resonance field H_{res} and the linewidth ΔH (FWHM, extracted as described in Section 6.3.2), as a function of laser power. As expected from theoretical considerations (see Section 5.3.2), we observe a shift of the resonance field towards higher values with increasing laser power, from $H_{\mathrm{res}} = 609.8\,\mathrm{Oe}$ without laser heating to $H_{\mathrm{res}} = 620.9\,\mathrm{Oe}$ at maximum laser power. Based on the discussion of the temperature-dependence of FMR in Section 5.3.2, we deduce from this change in H_{res} a maximum temperature difference of $\Delta T \approx 55\,\mathrm{K}$. Assuming that the heat sink does not heat up significantly, we obtain a rough estimate for the temperature gradient along the Py strip of about $\nabla T \approx 55\,\mathrm{K}/1\,\mathrm{mm} = 0.055\,\mathrm{K\,\mu m^{-1}}$. In addition to the observed shift, Figure 8.1(b) also indicates a reduction of the resonance amplitude with increasing temperature, which can be attributed to the decreasing saturation magnetization at higher temperatures. In line with previous studies [186, 187], our analysis does not show any drastic change of the linewidth ΔH close to room temperature. Only the last two data points for the highest laser power may indicate a trend towards larger linewidths. We attribute this increase to the increasingly inhomogeneous temperature distribution within

the region probed by the local resonator. The measured signal contains contributions from regions of different temperature and thus different H_{res}, which results in inhomogeneous broadening. Furthermore, without additional measurements, other heating-induced artifacts, such as thermal expansion or drift of the resonator's properties, can also not be excluded.

As discussed in Section 5.3.3, the additional torque induced by the absorption of a spin current depends on the spin current polarization. The polarization of an SSE-generated spin current is believed to follow the magnetization of the ferromagnet where it is generated. Thus, any change in the FMR (damping, amplitude, etc.) induced by such a thermally generated spin current would have to be asymmetric in H_0. However, our experimental data does not indicate any change in the behavior for the opposite field orientation: the obtained data correspond to the results presented in Figure 8.1 mirrored at $H_0 = 0\,\mathrm{Oe}$. We therefore conclude that in this sample the temperature gradient itself does not have a generic influence on the FMR measured at the position of the local resonator.

8.2 Electrical detection: Patterned Au / Py thin film structures

As we have seen in Section 6.2.2, the Gaussian shape of the laser spot profile allows us to generate temperature gradients on the µm-scale that can be controlled in both magnitude and position. At the same time, the electrical detection scheme presented in Section 6.3.3 enables the measurement of FMR in confined structures. Here, we combine both to study the FMR in a Py wire subject to a strong temperature gradient.

For the following measurements, we use a modified setup for the electrical detection of FMR where we replaced the detection based on field modulation (see Figure 6.8) by amplitude modulation using a microwave switch (see Figure 6.5). The EDFMR signal is then measured using a lock-in amplifier at the amplitude modulation frequency f_{m} of the switch. As we are interested in the generation of unidirectional temperature gradients, it is favorable to use a sample with a narrow magnetic wire and a relatively large laser spot. We thus use a sample from batch II (MgO substrate) with the smallest available width of the Py wire ($w_{\mathrm{Py}} = 4\,\mu\mathrm{m}$).

As the local character of the FMR measurement is vital for such a measurement, first we verify that the measured EDFMR signal stems exclusively from the contacted region in our sample. To identify this region, we exploit the observation from the previous section that heating causes the line shape of the FMR to change and the resonance field to shift to higher fields. Figure 8.2(a) illustrates how the voltage signal for a constant external magnetic field changes when heating the sample. We therefore expect to observe a change in the EDFMR signal only when we heat the region where the FMR is probed.

Similar to the measurements presented in Chapter 7, we scan the laser beam with a spot diameter of $d = 4\sigma \approx 2.6\,\mu\mathrm{m}$ across the surface of the sample while measuring the change of the EDFMR signal ΔV between a fixed pair of Au wires. The upper panel of Figure 8.2(b) shows the reflectivity map of the region around the contacted part of the Py wire. The bottom panel

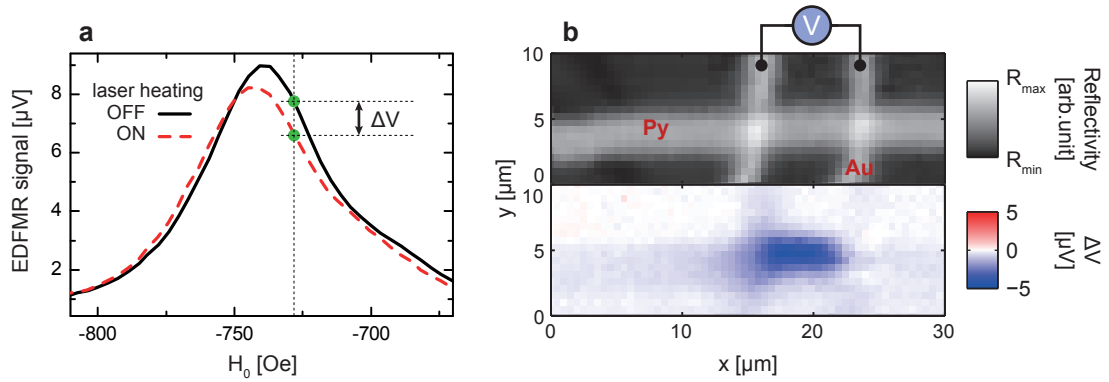

Figure 8.2 | Spatially resolved modulation of EDFMR by laser-induced heating. (a) Illustration of measurement principle: When measuring the EDFMR signal at a fixed DC field H_0, the heating-induced change of the shape of the resonance curve appears as a change of the signal magnitude. ΔV is the difference between the EDFMR signal without and with laser illumination. (b) Upper panel: Reflectivity map obtained from a sample from batch II (MgO substrate) with $w_{\mathrm{Py}} = 4\,\mu\mathrm{m}$. Laser parameters: $\lambda = 532\,\mathrm{nm}$, $\sigma \approx 650\,\mathrm{nm}$, $P = 39\,\mathrm{mW}$. The EDFMR voltage is measured with a lock-in amplifier between the two labeled Au wires at $f_{\mathrm{MW}} = 7.19\,\mathrm{GHz}$, $P_{\mathrm{MW}} = 30\,\mathrm{dBm}$ and an amplitude modulation frequency of $f_{\mathrm{m}} = 628\,\mathrm{Hz}$. Lower panel: Change in EDFMR signal ΔV as a function of laser spot position at $H = -730\,\mathrm{Oe}$.

shows the value of ΔV as a function of position. It is striking that a significant decrease of the EDFMR signal occurs only when the Py wire between the two contacted Au wires is directly heated by the laser beam. The signal is almost constant in this region. We can exclude the Seebeck effect as the origin of this local drop of ΔV as the thermovoltage changes its sign between the two Au/Py thermocouples (see Figure 7.2(c)). The observed weak decrease of the signal for positions outside this region is likely due to heat conduction along the Au and Py wires, indirectly heating up the contacted region. This measurement confirms the strictly local character of the EDFMR detection in the present sample.

Now that we have identified the region giving rise to the detected signal, we investigate the influence of a well-defined temperature gradient on the FMR. For this purpose the laser spot is centered on one of the adjacent Au/Py crossing points, as illustrated in Figure 8.3(c). By moving the sample out of focus, the spot size is increased to about $d = 4\sigma \approx 26\,\mu\mathrm{m}$ ($\sigma = 6.5\,\mu\mathrm{m}$), resulting in a lateral temperature gradient within the probed region in the indicated direction.

FMR spectra are then acquired for several values of the laser power, i.e. for a range of different magnitudes of the temperature gradient. As depicted in the insets of Figure 8.3(a) and (b), the magnetic DC field is applied at an angle of ~ 45° with respect to the direction of the Py wire. The angle is chosen such that the magnitude of the EDFMR signal is maximized (see Section 5.3.4). AMR measurements confirm that the magnetization is saturated for typical values of the resonance field H_{res}. From numerical simulations of the temperature distribution (see Section 6.2.2) at maximum laser power $P_{\mathrm{max}} = 400\,\mathrm{mW}$ we extract an average temperature increase of $\overline{\Delta T} \approx 63\,\mathrm{K}$ and an average temperature gradient of $\overline{\nabla_x T} \approx 3.5 \times 10^6\,\mathrm{K\,m^{-1}}$. We

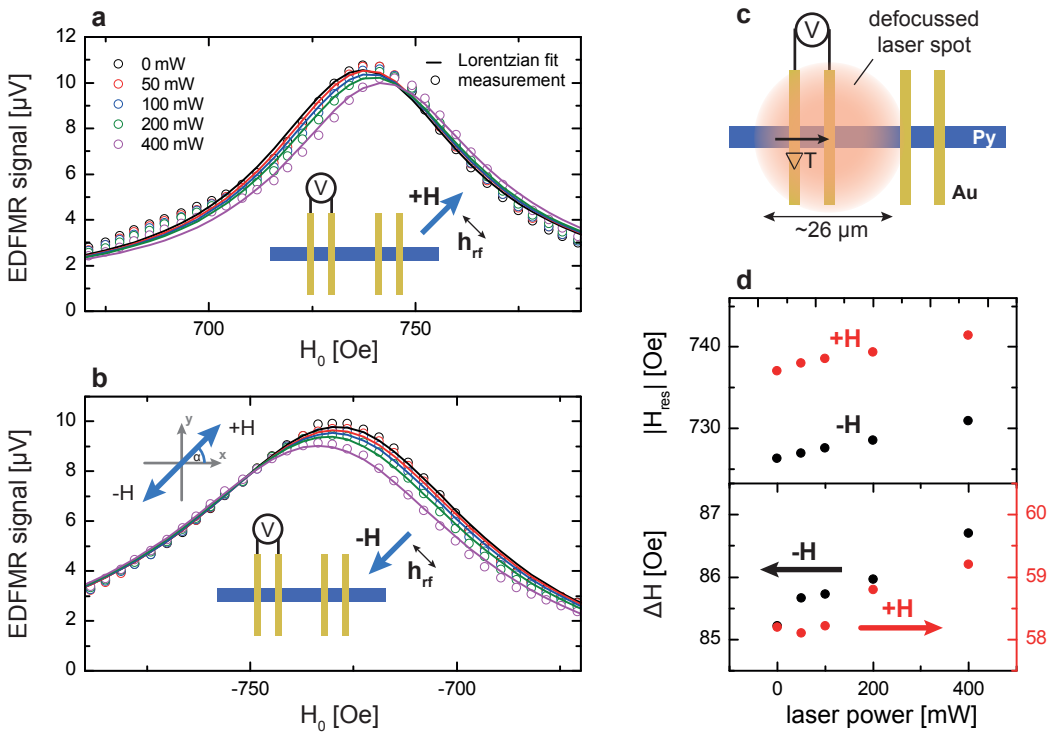

Figure 8.3 | EDFMR in a microscopic laser-induced heat gradient. (a & b) EDFMR spectra for laser power between 0 mW and 400 mW, signal is measured between two adjacent Au wires for saturation along $+H$ (a) and $-H$ (b) at a field angle of 45° with respect to the Py wire. Schematic illustrations indicate the relative orientation of the wire, H_0 and the excitation field h_{rf}. Open symbols represent experimental data, whereas solid lines are fits based on asymmetric Lorentzian functions. FMR and laser parameters (except spot size) are the same as in Figure 8.2. (c) Defocussed laser beam with $\sigma \approx 6.5\,\mu\mathrm{m}$ positioned on the Au wire generates a strong temperature gradient ($\approx 10\,\mathrm{K\,\mu m^{-1}}$) in the probed part of the Py wire. (d) Position of resonance field H_{res} (upper panel) and linewidth ΔH (lower panel) as a function of laser power for both field (and thus magnetization) orientations.

therefore assume that the maximum gradient generated in this about 9 µm × 4 µm small section of the Py wire is more than one order of magnitude larger than in the experiment discussed in Section 8.1. Figure 8.3(a) and (b) show how the FMR peak changes in shape and position as a function of laser power for positive and negative saturation of the magnetization. In agreement with our previous findings obtained from the homogeneous Py film, we observe a shift of the resonance field to higher (absolute) values as well as a slight change in the width of the resonance when increasing the temperature.

We now turn to the possible influence of a thermally generated spin current on the FMR by comparing the evolution of H_{res} and ΔH with increasing temperature gradient $\nabla_y T$. For both field orientations we obtain a gradual increase in H_{res}, as expected from the temperature-dependence of the saturation magnetization in Py. The maximum shift amounts to 4.4 Oe and 4.6 Oe for $+H$ and $-H$, respectively, which corresponds to a temperature increase of about 24 K (see Section 5.3.2). This is in reasonable agreement with the average temperature rise predicted by the numerical simulation, considering that the latter is partly based on estimated parameters such as the interfacial heat conductivity between Py and MgO. The line width ΔH, shown in the bottom panel of Figure 8.3(d), follows the same trend as observed for the Py film. Irrespective of the field direction, ΔH slightly increases by up to 1.5 Oe. As in Section 8.1, we attribute this increase to the inhomogeneous temperature distribution within the probed region. The presented data is completely symmetric in H_0, and the changes of the line shape can thus be attributed entirely to the normal temperature-dependence of FMR (due to $M_s(T)$). Our data suggests that the strong temperature gradient (i.e. not the absolute temperature rise) considered in this experiment does not significantly affect the FMR. It thus appears that, even if a thermal spin current is generated by this temperature gradient, it is either too small to lead to a measurable effect on the FMR or it does not exert a torque on the magnetization. In the following, we discuss different possible explanations for the absence of any temperature gradient-induced effect.

First, it should be noted that the thermal spin-transfer torque effect is not expected to give rise to any modulation of the FMR in this experiment: the effect has been predicted [146] and experimentally observed [147] for non-collinear magnetization structures, such as spin valves, only. However, in the experiment discussed above, we excite the fundamental mode (coherent precession), where the magnetization is uniform.

Assuming that the simple (but for macroscopic distances controversial (see Section 5.1)) picture of a thermally generated spin current in the bulk due to the spin Seebeck effect is true, we would expect a spin torque density on the order of $\tau_s \sim 6 \times 10^{-8}\,\mathrm{J\,m^{-2}}$ for $\overline{\nabla_x T} \approx 3.5 \times 10^{6}\,\mathrm{K\,m^{-1}}$ (derived from the data given in Reference [188]). Experimental studies based on the injection of a SHE-generated spin current from Pt into Py have shown that a spin torque density of about $\tau_s \sim 4.7 \times 10^{-8}\,\mathrm{J\,m^{-2}}$ has a measurable impact on the magnetization relaxation and thus the FMR signal [170]. However, in the geometry used here, the spin polarization σ of the spin current is parallel to the local magnetization. Unlike in Reference [170] where the angle between $\mathbf{M}$ and $\boldsymbol{\sigma}$ is non-zero, our geometry would lead to a vanishing

torque acting on the magnetization (see Section 5.3.3). In this picture it is thus not surprising that we do not detect any effect of the temperature gradient on the magnetization dynamics.

The influence of a spatially varying temperature profile on the magnetization dynamics has recently been investigated theoretically by Bose *et al.* [189]. Based on a one-dimensional Lagrangian approach the authors conclude that a temperature profile $T(\boldsymbol{x})$ leads to an additional damping term of the form $\mathrm{d}\boldsymbol{m}/\mathrm{d}t \propto \gamma C \left[\nabla^2 T(\boldsymbol{x})\right] \boldsymbol{m}(\boldsymbol{x}, t)$. In an FMR measurement, such thermally induced damping would appear as a broadening of the lineshape. However, it is unclear to what extend this model is suitable to describe our experiments as the model is based on the assumption that $\boldsymbol{M} \perp \boldsymbol{\nabla} T$, which is clearly not the case in our experiment.

Models that directly focus on the influence of a temperature gradient on the fundamental FMR mode are rare. The only other approach of this kind has been developed by S.E. Barnes (published as a chapter in Reference [190]). According to Barnes, a fraction of the heat that leaves the sample must come from the dissipation due to the precession of the magnetization. Hence, the cone angle must be greater at the cold end than at the hot one. In this picture, heat must be forced to go from the hot to the cold end. This is not the case in the geometry discussed above, since the intimate contact between Py and the MgO substrate implies that heat flows everywhere into the substrate and the effect predicted by this model cannot occur.

This highlights a fundamental issue of this experiment in the current geometry. The in-plane component of the temperature gradient $\overline{\nabla_x T}$ is exceptionally large, even compared to electrically induced temperature gradients in spin valves [147]. However, our numerical simulations show that the maximum out-of-plane component of the gradient within the laser spot is about twice as large. Despite the thermal resistance of the Py/MgO interface, the MgO substrate represents an efficient heat sink as it exhibits both a larger heat capacity as well as a larger heat conductivity than Py ($\lambda_{\mathrm{MgO}} \approx 45\,\mathrm{W\,m^{-1}\,K^{-1}} > \lambda_{\mathrm{Py}} \approx 30\,\mathrm{W\,m^{-1}\,K^{-1}}$). This implies that the temperature gradient is far from being collinear with the magnetization, which seems to be one of the main requirements for the observation of the spin Seebeck effect. In addition, due to the spatially changing out-of-plane component, the inhomogeneity of the temperature gradient increases further, making any gradient-induced effect on the FMR hard to detect. To overcome these difficulties and to study the effect of a pure in-plane temperature gradient as proposed by Barnes, a sample based on a suspended bridge would be needed. By removing the dissipation channel through the substrate, a homogeneous in-plane temperature gradient could thus be generated.

9 Summary and Conclusions

The second part of this thesis is largely motivated by the discovery of the spin Seebeck effect (SSE) in macroscopic structures [20]. As discussed in Chapter 5, its origin as well as its possible entanglement with other thermoelectric effects, such as the anomalous Nernst effect (ANE), is currently subject of debate [4, 157]. In order to shed light on the issue of artifacts in the transverse SSE configuration we first develop an experimental setup that allows us to create temperature gradients in microscopic samples using focused laser heating – a novel approach that has recently raised significant attention [191, 160]. Our characterization shows that due to the small sample dimensions and the Gaussian shape of the laser beam, we indeed create large in-plane gradients greater than $1 \times 10^6\,\mathrm{K\,m^{-1}}$, exceeding most previous experiments by several orders of magnitude (in the original SSE experiment by Uchida et al. the temperature gradient amounts to only $\sim 1 \times 10^3\,\mathrm{K\,m^{-1}}$ [20]). Such strong gradients are expected to facilitate the detection of the SSE and, according to some, they should generate significant spin currents large enough to influence the local magnetization [191]. However, simulations show that there is also a large and undesirable out-of-plane temperature gradient. Air-bridge structures would be needed in order to generate temperature gradients in-plane only.

Unlike in experiments based on macroscopic samples heated by Peltier elements, we can control both the position and the spatial confinement of the temperature gradient with better than µm-accuracy. By scanning the laser beam across the surface of the sample we simultaneously obtain a reflectivity image and a position-dependent voltage. This opens the unique possibility of analyzing and separating the different thermovoltages that appear in crossed Py/Au wire structures. For this purpose, we perform a series of experiments based on different geometries, magnetization configurations, substrates and laser positions. Supported by numerical simulations of the laser-induced temperature distribution, we identify two major contributions to the laser-induced voltage: (i) the Seebeck effect due to local heating of the thermocouples at intersections of the Au and Py wires and (ii) the anomalous Nernst effect (ANE) due to the in-plane magnetization in the Py wire and the out-of-plane temperature gradient generated at the position of the laser spot.

The SE and ANE signals are generated simultaneously when heating an area close to the Au/Py

intersections. Using a novel approach based on a combination of time-resolved measurements and numerical simulations of the time-evolution of the Seebeck signal we unambiguously identify and separate the two contributions. In addition to that, the time-dependent data confirm that the ANE signal is generated locally, i.e. as a function of the magnetization in the illuminated area only. Given the complexity of the generated signals, we consider an analysis of this kind essential for any experimental study based on the transverse SSE configuration involving two or more materials.

Furthermore, we demonstrate thermoelectrical magnetic imaging of a 10 µm wide Py wire using spatially resolved measurements of the ANE probed by focused laser heating. The achieved lateral resolution of about 2 µm enables – for the first time based on this technique – a detailed study of the micromagnetic behavior on the µm-scale. We investigate the formation and pinning of magnetic domains during magnetization reversal and the impact of laser heating on the reversal process. Evidently, just like MOKE microscopy (magneto-optical Kerr effect), this technique cannot compete with the ~ nm-resolution provided by other imaging techniques, such as magnetic force microscopy (MFM) or spin-resolved SEM (SEMPA). However, due to its simplicity (in contrast to MOKE, control and modulation of the light polarization is not required) it may be a viable alternative for specific applications with moderate resolution requirements where electrical contacts to the sample are available. Additional studies would be required to assess its applicability to other sample geometries and magnetization structures, with special focus on minimizing the impact of the inherent heating on the micromagnetic behavior.

Finally, we explore the effect of heat gradients on magnetization dynamics. For this purpose, we combine the local generation of heat gradients with local excitation and detection of FMR. For the geometry and temperature distribution considered here, there appears to be no detectable effect (despite large temperature gradients of $> 1 \times 10^6\,\mathrm{K\,m^{-1}}$). However, the question whether there is an effect on the fundamental mode of the resonance or not cannot be answered with absolute certainty. Future studies with improved sensitivity as well as a more desirable shape of the temperature distribution (entirely in-plane) are needed. In particular, suspended magnetic bridges represent a promising idea to better control temperature gradients. Since controlling the temperature gradient is essential in any experimental demonstration of spin-caloric effects, experiments based on such samples promise to reveal new insights into many of these effects.

A Fabrication process parameters

A.1 Process I: Focused ion beam (FIB) lithography of suspended SiN bridges

Initial state of sample: Si_3N_4 (200 nm)/SiO_2 (500 nm)/Si with EBL-patterned etch mask composed of Cr (5 nm)/Au (30 nm)/Cr (5 nm).

1. Clean sample after cleaving (acetone, ethanol, water)
2. RIE of the masked Si_3N_4 layer

$Q(CF_4)$	$Q(O_2)$	p	P	t
42 sccm	5 sccm	0.01 mbar	110 W	3.5 min

3. FIB etching of the Au/Cr mask and the Si_3N_4 layer to define 2 µm wide bridges that will become underetched in the subsequent HF etching step. Etching has to be stopped within the SiO_2 layer to avoid redeposition of Si onto the sidewalls.

V_{accel}	I_{Ga}	t_{dwell}	step size
30 kV	100 pA	25.6 µs	5 nm

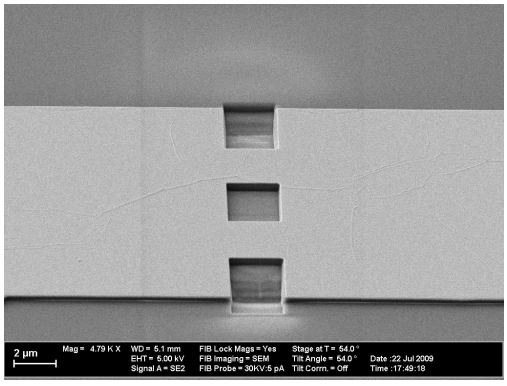

4. Rinsing sample in acetone, ethanol and water

5. Wet etching in HF solution - removes SiO_2 layer and creates untercut.

solution	t
HF / H_2O (1:1 v/v)	2 min

6. Cleaning of edges of underetched Cr/Au/Cr/SiN layer using FIB. The SEM image below shows a manually corrected edge that was previously in contact with the substrate.

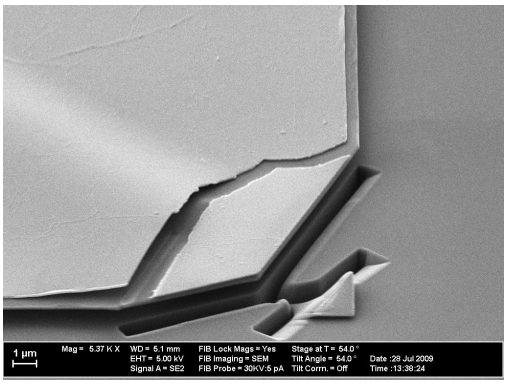

7. Preparation of ring section with notch (low current / small spot size / large number of loops for controlled etching and best edge sharpness)

V_{accel}	I_{Ga}	t_{dwell}	step size
30 kV	5 pA (bridge) / 1 pA (notch)	62.5 µs	5 nm

and opening of second (backup) bridge:

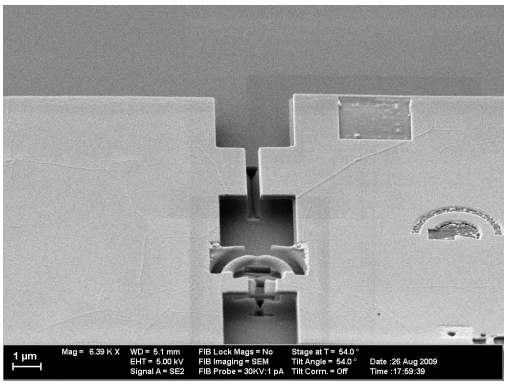

8. Removal of Au layer on top of SiN bridge at $I_{Ga} = 1$ pA.

A.2 Process II: Shadow mask evaporation

Initial state of sample: EBL-exposed double layer resist composed of 540 nm MMA (Methyl methacrylate) / 200 nm PMMA (Poly(methyl methacrylate) or Plexiglas) on a SiO_2 (200 nm)/Si substrate.

1. Development of double layer resist in isopropanol for 25 min

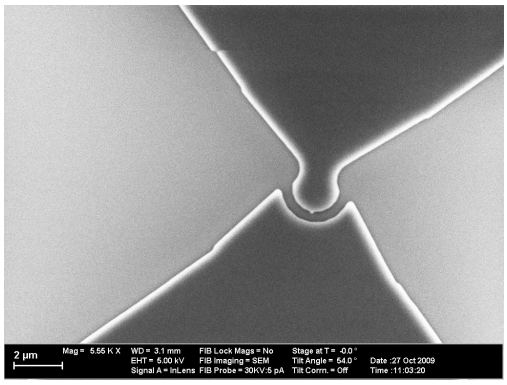

   The bright edges in the pattern indicate the presence of a pronounced undercut in the double layer resist. As electron beam irradiation (by the SEM) decomposes (P)MMA, the thin small notch in the image above is smaller than than it was originally right after development.

2. Deposition of a 5 nm Ti / 50 nm Au layer to form bonding pads. A thin metal wire placed precisely along the line of nanocontacts served as a simple deposition mask (left image). The test structure to the right illustrates the undercut along the resist edges electrically separating the bonding pads from the metal film on top of the resist.

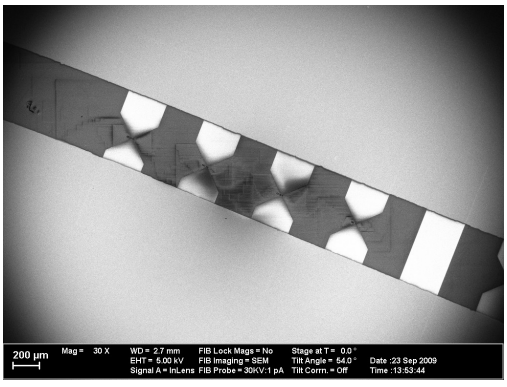

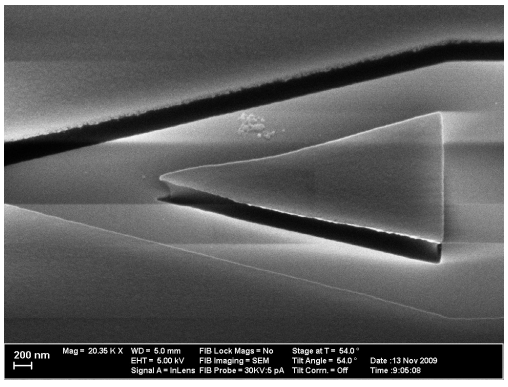

3. Wire bonding and deposition of Py

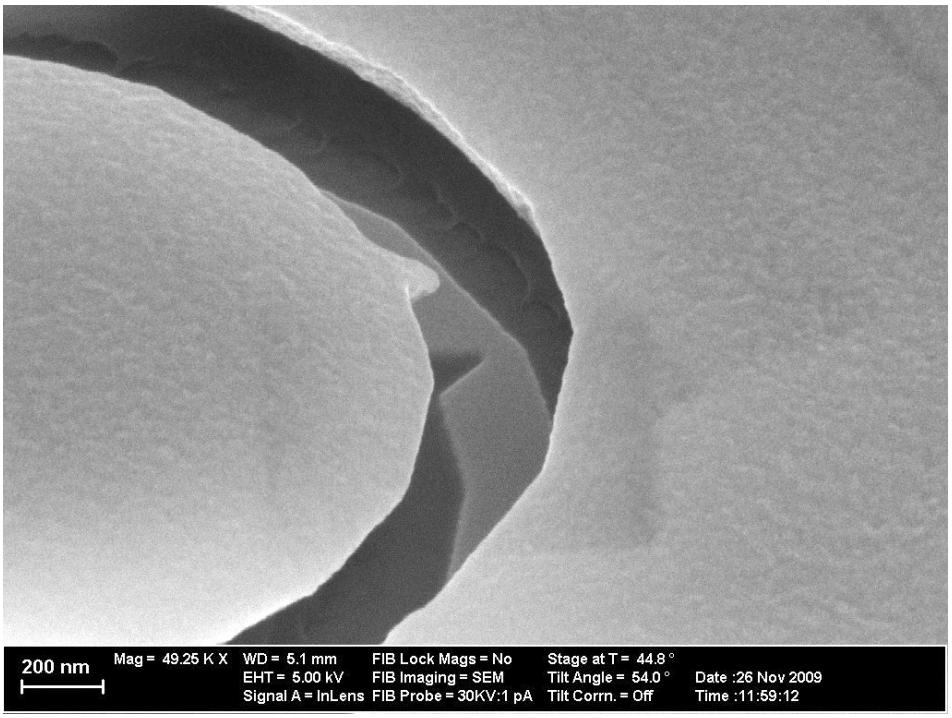

Bibliography

[1] Bader, S. & Parkin, S. Spintronics. *Annu. Rev. Cond. Mat. Phys.* **1**, 71–88 (2010).

[2] Fert, A. Nobel lecture: Origin, development, and future of spintronics. *Angew. Chem. Int. Ed.* **80**, 1517 (2008).

[3] Terabe, K., Hasegawa, T., Nakayama, T. & Aono, M. Quantized conductance atomic switch. *Nature* **433**, 47–50 (2005).

[4] Bauer, G. E. W., Saitoh, E. & van Wees, B. J. Spin caloritronics. *Nat. Mater.* **11**, 391–399 (2012).

[5] Jungwirth, T., Wunderlich, J. & Olejník, K. Spin Hall effect devices. *Nat. Mater.* **11**, 382–390 (2012).

[6] Chappert, C., Fert, A. & Van Dau, F. N. The emergence of spin electronics in data storage. *Nat. Mater.* **6**, 813–823 (2007).

[7] Baibich, M. N. *et al.* Giant magnetoresistance of (001)Fe/(001)Cr magnetic superlattices. *Phys. Rev. Lett.* **61**, 2472 (1988).

[8] Binasch, G., Grünberg, P., Saurenbach, F. & Zinn, W. Enhanced magnetoresistance in layered magnetic structures with antiferromagnetic interlayer exchange. *Phys. Rev. B* **39**, 4828 (1989).

[9] Sinova, J. & Žutić, I. New moves of the spintronics tango. *Nat. Mater.* **11**, 368–371 (2012).

[10] Yuasa, S., Nagahama, T., Fukushima, A., Suzuki, Y. & Ando, K. Giant room-temperature magnetoresistance in single-crystal Fe/MgO/Fe magnetic tunnel junctions. *Nat. Mater.* **3**, 868–871 (2004).

[11] Kläui, M. Head-to-head domain walls in magnetic nanostructures. *J. Phys.: Condens. Matter* **20**, 313001 (2008).

[12] Franken, J., Hoeijmakers, M., Swagten, H. & Koopmans, B. Tunable resistivity of individual magnetic domain walls. *Phys. Rev. Lett.* **108**, 37205 (2012).

[13] Levy, P. M. & Zhang, S. Resistivity due to domain wall scattering. *Phys. Rev. Lett.* **79**, 5110 (1997).

[14] Marrows, C. H. Spin-polarised currents and magnetic domain walls. *Adv. Phys.* **54**, 585–713 (2005).

[15] Agraït, N., Yeyati, A. L. & van Ruitenbeek, J. M. Quantum properties of atomic-sized conductors. *Phys. Rep.* **377**, 81–279 (2003).

[16] Doudin, B. & Viret, M. Ballistic magnetoresistance? *J. Phys.: Condens. Matter* **20**, 083201 (2008).

[17] Slonczewski, J. C. Current-driven excitation of magnetic multilayers. *J. Magn. Magn. Mater.* **159**, L1–L7 (1996).

[18] Brataas, A., Kent, A. D. & Ohno, H. Current-induced torques in magnetic materials. *Nat. Mater.* **11**, 372–381 (2012).

[19] Jedema, F. J., Filip, A. T. & van Wees, B. J. Electrical spin injection and accumulation at room temperature in an all-metal mesoscopic spin valve. *Nature* **410**, 345–348 (2001).

[20] Uchida, K. *et al.* Observation of the spin Seebeck effect. *Nature* **455**, 778–781 (2008).

[21] Kittel, C. & McEuen, P. *Introduction to solid state physics*, vol. 7 (Wiley New York, 1976).

[22] Mott, N. F. The resistance and thermoelectric properties of the transition metals. *Proceedings of the Royal Society of London. Series A-Mathematical and Physical Sciences* **156**, 368–382 (1936).

[23] Mazin, I. I. How to define and calculate the degree of spin polarization in ferromagnets. *Phys. Rev. Lett.* **83**, 1427–1430 (1999).

[24] Soulen Jr, R. *et al.* Measuring the spin polarization of a metal with a superconducting point contact. *Science* **282**, 85–88 (1998).

[25] Meservey, R. & Tedrow, P. Spin-polarized electron tunneling. *Phys. Rep.* **238**, 173–243 (1994).

[26] Takahashi, S. & Maekawa, S. Spin injection and detection in magnetic nanostructures. *Phys. Rev. B* **67**, 052409 (2003).

[27] Bass, J. & Pratt Jr, W. Spin-diffusion lengths in metals and alloys, and spin-flipping at metal/metal interfaces: an experimentalist's critical review. *J. Phys.: Condens. Matter* **19**, 183201 (2007).

[28] Alex-engraver. Spin-valve GMR.svg. *(http://commons.wikimedia.org/wiki/File:Spin-valve_GMR.svg) Creative Commons BY-SA 3.0* (2011).

[29] Parkin, S. S. P., Li, Z. G. & Smith, D. J. Giant magnetoresistance in antiferromagnetic Co/Cu multilayers. *Appl. Phys. Lett.* **58**, 2710–2712 (1991).

[30] Julliere, M. Tunneling between ferromagnetic films. *Phys. Lett. A* **54**, 225–226 (1975).

[31] Slonczewski, J. C. Conductance and exchange coupling of two ferromagnets separated by a tunneling barrier. *Phys. Rev. B* **39**, 6995 (1989).

[32] MacLaren, J., Zhang, X. & Butler, W. Validity of the Julliere model of spin-dependent tunneling. *Phys. Rev. B* **56**, 11827 (1997).

[33] Sun, J. & Ralph, D. Magnetoresistance and spin-transfer torque in magnetic tunnel junctions. *J. Magn. Magn. Mater.* **320**, 1227–1237 (2008).

[34] Hubert, A. & Schäfer, R. *Magnetic domains: the analysis of magnetic microstructures* (Springer Verlag, 1998).

[35] Parkin, S. S. P., Hayashi, M. & Thomas, L. Magnetic Domain-Wall racetrack memory. *Science* **320**, 190–194 (2008).

[36] Allwood, D. A. *et al.* Magnetic Domain-Wall logic. *Science* **309**, 1688–1692 (2005).

[37] Beach, G. S. D., Tsoi, M. & Erskine, J. L. Current-induced domain wall motion. *J. Magn. Magn. Mater.* **320**, 1272–1281 (2008).

[38] Kläui, M. & Vaz, C. A. F. Magnetization configurations and reversal in small magnetic elements. *Handbook of Magnetism and Advanced Magnetic Materials* (2007).

[39] McMichael, R. & Donahue, M. Head to head domain wall structures in thin magnetic strips. *IEEE Trans. Magn.* **33**, 4167–4169 (1997).

[40] Backes, D. *et al.* Transverse domain walls in nanoconstrictions. *Appl. Phys. Lett.* **91**, 112502–112502 (2007).

[41] Bruno, P. Geometrically constrained magnetic wall. *Phys. Rev. Lett.* **83**, 2425 (1999).

[42] Kläui, M. *et al.* Domain wall pinning in narrow ferromagnetic ring structures probed by magnetoresistance measurements. *Phys. Rev. Lett.* **90**, 097202 (2003).

[43] Maxwell, J. *A treatise on electricity and magnetism*, vol. 1 (Clarendon Press, 1873).

[44] Petrovykh, D. Y. *et al.* Spin-dependent band structure, fermi surface, and carrier lifetime of permalloy. *Appl. Phys. Lett.* **73**, 3459–3461 (1998).

[45] Sharvin, Y. A possible method for studying Fermi surfaces. *Soviet Journal of Experimental and Theoretical Physics* **21**, 655 (1965).

[46] Wexler, G. The size effect and the non-local Boltzmann transport equation in orifice and disk geometry. *Proceedings of the Physical Society* **89**, 927 (1966).

[47] Landauer, R. Electrical resistance of disordered one-dimensional lattices. *Philos. Mag.* **21**, 863–867 (1970).

[48] Rodrigues, V., Bettini, J., Silva, P. & Ugarte, D. Evidence for spontaneous spin-polarized transport in magnetic nanowires. *Phys. Rev. Lett.* **91**, 096801 (2003).

[49] Shimizu, M., Saitoh, E., Miyajima, H. & Otani, Y. Conductance quantization in ferromagnetic Ni nano-constriction. *J. Magn. Magn. Mater.* **239**, 243–245 (2002).

[50] Untiedt, C., Dekker, D. M. T., Djukic, D. & van Ruitenbeek, J. M. Absence of magnetically induced fractional quantization in atomic contacts. *Phys. Rev. B* **69**, 081401 (2004).

[51] Jansen, A., Gelder, A. & Wyder, P. Point-contact spectroscopy in metals. *J. Phys. C* **13**, 6073 (1980).

[52] Wiesendanger, R. *Scanning probe microscopy and spectroscopy: methods and applications* (Cambridge Univ Press (Cambridge England and New York), 1994).

[53] Gimzewski, J. & Möller, R. Transition from the tunneling regime to point contact studied using scanning tunneling microscopy. *Phys. Rev. B* **36**, 1284 (1987).

[54] Gai, Z., He, Y., Yu, H. & Yang, W. Observation of conductance quantization of ballistic metallic point contacts at room temperature. *Phys. Rev. B* **53**, 1042 (1996).

[55] Morpurgo, A. F., Marcus, C. M. & Robinson, D. B. Controlled fabrication of metallic electrodes with atomic separation. *Appl. Phys. Lett.* **74**, 2084 (1999).

[56] Sorbello, R. S. Electromigration and the local transport field in mesoscopic systems. *Phys. Rev. B* **39**, 4984–4996 (1989).

[57] Stöffler, D., Fostner, S., Grütter, P. & Hoffmann-Vogel, R. Scanning probe microscopy imaging of metallic nanocontacts. *Phys. Rev. B* **85**, 033404 (2012).

[58] Ho, P. S. & Kwok, T. Electromigration in metals. *Rep. Prog. Phys.* **52**, 301–348 (1989).

[59] Park, H., Lim, A. K. L., Alivisatos, A. P., Park, J. & McEuen, P. L. Fabrication of metallic electrodes with nanometer separation by electromigration. *Appl. Phys. Lett.* **75**, 301–303 (1999).

[60] Trouwborst, M. L., van der Molen, S. J. & van Wees, B. J. The role of Joule heating in the formation of nanogaps by electromigration. *J. Appl. Phys.* **99**, 114316–114316–7 (2006).

[61] Tao, N. J. Electron transport in molecular junctions. *Nat. Nanotechnol.* **1**, 173–181 (2006).

[62] Wu, Z. M. *et al.* Feedback controlled electromigration in four-terminal nanojunctions. *Appl. Phys. Lett.* **91**, 053118–053118–3 (2007).

[63] Strachan, D. R. *et al.* Controlled fabrication of nanogaps in ambient environment for molecular electronics. *Appl. Phys. Lett.* **86**, 043109–043109–3 (2005).

[64] Esen, G. & Fuhrer, M. S. Temperature control of electromigration to form gold nanogap junctions. *Appl. Phys. Lett.* **87**, 263101 (2005).

[65] Hoffmann, R., Weissenberger, D., Hawecker, J. & Stöffler, D. Conductance of gold nanojunctions thinned by electromigration. *Appl. Phys. Lett.* **93**, 043118–043118–3 (2008).

[66] Strachan, D. R. *et al.* Clean electromigrated nanogaps imaged by transmission electron microscopy. *Nano Lett.* **6**, 441–444 (2006).

[67] Strachan, D. R. *et al.* Real-time TEM imaging of the formation of crystalline nanoscale gaps. *Phys. Rev. Lett.* **100**, 056805 (2008).

[68] Thomson, W. On the electro-dynamic qualities of metals: effects of magnetization on the electric conductivity of nickel and of iron. *Proceedings of the Royal Society of London* **8**, 546–550 (1856).

[69] McGuire, T. & Potter, R. Anisotropic magnetoresistance in ferromagnetic 3d alloys. *IEEE Trans. Magn.* **11**, 1018–1038 (1975).

[70] Cabrera, G. G. & Falicov, L. M. Theory of the residual resistivity of Bloch walls I. Paramagnetic effects. *Phys. Status Solidi B* **61**, 539–549 (1974).

[71] Berger, L. Low-field magnetoresistance and domain drag in ferromagnets. *J. Appl. Phys.* **49**, 2156–2161 (1978).

[72] Viret, M. *et al.* Spin scattering in ferromagnetic thin films. *Phys. Rev. B* **53**, 8464 (1996).

[73] Gregg, J. F. *et al.* Giant magnetoresistive effects in a single element magnetic thin film. *Phys. Rev. Lett.* **77**, 1580 (1996).

[74] Brataas, A., Tatara, G. & Bauer, G. Ballistic and diffuse transport through a ferromagnetic domain wall. *Phys. Rev. B* **60**, 3406 (1999).

[75] Tatara, G. & Fukuyama, H. Resistivity due to a domain wall in ferromagnetic metal. *Phys. Rev. Lett.* **78**, 3773 (1997).

[76] van Gorkom, R. P., Brataas, A. & Bauer, G. E. W. Negative domain wall resistance in ferromagnets. *Phys. Rev. Lett.* **83**, 4401 (1999).

[77] Yavorsky, B. Y., Mertig, I., Perlov, A. Y., Yaresko, A. N. & Antonov, V. N. Giant magnetoresistance due to a domain wall in Fe: Ab initio study. *Phys. Rev. B* **66**, 174422 (2002).

[78] Van Hoof, J., Schep, K. M., Kelly, P. J. & Bauer, G. E. W. Ab initio magnetoresistance in magnetic domain walls. *J. Magn. Magn. Mater.* **177**, 188–192 (1998).

[79] Wickles, C. & Belzig, W. Electronic transport in ferromagnetic conductors with inhomogeneous magnetic order parameter and domain-wall resistance. *Phys. Rev. B* **80**, 104435 (2009).

[80] García, N., Muñoz, M. & Zhao, Y. Magnetoresistance in excess of 200% in ballistic Ni nanocontacts at room temperature and 100 Oe. *Phys. Rev. Lett.* **82**, 2923 (1999).

[81] Chopra, H. D. & Hua, S. Z. Ballistic magnetoresistance over 3000% in Ni nanocontacts at room temperature. *Phys. Rev. B* **66**, 020403 (2002).

[82] Hua, S. Z. & Chopra, H. D. 100,000 % ballistic magnetoresistance in stable Ni nanocontacts at room temperature. *Phys. Rev. B* **67**, 060401 (2003).

[83] Tatara, G., Zhao, Y., Muñoz, M. & García, N. Domain wall scattering explains 300% ballistic magnetoconductance of nanocontacts. *Phys. Rev. Lett.* **83**, 2030 (1999).

[84] Tagirov, L. R., Vodopyanov, B. P. & Efetov, K. B. Ballistic versus diffusive magnetoresistance of a magnetic point contact. *Phys. Rev. B* **63**, 104428 (2001).

[85] Bagrets, A., Papanikolaou, N. & Mertig, I. Magnetoresistance of atomic-sized contacts: An ab initio study. *Phys. Rev. B* **70**, 064410 (2004).

[86] Jacob, D., Fernández-Rossier, J. & Palacios, J. J. Magnetic and orbital blocking in Ni nanocontacts. *Phys. Rev. B* **71**, 220403 (2005).

[87] Burton, J. D., Sabirianov, R. F., Jaswal, S. S., Tsymbal, E. Y. & Mryasov, O. N. Magnetic moment softening and domain wall resistance in Ni nanowires. *Phys. Rev. Lett.* **97**, 077204 (2006).

[88] Velev, J., Sabirianov, R. F., Jaswal, S. S. & Tsymbal, E. Y. Ballistic anisotropic magnetoresistance. *Phys. Rev. Lett.* **94**, 127203 (2005).

[89] Viret, M. *et al.* Giant anisotropic magneto-resistance in ferromagnetic atomic contacts. *Eur. Phys. J. B* **51**, 4 (2006).

[90] Autes, G., Barreteau, C., Desjonqueres, M., Spanjaard, D. & Viret, M. Giant orbital moments are responsible for the anisotropic magnetoresistance of atomic contacts. *Europhys. Lett.* **83**, 17010 (2008).

[91] Czerner, M., Yavorsky, B. & Mertig, I. The role of noncollinear magnetic order and magnetic anisotropy for the transport properties through nanowires. *Phys. Status Solidi B* **247**, 2594–2602 (2010).

[92] Häfner, M., Viljas, J. K. & Cuevas, J. C. Theory of anisotropic magnetoresistance in atomic-sized ferromagnetic metal contacts. *Phys. Rev. B* **79**, 140410 (2009).

[93] Autes, G., Barreteau, C., Spanjaard, D. & Desjonquères, M. C. Electronic transport in iron atomic contacts: From the infinite wire to realistic geometries. *Phys. Rev. B* **77**, 155437 (2008).

[94] Otani, Y., Kim, S. G., Fukamichi, K., Kitakami, O. & Shimada, Y. Magnetic and transport properties of sub-micron ferromagnetic wires. *IEEE Trans. Magn.* **34**, 1096 –1098 (1998).

[95] Hong, K. & Giordano, N. Resistance of a domain wall in a thin ferromagnetic wire. *J. Phys.: Condens. Matter* **10**, L401–L407 (1998).

[96] Taniyama, T., Nakatani, I., Namikawa, T. & Yamazaki, Y. Resistivity due to domain walls in Co zigzag wires. *Phys. Rev. Lett.* **82**, 2780–2783 (1999).

[97] Rüdiger, U., Yu, J., Zhang, S., Kent, A. D. & Parkin, S. S. P. Negative domain wall contribution to the resistivity of microfabricated Fe wires. *Phys. Rev. Lett.* **80**, 5639 (1998).

[98] Giordano, N. & Çetin, B. Electron transport and magnetoresistance in ferromagnetic nanostructures. *Phys. Status Solidi B* **241**, 2404–2409 (2004).

[99] Wegrowe, J.-E., Kelly, D., Franck, A., Gilbert, S. E. & Ansermet, J.-P. Magnetoresistance of ferromagnetic nanowires. *Phys. Rev. Lett.* **82**, 3681 (1999).

[100] Miyake, K., Shigeto, K., Mibu, K., Shinjo, T. & Ono, T. Geometrical confinement of a domain wall in a nanocontact between two NiFe wires. *J. Appl. Phys.* **91**, 3468–3470 (2002).

[101] Montero, M. I. *et al.* Magnetoresistance of mechanically stable Co nanoconstrictions. *Phys. Rev. B* **70**, 184418 (2004).

[102] Wegrowe, J.-E. *et al.* Spin-dependent scattering of a domain wall of controlled size. *Phys. Rev. B* **61**, 12216 (2000).

[103] Ravelosona, D. *et al.* Domain-wall scattering in epitaxial FePd ordered alloy films with perpendicular magnetic anisotropy. *Phys. Rev. B* **59**, 4322 (1999).

[104] Viret, M. *et al.* Anisotropy of domain wall resistance. *Phys. Rev. Lett.* **85**, 3962 (2000).

[105] Danneau, R. *et al.* Individual domain wall resistance in submicron ferromagnetic structures. *Phys. Rev. Lett.* **88**, 157201 (2002).

[106] Ebels, U., Radulescu, A., Henry, Y., Piraux, L. & Ounadjela, K. Spin accumulation and domain wall magnetoresistance in 35 nm Co wires. *Phys. Rev. Lett.* **84**, 983 (2000).

[107] Hassel, C., Brands, M., Lo, F. Y., Wieck, A. D. & Dumpich, G. Resistance of a single domain wall in $(Co/Pt)_7$ multilayer nanowires. *Phys. Rev. Lett.* **97**, 226805 (2006).

[108] Aziz, A. *et al.* Angular dependence of domain wall resistivity in artificial magnetic domain structures. *Phys. Rev. Lett.* **97**, 206602 (2006).

[109] García, N., Qiang, G. G. & Saveliev, I. G. Balistic magnetoresistance in nanocontacts electrochemically grown between macro- and microscopic ferromagnetic electrodes. *Appl. Phys. Lett.* **80**, 1785 (2002).

[110] Egelhoff, W. *et al.* Artifacts in ballistic magnetoresistance measurements (invited). *J. Appl. Phys.* **95**, 7554–7559 (2004).

[111] Viret, M. *et al.* Magnetoresistance through a single nickel atom. *Phys. Rev. B* **66**, 220401 (2002).

[112] Yang, C., Zhang, C., Redepenning, J. & Doudin, B. In situ magnetoresistance of Ni nanocontacts. *Appl. Phys. Lett.* **84**, 2865 (2004).

[113] Keane, Z. K., Yu, L. H. & Natelson, D. Magnetoresistance of atomic-scale electromigrated nickel nanocontacts. *Appl. Phys. Lett.* **88**, 062514 (2006).

[114] Egle, S. *et al.* Magnetoresistance of atomic-size contacts realized with mechanically controllable break junctions. *Phys. Rev. B* **81**, 134402 (2010).

[115] Sokolov, A., Zhang, C., Tsymbal, E. Y., Redepenning, J. & Doudin, B. Quantized magnetoresistance in atomic-size contacts. *Nat Nano* **2**, 171–175 (2007).

[116] Shi, S. & Ralph, D. C. Atomic motion in ferromagnetic break junctions. *Nat. Nanotechnol.* **2**, 522–522 (2007).

[117] Sokolov, A., Zhang, C., Tsymbal, E. Y., Redepenning, J. & Doudin, B. Atomic motion in ferromagnetic break junctions. *Nat. Nanotechnol.* **2**, 522–523 (2007).

[118] Bolotin, K. I., Kuemmeth, F. & Ralph, D. C. Anisotropic magnetoresistance and anisotropic tunneling magnetoresistance due to quantum interference in ferromagnetic metal break junctions. *Phys. Rev. Lett.* **97**, 127202 (2006).

[119] Bolotin, K. I., Kuemmeth, F., Pasupathy, A. N. & Ralph, D. C. From ballistic transport to tunneling in electromigrated ferromagnetic breakjunctions. *Nano Lett.* **6**, 123–127 (2006).

[120] Ben Hamida, A., Rousseau, O., Petit-Watelot, S. & Viret, M. Positive domain wall resistance in atomic-sized constrictions. *Europhys. Lett.* **94**, 27002 (2011).

[121] Kläui, M. *et al.* Direct observation of domain-wall configurations transformed by spin currents. *Phys. Rev. Lett.* **95**, 26601 (2005).

[122] Rhensius, J. *et al.* Imaging of domain wall inertia in permalloy half-ring nanowires by time-resolved photoemission electron microscopy. *Phys. Rev. Lett.* **104**, 067201 (2010).

[123] Bedau, D. *et al.* Angular dependence of the depinning field for head-to-head domain walls at constrictions. *J. Appl. Phys.* **101**, 09F509–09F509 (2007).

[124] Patra, A. K. *et al.* Magnetoresistance measurement of tailored permalloy nanocontacts. *Phys. Rev. B* **82**, 134447 (2010).

[125] Bogart, L. K. & Atkinson, D. Domain wall anisotropic magnetoresistance in planar nanowires. *Appl. Phys. Lett.* **94**, 042511–042511 (2009).

[126] Achilles, S., Czerner, M. & Mertig, I. Tailoring magnetoresistance through rotating Ni particles. *Phys. Rev. B* **84**, 054418 (2011).

[127] Lee, E. Magnetostriction and magnetomechanical effects. *Rep. Prog. Phys.* **18**, 184 (1955).

[128] Ashcroft, N. & Mermin, M. *Introduction to Solid State Physics* (Saunders, Philadelphia, 1976).

[129] Harman, T. & Honig, J. *Thermoelectric and thermomagnetic effects and applications* (McGraw-Hill, New York, 1967).

[130] Mott, N. & Jones, H. *The theory of the properties of metals and alloys* (Dover Publications, 1958).

[131] Onsager, L. Reciprocal relations in irreversible processes. I. *Phys. Rev.* **37**, 405 (1931).

[132] Nernst, W. Über die electromotorischen kräfte, welche durch den Magnetismus in von einem Wärmestrome durchflossenen Metallplatten geweckt werden. *Annalen der Physik* **267**, 760–789 (1887).

[133] Smith, H. & Jensen, H. *Transport phenomena* (Oxford University Press, USA, 1989).

[134] Nagaosa, N., Sinova, J., Onoda, S., MacDonald, A. & Ong, N. Anomalous Hall effect. *Rev. Mod. Phys.* **82**, 1539 (2010).

[135] Xiao, D., Chang, M.-C. & Niu, Q. Berry phase effects on electronic properties. *Reviews of Modern Physics* **82**, 1959–2007 (2010).

[136] Wang, Y. *et al.* Onset of the vortexlike Nernst signal above T_c in $La_{2-x}Sr_xCuO_4$ and $Bi_2Sr_{2-y}La_yCuO_6$. *Phys. Rev. B* **64**, 224519 (2001).

[137] Miyasato, T. *et al.* Crossover behavior of the anomalous Hall effect and anomalous Nernst effect in itinerant ferromagnets. *Phys. Rev. Lett.* **99**, 86602 (2007).

[138] Onoda, S., Sugimoto, N. & Nagaosa, N. Quantum transport theory of anomalous electric, thermoelectric, and thermal Hall effects in ferromagnets. *Phys. Rev. B* **77**, 165103 (2008).

[139] Brechet, S. D. & Ansermet, J.-P. Heat-driven spin currents on large scales. *Phys. Status Solidi Rapid Res. Lett.* **5**, 423–425 (2011).

[140] Slachter, A., Bakker, F., Adam, J. & Van Wees, B. Thermally driven spin injection from a ferromagnet into a non-magnetic metal. *Nat. Phys.* **6**, 879–882 (2010).

[141] Flipse, J., Bakker, F. L., Slachter, A., Dejene, F. K. & Wees, B. J. v. Direct observation of the spin-dependent Peltier effect. *Nat. Nanotechnol.* **7**, 166–168 (2012).

[142] Hatami, M., Bauer, G. E. W., Zhang, Q. & Kelly, P. J. Thermoelectric effects in magnetic nanostructures. *Phys. Rev. B* **79**, 174426 (2009).

[143] Gravier, L., Serrano-Guisan, S., Reuse, F. & Ansermet, J.-P. Thermodynamic description of heat and spin transport in magnetic nanostructures. *Phys. Rev. B* **73**, 024419 (2006).

[144] Walter, M. *et al.* Seebeck effect in magnetic tunnel junctions. *Nat. Mater.* **10**, 742–746 (2011).

[145] Le Breton, J., Sharma, S., Saito, H., Yuasa, S. & Jansen, R. Thermal spin current from a ferromagnet to silicon by Seebeck spin tunnelling. *Nature* **475**, 82–85 (2011).

[146] Hatami, M., Bauer, G. E. W., Zhang, Q. & Kelly, P. J. Thermal Spin-Transfer torque in magnetoelectronic devices. *Phys. Rev. Lett.* **99**, 066603 (2007).

[147] Yu, H., Granville, S., Yu, D. P. & Ansermet, J.-P. Evidence for thermal Spin-Transfer torque. *Phys. Rev. Lett.* **104**, 146601 (2010).

[148] Saitoh, E., Ueda, M., Miyajima, H. & Tatara, G. Conversion of spin current into charge current at room temperature: Inverse spin-Hall effect. *Appl. Phys. Lett.* **88**, 182509 (2006).

[149] Jungwirth, T., Wunderlich, J. & Olejnik, K. Spin Hall effect devices. *Nat. Mater.* **11**, 382–390 (2012).

[150] Jaworski, C. M. *et al.* Observation of the spin-Seebeck effect in a ferromagnetic semiconductor. *Nat. Mater.* **9**, 898–903 (2010).

[151] Uchida, K. *et al.* Observation of longitudinal spin-Seebeck effect in magnetic insulators. *Appl. Phys. Lett.* **97**, 172505 (2010).

[152] Jaworski, C., Myers, R., Johnston-Halperin, E. & Heremans, J. Giant spin Seebeck effect in a non-magnetic material. *Nature* **487**, 210–213 (2012).

[153] Adachi, H., Uchida, K., Saitoh, E. & Maekawa, S. Theory of the spin Seebeck effect. *arXiv preprint arXiv:1209.6407* (2012).

[154] Agrawal, M. *et al.* Magnon-phonon coupling unmasked: a direct measurement of magnon temperature. *arXiv preprint arXiv:1209.3405* (2012).

[155] Jaworski, C. *et al.* Spin-Seebeck effect: a phonon driven spin distribution. *Phys. Rev. Lett.* **106**, 186601 (2011).

[156] Uchida, K. *et al.* Long-range spin Seebeck effect and acoustic spin pumping. *Nat. Mater.* **10**, 737–741 (2011).

[157] Huang, S. Y., Wang, W. G., Lee, S. F., Kwo, J. & Chien, C. L. Intrinsic Spin-dependent thermal transport. *Phys. Rev. Lett.* **107**, 216604 (2011).

[158] Bosu, S. *et al.* Spin Seebeck effect in thin films of the Heusler compound Co_2MnSi. *Phys. Rev. B* **83**, 224401 (2011).

[159] Sears, M. & Saslow, W. Thermal equilibration and thermally induced spin currents in a thin-film ferromagnet on a substrate. *Phys. Rev. B* **85**, 035446 (2012).

[160] Weiler, M. *et al.* Local charge and spin currents in magnetothermal landscapes. *Phys. Rev. Lett.* **108**, 106602 (2012).

[161] Huang, S. *et al.* Transport magnetic proximity effects in platinum. *Phys. Rev. Lett.* **109**, 107204 (2012).

[162] Vonsovskii, S. *Ferromagnetic resonance* (Pergamon Press, Oxford, 1966).

[163] Korenivski, V. & Slonczewski, J. *Introduction to Spintronics* (KTH, Stockholm, 2007).

[164] Goryunov, Y. *et al.* Magnetic anisotropies of sputtered Fe films on MgO substrates. *Phys. Rev. B* **52**, 13450 (1995).

[165] Liu, Z., Giesen, F., Zhu, X., Sydora, R. & Freeman, M. Spin wave dynamics and the determination of intrinsic damping in locally excited permalloy thin films. *Phys. Rev. Lett.* **98**, 87201 (2007).

[166] O'Handley, R. *Modern magnetic materials: principles and applications* (Wiley New York, 2000).

[167] Nazaretski, E. *et al.* Temperature-dependent magnetic resonance force microscopy studies of a thin permalloy film. *J. Appl. Phys.* **101**, 074905–074905 (2007).

[168] Ghosh, A., Auffret, S., Ebels, U. & Bailey, W. Penetration depth of transverse spin current in ultrathin ferromagnets. *Phys. Rev. Lett.* **109**, 127202 (2012).

[169] Berger, L. Emission of spin waves by a magnetic multilayer traversed by a current. *Phys. Rev. B* **54**, 9353 (1996).

[170] Ando, K. *et al.* Electric manipulation of spin relaxation using the spin-Hall effect. *Phys. Rev. Lett.* **101**, 036601 (2008).

[171] Tserkovnyak, Y., Brataas, A., Bauer, G. & Halperin, B. Nonlocal magnetization dynamics in ferromagnetic heterostructures. *Rev. Mod. Phys.* **77**, 1375 (2005).

[172] Azevedo, A., Vilela-Leão, L. H., Rodríguez-Suárez, R. L., Lacerda Santos, A. F. & Rezende, S. M. Spin pumping and anisotropic magnetoresistance voltages in magnetic bilayers: Theory and experiment. *Phys. Rev. B* **83**, 144402 (2011).

[173] Guan, Y., Bailey, W., Vescovo, E., Kao, C. & Arena, D. Phase and amplitude of element-specific moment precession in $Ni_{81}Fe_{19}$. *J. Magn. Magn. Mater.* **312**, 374–378 (2007).

[174] Harder, M., Cao, Z. X., Gui, Y. S., Fan, X. L. & Hu, C. Analysis of the line shape of electrically detected ferromagnetic resonance. *Phys. Rev. B* **84**, 054423 (2011).

[175] Palik, E. & Ghosh, G. *Handbook of optical constants of solids*, vol. 3 (Academic press, 1998).

[176] Neuber, G., Rauer, R., Kunze, J., Backstrom, J. & Rübhausen, M. Generalized magneto-optical ellipsometry in ferromagnetic metals. *Thin Solid Films* **455**, 39–42 (2004).

[177] Costescu, R. M., Wall, M. A. & Cahill, D. G. Thermal conductance of epitaxial interfaces. *Phys. Rev. B* **67**, 054302 (2003).

[178] Cahill, D., Bullen, A. & Lee, S.-M. Interface thermal conductance and the thermal conductivity of multilayer thin films. *High Temp.-High Press.* **32** (2000).

[179] Lyeo, H.-K. & Cahill, D. G. Thermal conductance of interfaces between highly dissimilar materials. *Phys. Rev. B* **73**, 144301 (2006).

[180] Bakker, F. L., Flipse, J. & van Wees, B. J. Nanoscale temperature sensing using the Seebeck effect. *J. Appl. Phys.* **111**, 084306–084306–4 (2012).

[181] David, P. & Heath, M. The shape-dependent demagnetizing field in ferromagnetic resonance. *J. Phys. C* **3**, 1356–1362 (1970).

[182] LeCraw, R. C., Spencer, E. G. & Porter, C. S. Ferromagnetic resonance line width in yttrium iron garnet single crystals. *Phys. Rev.* **110**, 1311–1313 (1958).

[183] Kronik, L. & Shapira, Y. Surface photovoltage phenomena: theory, experiment, and applications. *Surf. Sci. Rep.* **37**, 1–206 (1999).

[184] Slachter, A., Bakker, F. L. & van Wees, B. J. Anomalous Nernst and anisotropic magnetoresistive heating in a lateral spin valve. *Phys. Rev. B* **84**, 020412 (2011).

[185] Braun, H.-B. Statistical mechanics of nonuniform magnetization reversal. *Phys. Rev. B* **50**, 16501–16521 (1994).

[186] Bhagat, S. & Lubitz, P. Temperature variation of ferromagnetic relaxation in the 3 d transition metals. *Phys. Rev. B* **10**, 179 (1974).

[187] Patton, C. & Wilts, C. Temperature dependence of the ferromagnetic resonance linewidth in thin NiFe films. *J. Appl. Phys.* **38**, 3537–3540 (1967).

[188] Uchida, K. *et al.* Phenomenological analysis for spin-Seebeck effect in metallic magnets. *J. Appl. Phys.* **105**, 07C908 (2009).

[189] Bose, T. & Trimper, S. Temperature gradient assisted magnetodynamics. *Phys. Lett. A* (2012).

[190] Maekawa, S., Valenzuela, S., Saitoh, E. & Kimura, T. *Spin Current (Series on Semiconductor Science and Technology 17)* (Oxford University Press, 2012).

[191] Möhrke, P., Rhensius, J., Thiele, J., Heyderman, L. & Kläui, M. Tailoring laser-induced domain wall pinning. *Solid State Commun.* **150**, 489–491 (2010).

Arndt von Bieren
E-mail: arndt.vb@gmail.com

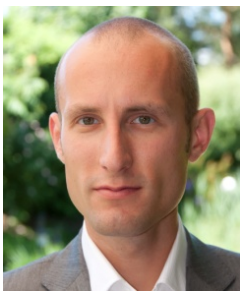

Professional Experience

4/2010 – 2/2013	**École Polytechnique Fédérale de Lausanne (EPFL)**, Switzerland *Research / Teaching assistant (PhD student), Physics of nanostructures lab (LPMN)*
4/2009 – 4/2010	**University of Konstanz,** Germany *Research / Teaching assistant (PhD student), Nanomagnetism research group*
7/2007 – 4/2009	**AlbaNova University Center, KTH**, Stockholm, Sweden *Research assistant and Diploma / Master student, Section of Nanostructure Physics*
9/2005 – 4/2006	**Walter Schottky Institute,** Munich, Germany *Research assistant (part-time), Semiconductor Technology group (E26)*
9/2004 – 10/2004	**Infineon Technologies AG**, Munich, Germany *Internship in quality management, Secure Mobile Solutions division*

Education

4/2009 – 2/2013	**Ph.D. studies in Physics, Nanomagnetism** École Polytechnique Fédérale de Lausanne (EPFL) and University of Konstanz
2006 – 2008	**M.Sc., Nanoelectronics** Royal Institute of Technology (KTH), Stockholm, Sweden
2003 – 2009	**Diplom, Engineering Physics** Technical University of Munich (TUM), Germany